Research Paper

Geosphere, published online on 12 November 2015 as doi:10.1130/GES01066.1

GEOSPHERE

GEOSPHERE; v. 11, no. 6

doi:10.1130/GES01066.1

13 figures; 9 tables; 10 supplemental files

CORRESPONDENCE: quakejay@gmail.com

CITATION: Patton, J.R., Goldfinger, C., Morey, A.E., Ikehara, K., Romsos, C., Stoner, J., Djadjadihardja, Y., Udrekh, Ardhyastuti, S., Gaffar, E.Z., and Vizcaino, A., 2015, A 6600 year earthquake history in the region of the 2004 Sumatra-Andaman subduction zone earthquake: Geosphere, v. 11, no. 6, doi:10.1130/GES01066.1.

Received 23 April 2014
Revision received 23 June 2015
Accepted 21 September 2015

A 6600 year earthquake history in the region of the 2004 Sumatra-Andaman subduction zone earthquake

Jason R. Patton[1], Chris Goldfinger[1], Ann E. Morey[1], Ken Ikehara[2], Chris Romsos[1], Joseph Stoner[1], Yusuf Djadjadihardja[3], Udrekh[3], Sri Ardhyastuti[3], Eddy Zulkarnaen Gaffar[4], and Alexis Vizcaino[5]

[1]College of Earth, Ocean and Atmospheric Sciences, Oregon State University, 104 CEOAS Administration Building, 101 SW 26th Street, Corvallis, Oregon 97331, USA
[2]National Institute of Advanced Industrial Science and Technology (AIST), 1-1-1 Umezono, Tsukuba, Ibaraki 305-8568, Japan
[3]Bandan Penghajian dan Penerapan Teknologi (BPPT), 2nd Building, 19th Floor, Jl.MH. Thamrin 8, Jakarta, 10340 Indonesia
[4]Geotechnology LIPI (Lembaga Ilmu Pengetahuan Indonesia), Jalan Cisitu-Sangkuriang, Bandung 40141, Indonesia
[5]Unitat de Tecnologia Marina-CSIC, Centre Mediterrani d'Investigacions Marines i Ambientals (CMIMA), Passeig Marı´tim de la Barceloneta, 37-49, 08003 Barcelona, Spain

ABSTRACT

In order to investigate the possibility of a long-term paleoseismic history from offshore sedimentary records in Sumatra, we collected 144 deep-sea sediment cores in the trench and in lower slope piggyback basins of the Sumatra accretionary prism. We used multibeam bathymetry and seismic reflection data to develop an understanding of catchment basins, turbidity current pathways, and depositional styles, as well as to precisely locate our gravity cores, piston cores, Kasten cores, and multicores. We use detailed physical property data, including computed tomographic X-ray, gamma density, magnetic susceptibility, grain-size analysis, faunal analysis, and smear slides, to evaluate the turbidite stratigraphy and sedimentology at each site. We use radiocarbon age control for piggyback basin sites above the carbonate compensation depth, and use ^{210}Pb and ^{137}Cs to evaluate the timing of the most recent sedimentary deposits. Using well-log correlation methods and radiometric age control, we test for potential correlations between isolated sites in piggyback basins and the trench.

We find evidence for very young surface turbidites along the northern Sumatra margin, most likely emplaced within the past few decades at the seafloor in both the 2004 and 2005 earthquake rupture zones, with no overlying hemipelagic sediment. Based on the young soupy deposits, lack of oxidation, and ^{210}Pb and ^{14}C age determinations, we interpret the uppermost turbidite in 21 cores within the 2004 rupture area to have been deposited within a few years of collection in 2007, and most likely as a result of the 2004 moment magnitude (M_w) ~9.2 earthquake. The likely 2004 turbidite has a distinctive stacked structure of three major fining-upward sequences observed at several basin and trench sites, similar to the pattern of moment release in the 2004 earthquake. We observe rapid die out of the 2004 and 2005 deposits with distance from the slip zones, from local sources of sediment supply, and in the segment boundary between the slip zones.

Many individual turbidites show strong similarities between isolated sites, as well as having similar emplacement times. Based upon radiocarbon age control and lithostratigraphic correlations between isolated basin and trench core sites, we interpret that 43 turbidites can be linked spatially over a distance of ~230 km within the southern portion of the 2004 rupture zone. Sampling at deep-water sites isolated from terrestrial and shallow-water sediment sources, as well as potential storm or tsunami wave triggers, limits potential mechanisms for initiating turbidity currents to plate boundary, crustal, or slab earthquakes. Other potential triggers, such as tectonic oversteepening, random self-failures, gas hydrate destabilization, are unlikely to be correlative between any two isolated sites. The most probable explanation for the similarity of timing, turbidite sequences, and individual turbidite structure in isolated basin and trench stratigraphic sequences is a seismogenic origin.

The mean emplacement time for turbidites (likely triggered by Great earthquakes, magnitude > ~8) in the 2004 rupture region for the past 6.6 ± 0.14 k.y. is 160 yr for 43 turbidites. The ages of 8 of the 10 uppermost turbidite deposits, spanning the past ~1500 yr, are largely consistent with the terrestrial paleoseismic and/or tsunami records in Thailand, Sumatra, India, and the Andaman Islands, suggesting either coincidence or a common origin. The mean interseismic time from the turbidite record for this same period is 170 yr, comparable to the ~210 yr recurrence for regional tsunami. The turbidite record, at 180 yr (6 events), compares reasonably well to the average for all events on northern Simeulue of 220 yr, and is identical to the tsunami interval of 180 yr for the same time period (6 events). Of the 43 correlated turbidites in the 2004 earthquake region, 13 are well correlated in our cores along strike lengths of 150 km or greater, and satisfy criteria for robustness; 24 turbidites correlated along a shorter strike distance may represent other plate boundary earthquakes of shorter spatial extent and may include turbidite beds sourced from crustal and slab earthquakes.

INTRODUCTION

Following the 26 December 2004 moment magnitude (M_w) ~9.2 Sumatra-Andaman and 11 March 2011 Tohoku-Oki subduction zone earthquakes and tsunamis, geologists have been reevaluating global models of subduction zone

Geosphere, published online on 12 November 2015 as doi:10.1130/GES01066.1

earthquake recurrence (e.g., Ruff and Kanamori, 1980; Shimazaki and Nakata, 1980). Given the short record of historic earthquakes (a few centuries) and the knowledge that many subduction zones have Geat Earthquake (i.e., M > 8) return periods that span multiple centuries, it has been difficult to properly document, characterize, and develop new models of their recurrence (Wesnousky, 1994; Murray and Segall, 2002; Satake and Atwater, 2007; Stein and Okal, 2007; Hindle and Mackey, 2011; Schlagenhauf et al., 2011; Colella et al., 2012; Kagan et al., 2012; Parsons, 2012; Parsons et al., 2012; Béjar-Pizarro et al., 2013; Davis et al., 2013; Goldfinger et al., 2013a; Heki and Mitsui, 2013; Ide, 2013; Kopp, 2013; Ninis et al., 2013). Many aspects of subduction zone seismogenesis have been evaluated to understand the size, timing, and contributing factors that control the outcome of future Great earthquakes (Chlieh et al., 2008; Ruff and Kanamori, 1980; Wiseman and Bürgmann, 2011); parameters include lower plate age, convergence rate, fault coupling ratio, seismicity, b-value, sediment thickness, geodesy, and other factors. Paleoseismology can reveal the temporal and spatial behavior of a fault through multiple earthquake cycles by using longer time spans than possible with historical and instrumental records (McCalpin, 2009; Goldfinger et al., 2012a). Proxies for earthquake magnitude found in the paleoseismic record may eventually provide some measure of the cycling of energy accumulation and release (stress and strain) through time (Goldfinger et al., 2012a, 2013a). Submarine (and sublacustrine) paleoseismology is advantageous for this purpose because the sedimentary record, while it includes secondary evidence for earthquakes (McCalpin, 2009), can commonly preserve very long records in great detail and provides expanded opportunities for testing spatial and temporal patterns (Goldfinger et al., 2012a, 2013a).

Strong ground shaking from earthquake rupture has been inferred to trigger turbidity currents that may deposit a very long record of past earthquakes in the form of turbidites (Dallimore et al., 2005; Enkin et al., 2013; Goldfinger et al., 2003, 2008, 2012a; Inouchi et al., 1996; Karlin and Seitz, 2007; Noda, 2004; Noda et al., 2008; Rajendran et al., 2008; Shiki et al., 2000; Nakajima and Kanai, 2000; St-Onge et al., 2004, 2012). Triggering by earthquakes, however, is far from unique; other available mechanisms must be distinguished from earthquakes, or otherwise filtered from the sedimentary record in order to develop a paleoseismic history. Methods to accomplish this have been developed for more than three decades by combining evidence from sedimentology, tests of synchroneity, stratigraphic correlation, and analysis of nonearthquake triggers. Together these criteria can be used to develop a reliable earthquake record for sublacustrine and submarine fault zones (Adams, 1990; Karlin and Abella, 1992, 1996; Karlin et al., 2004; McHugh et al., 2006; Moernaut et al., 2007; Goldfinger et al., 2012a; Gràcia et al., 2010, 2012; Pouderoux et al., 2012; Barnes et al., 2013; Smith et al., 2013; Van Daele et al., 2014, 2015, Polonia et al., 2015), although there has been dissent (Atwater and Griggs, 2012; Atwater et al., 2014; Sumner et al., 2013; Talling, 2014).

We describe our initial results from a submarine paleoseismic investigation conducted offshore of Sumatra in the region of the 26 December 2004 M_w ~9.2 earthquake (Ishii et al., 2005; Subarya et al., 2006; Chlieh et al., 2007; Stein and Okal, 2007). We introduce the geologic setting and our resulting rationale for examining the stratigraphic record for evidence of earthquakes, mixed sources, or the lack thereof. Building on an initial examination of styles of sediment transport (Patton et al., 2013a), we closely examine the marine turbidite stratigraphy and event timing to test for the possibility of regional synchronous deposition suggestive of earthquakes.

Sumatra-Andaman Subduction Zone Plate Boundary Seismicity

The 26 December 2004 M_w ~9.2 earthquake that struck Sumatra and the Andaman–Nicobar Islands (e.g., Park et al., 2005) resulted in a tsunami that inundated coastal communities around the Indian Ocean, killing more than 220,000 people. This earthquake was followed by the M_w 8.7 Nias earthquake in March 2005 (e.g., Hsu et al., 2006; Briggs et al., 2006), and by earthquakes in 2007 (e.g., Konca et al., 2008) and 2010 (Bilek et al., 2011; Newman et al., 2011). These earthquakes all ruptured sections of the megathrust between the subducting India-Australia plate and the overriding Burma-Sunda microplate (Fig. 1). The 2004–2010 earthquake series may constitute a repeating rupture series (Sieh et al., 2008). The 2004 and 2005 events were the first great subduction earthquakes in this region to be analyzed using advanced seismological and geodetic techniques.

Historic Sumatra-Andaman subduction zone (SASZ) earthquakes in the 2004 rupture zone (A.D. 1679, 1762, 1847, 1881, and 1941; Chhibber, 1934; Newcomb and McCann, 1987; Bilham, 2005; Malik et al., 2011) were much smaller (magnitude < 8.0) than the 2004 earthquake (Fig. 1). Historic earthquakes farther south along the margin were also generally of smaller magnitude (north to south: 2002 M_w 7.3; 2010 M_w 7.8; 2008 M_w 7.4; 1861 M 8.6; 1907 M_s 7.6; 1984 M 7.2; 1935 M_w 7.7; 1797 M_w ~8.6; 2009 M_w 7.5; 1833 M_w ~9; 2007 M_w 8.4, 7.9; 2004 M 7.3; 2010 M_w 7.7; 2000M_w 7.9; Newcomb and McCann, 1987; Rivera et al., 2002; Abercrombie et al., 2003; Natawidjaja et al., 2006; Konca et al., 2008; Sieh et al., 2008; Bothara et al., 2010; Kanamori et al., 2010; Philibosian et al., 2012, 2014). Recent investigations of secondary evidence left behind by tsunami as sand sheets in northern Sumatra (Monecke et al., 2008), Thailand (Jankaew et al., 2008), and the Andaman and Nicobar Islands (Rajendran et al., 2008, 2013), along with coral microatoll evidence (Meltzner et al., 2010, 2012), suggest that the penultimate subduction zone earthquake most likely occurred 500–700 yr ago, and an antepenultimate earthquake or tsunami in Sumatra (Monecke et al., 2008; Rajendran et al., 2008), the Andaman and Nicobar Islands (Rajendran et al., 2008), and India (Rajendran et al., 2007) likely occurred ~900–1200 yr ago. These initial studies suggested that recurrence of M > 8 earthquakes is ~500 yr within the past 1200 yr.

Tectonic Setting

The southern 2004 rupture was centered beneath an ~150-km-wide forearc plateau, in contrast to the typical wedge structure of many accretionary margins (Moore and Karig, 1980; Henstock et al., 2006; Fisher et al., 2007). The rupture initiated near Simeulue Island and propagated updip and northwestward at 2–2.5 km/s (e.g., Ammon et al., 2005; Ishii et al., 2005; Chlieh et al., 2007, figs.

Geosphere, published online on 12 November 2015 as doi:10.1130/GES01066.1

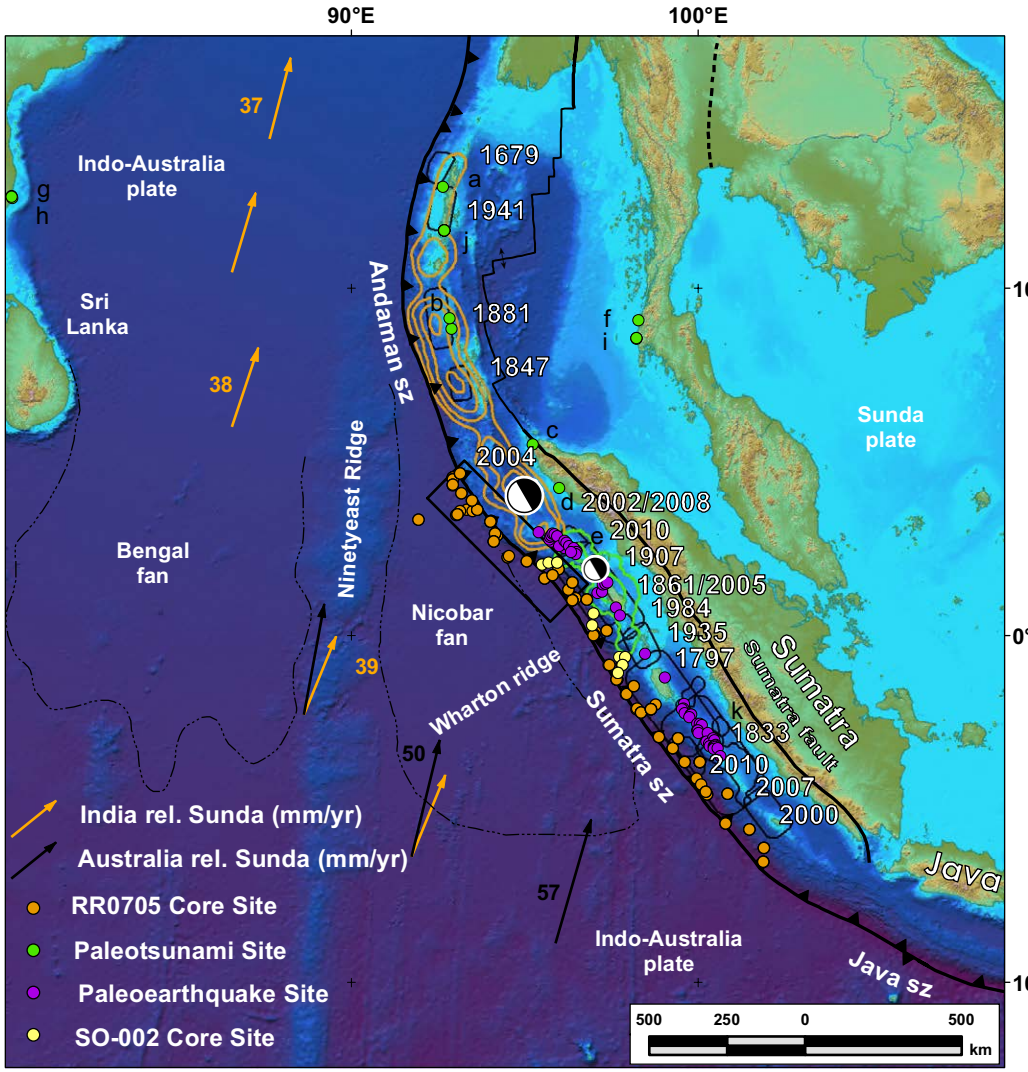

Figure 1. Plate tectonic setting. Compiled multiband single beam bathymetry and Shuttle Radar Topography Mission topography is in shaded relief and colored versus depth (Smith and Sandwell, 1997; Graindorge et al., 2008; Ladage et al., 2006). The India-Australia plate subducts northeastward beneath the Sunda plate (part of Eurasia; sz—subduction zone). Orange vectors plot India plate movement relative (rel.) to Sunda, and black vectors plot Australia relative to Sunda (global positioning system velocity based on Nuvel-1A; Bock et al., 2003; Subarya et al., 2006). Historic ruptures (Bilham, 2005; Malik et al., 2011) are plotted in gray, calendar years are in white. The 2004 and 2005 slip contours are shown in orange and green, respectively (Chlieh et al., 2007, fig. 11 therein; Chlieh et al., 2008, fig. 20 therein). Paleotsunami and paleoearthquake sites (lowercase letters) are plotted in green and purple, respectively: a, b—Rajendran et al. (2007), c—Grand-Pre et al. (2008), d—Monecke et al. (2008), e—Meltzner et al. (2010, 2012), f—Jankaew et al. (2008), g—Rajendran et al. (2008), h—Nair et al. (2010), i—Rhodes et al. (2011), j—Malik et al., (2011), k—Philibosian et al., (2012). RR0705 cores are plotted in orange, SO-002 cores are plotted in yellow (Sumner et al., 2013). Black rectangle indicates locations of Figure 3 and Supplemental File S3. Bengal and Nicobar fans cover structures of the India-Australia plate in the northern part of the map; are dashed black lines delimit their southern boundaries (Stow et al., 1990). The 2004 and 2005 earthquake focal mechanisms are plotted.

1 and 3 therein). Moment release appears to have been concentrated in three main patches that were captured in nearly all inversion models (Ni et al., 2005; Tolstoy and Bohnenstiehl, 2006; Ishii et al., 2007; Chlieh et al., 2007). In some of the seismologic records, there are more than three maxima (e.g., Chlieh et al., 2007, fig. 21, showed five or six slip maxima). Offshore northern Sumatra, the location of the greatest seismic moment release (e.g., Ammon et al., 2005), the rupture propagated relatively far seaward beneath a large part of the forearc plateau and/or prism, and was not focused beneath the forearc basins, as suggested by some models that attempted to correlate basins and gravity anomalies with the seismogenic region of subduction zones (Wells et al., 2003; Song and Simons, 2003). In contrast, slip during the 2005 rupture was concentrated further downdip beneath the forearc islands and did not propagate coseismically beneath the seaward-tapered wedge. Velocity strengthening slip occurred updip and downdip postseismically over the next few months (Hsu et al., 2006).

Geosphere, published online on 12 November 2015 as doi:10.1130/GES01066.1

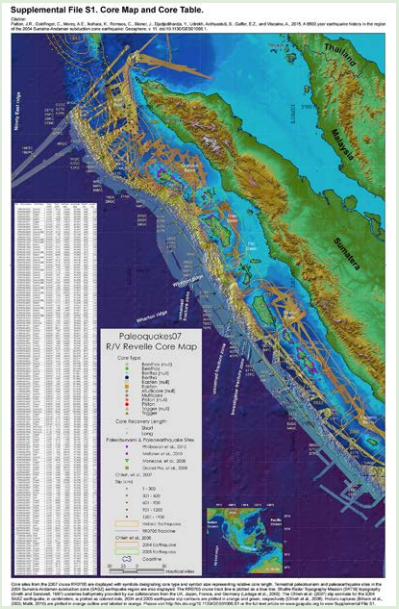

[1]Supplemental File S1. Core map and core table. Core sites from the 2007 cruise RR0705 are displayed with symbols designating core type and symbol size representing relative core length. Terrestrial paleotsunami and paleoearthquake sites in the 2004 Sumatra-Andaman subduction zone (SASZ) earthquake region are also displayed. The RR0705 cruise track line is plotted as a blue line. Shuttle Radar Topography Mission (SRTM) topography (Smith and Sandwell, 1997) underlies bathymetry provided by our collaborators from the UK, Japan, France, and Germany (Ladage et al., 2006). The Chlieh et al. (2007) slip estimate for the 2004 SASZ earthquake, in centimeters, is plotted as colored dots; 2004 and 2005 earthquake slip contours are plotted in orange and green, respectively (Chlieh et al., 2008). Historic ruptures (Bilham et al., 2005; Malik et al., 2011) are plotted in orange outline and labeled in orange. Please visit **http://dx.doi.org/10.1130/GES01066.S1** or the full-text article on www.gsapubs.org to view Supplemental File S1.

Physiography of the Sumatra-Andaman Subduction Zone

The SASZ is formed by the Indo-Australia plate, which is subducting 50–70 mm/yr at ~N30E beneath the Burma microplate of Eurasia (Fig. 1; Bock et al., 2003; Subarya et al., 2006). The continental margin morphology in western Sumatra is dominated by the upper plate structure of a Tertiary and Quaternary accretionary prism with structural highs and forearc basins (Karig et al., 1980; Fisher et al., 2007). Fold and thrust belt topography forms longitudinal, discontinuously linked basins that can be isolated, drain to other basins, or drain to the trench. Canyon systems tend to be short and drainage catchments are relatively small, limiting the potential areal extent of source areas for turbidity currents (Graindorge et al., 2008).

The rarity of longer trench-normal canyon systems is likely due to the lack of terrestrial sediment sources. Most of the northern Sumatra forearc is isolated from Sumatra by a broad unfilled forearc basin that traps sediment and isolates the outer forearc (Matson and Moore, 1992; Sieh and Natawidjaja, 2000). Some exceptions are the canyons that lead to Simeulue (2.6°N) and Nias (1.1°N) Islands. These canyons likely supply sediment from the islands to the slope basins, and potentially to the trench (Ladage et al., 2006, fig. 2 therein). Sediment input to these canyons may include turbidity currents or hyperpycnal flows related to cyclones, high swell from the Southern Ocean, or tsunami waves. The northern limit of such potential influence is 2°N, the northernmost basin that could conceivably receive sediment from Simeulue Island. The subdued or absent trench-parallel channel systems offshore Sumatra (Patton et al., 2013a) are likely due to the low late Pleistocene sedimentation rate and the interruption of the trench by subducting features. Regional transport in the trench from northern sources is thought to be cut off from Himalaya-derived sediment by a large landslide at 14°N (Moore et al., 1976) and the intersection of the Ninetyeast Ridge with the subduction zone trench (Bandopadhyay and Bandyopadhyay, 1999; Fig. 1).

The trench deepens southward from 4.5 to 6.5 km from 5°N to 7°S, and is filled with sediment several kilometers thick in the north from the Nicobar fan (a southeastern extension of the Bengal fan; Patton et al., 2013a), partially burying lower plate structures that trend across the trench (Dean et al., 2010; Graindorge et al., 2008). The outer forearc is sedimentologically isolated from northern Sumatra by a longitudinal forearc basin, which is composed of the Aceh, Simeulue, Nias, Pini, Siberut, and Bengkulu Neogene forearc subbasins (Matson and Moore, 1992; Sieh and Natawidjaja, 2000; Susilohadi et al., 2005; Supplemental File S1[1]). Lack of input from the forearc basin and from northern sediment sources results in recent sediment starvation in terms of modern inputs; thus the abyssal seafloor topography is dominated by trench-subparallel bending moment normal faults and north-striking fracture zones. The bathymetry of the forearc high is controlled largely by the blocks of sediment as much as 4 km thick (Bandopadhyay and Bandyopadhyay, 1999; Fisher et al., 2007) uplifted from the Indo-Australia plate (likely by duplexing of the accretionary complex) to form the upper part of the accretionary prism and marginal plateau (Fisher et al., 2007; Mosher et al., 2008; Gulick et al., 2011). While throughgoing submarine canyon systems are absent, short canyon systems linking some basins in short paths through the outer slope to the trench exist (Patton et al., 2013a, fig. 1 therein). The erosional style of the outer forearc is indicative of relatively high erosion rates, numerous coalescing small failures, and headward canyon migration from threshold mass wasting during dissection from erosional retreat (Howard, 1994, 1997). This erosion style, in turn, is consistent with low-cohesion sediments and is consistent with the many basins that do not drain to the trench and have an expanded Holocene section (e.g., Lamb et al., 2006). Outer forearc canyon systems have channels only on the flanks of the lower slope and these channels morphologically die out in the trench, trending to the south, within tens of kilometers from the canyon mouths. Limited channel development suggests moderate mixing of turbidity currents dominated by proximal sedimentary processes (Patton et al., 2013a).

Turbidite Paleoseismology and Rationale as Applied to the Northern Sumatra Margin

Primary evidence of past earthquakes generally involves the identification of sedimentary deposits (including soils) that have been offset by fault rupture, typically found in an excavation across the fault (McCalpin, 2009). Secondary evidence of past earthquakes is interpreted from sedimentary deposits that contain evidence of fault motion from an earthquake (Atwater, 1987; Atwater and Hemphill-Haley, 1997; Goldfinger, 2009). The paleoseismology of subduction zone faults is primarily based on secondary evidence because the subduction zone fault is located in the submarine setting, where fault trenching is not yet possible. Examples of secondary evidence for subduction zone earthquakes include tsunami deposits (Hemphill-Haley, 1995), buried marsh soils (Atwater, 1987), landslides (Wilson and Keefer, 1985; Schulz et al., 2012), and turbidites (Adams, 1990; Goldfinger et al., 2003; Pouderoux et al., 2012).

Applicability to a Variety of Settings

Turbidite paleoseismology in sublacustrine and submarine environments has been applied in numerous localities globally, under a variety of conditions of climate, sedimentation rate, and subaqueous setting (methods used in each study are listed in parentheses): Lake Baikal (whole core and surface scanning magnetic susceptibility; Lees et al., 1998a, 1998b), Ecuador (correlation of mass transport deposits, MTDs, and the comparison between return times of MTDs, turbidites, and earthquakes; Ratzov et al., 2010), Iberian margin (turbidite chronologic correlation, interturbidite hemipelagic thicknesses, core geophysics, and geochemical composition; Gràcia et al., 2010), Kumano Trough, Japan (particle size, ^{137}Cs geochronology, X-ray radiography, and bulk density; Shirai et al., 2010), Lake Washington, Washington (core geophysics, X-ray radiography, and particle size; Karlin and Abella, 1992, 1996; Karlin et al., 2004), Lake Tahoe, California (sediment core isotopic correlation, anisotropic magnetic susceptibility, and ^{14}C geochronology; Karlin and Seitz, 2007), Okinawa Trough, Japan (correlation of core porosity and particle size, ^{210}Pb and

Geosphere, published online on 12 November 2015 as doi:10.1130/GES01066.1

^{137}Cs, and comparison of turbidite return timing; Huh et al., 2004, 2006), central Switzerland (historic earthquake timing compared to ^{14}C geochronology, high-resolution seismic data, and sedimentary structures; Monecke et al., 2006), Saguenay Fiord, Canada (biotracers, mass physical properties of sediment cores, and high-resolution seismic and sidescan profiles; Syvitski and Schafer, 1996; St-Onge et al., 2004), Canadian Arctic (sediment provenance and sediment accumulation rates; Grantz et al., 1996), Kuril trench (correlation based upon lithology, sand grain composition, and ^{14}C, ^{210}Pb, and ^{137}Cs chronology; Noda et al., 2008), Lake Biwa, Japan (sedimentation rate chronology compared with historic earthquake records, X-ray radiographs, and correlation of core geophysical data, i.e., density, Inouchi et al., 1996; sedimentary structures and grain-size distribution, Shiki et al., 2000), the southern margin of Japan (magnetomineralogical fabric analysis; Abdeldayem et al., 2004), Cascadia (core geophysics, confluence test, and ^{14}C chronology; Goldfinger et al., 2003; 2012a; Gutiérrez-Pastor et al., 2005a, 2005b, 2009, 2013; Enkin et al., 2013; Blais-Stevens et al., 1997, 2011; Blais-Stevens and Clague, 2001), the northern San Andreas fault in California (core geophysics, confluence test, and ^{14}C chronology; Goldfinger et al., 2003, 2008); south and south-central Chile (high-resolution reflection seismic profiles, comparison to historic earthquakes, particle size, and X-ray radiograph computed tomography scanning; Moernaut et al., 2007; Van Daele et al., 2014), Gulf of California (Gonzalez-Yajimovich et al., 2007), the Santa Barbara basin (turbidite volume and submarine distribution in km^2, comparison with historic flood and earthquake records; Gorsline et al., 2000), eastern Japan Sea (correlation between seismic reflection data and sediment core, ^{137}Cs chronology, and comparison with historic earthquake, turbidite structure, particle size, sediment composition; Nakajima and Kanai, 2000), central Mediterranean (grain size, core geophysics, X-ray imagery, geochemistry, mineralogy, and micropaleontology; Polonia et al., 2013a, 2013b), and Marmara Sea (^{14}C chronology compared with historic earthquakes, lithological composition; McHugh et al., 2006; Sarı and Çağatay, 2006; Çağatay et al., 2012; McHugh et al., 2014).

Earthquakes are well known as subaerial landslide triggers, with a possible minimum triggering earthquake magnitude of M ~ 5 (Keefer, 1984). Landslide density is found to be greater in areas of stronger ground acceleration (Meunier et al., 2007). Earthquake magnitude thresholds for submarine landslides are less well constrained than subaerial landslides (suggested as M ~ 7.1 in Cascadia; Goldfinger et al., 2012a, 2013a; M 7.4 in Japan, Nakajima and Kanai, 2000; M 7.3 in northern California and Cascadia, Wilson and Keefer, 1985; M 5.2 in Venezuela, Lorenzoni et al., 2012), probably because the evidence of minimum values is largely lacking. Black (2014) estimated a global average minimum value of Modified Mercalli Intensity (MMI) 5.5 for existing studies, although minimum value estimates are rare. Earthquakes are posed as one of the dominant submarine landslide triggers (Ross, 1971; Almagor and Wiseman, 1991; Hampton et al., 1978, 1996; Masson et al., 2006), with most historic examples attributed to ground accelerations from earthquakes (Mosher et al., 2010).

Submarine landslides may transform into turbidity currents that leave behind turbidites (Morgenstern, 1967; Stow and Bowen, 1980; Felix and Peakall, 2006), known as seismoturbidites or seismites when earthquake triggered. Turbidity currents are turbulence driven (autosuspension) sediment-rich gravity flows (Bouma, 1962; Middleton, 1967; Kneller and Buckee, 2000). The sedimentary sequence of an individual deposit reflects the time history of deposition from the turbidity current as it passes a sedimentary depositional setting (Baas et al., 2004). The vertical structure of a turbidite is a sampling of the longitudinal velocity and density structure of the causal turbidity current (Lowe, 1982; Kneller and McCaffrey, 2003). Early assumptions were that turbidity currents are the result of a single impulse of sediment into the system and that multiple fining-upward sequences were due to erosion of older deposits by younger currents (Ericson et al., 1952; Kneller and McCaffrey, 2003). More recent studies have revealed that the input of sediment into the turbidity current was not always singular, but was likely formed from a temporally heterogeneous flux of sediment (Lowe, 1982; Piper et al., 1999; Nakajima and Kanai, 2000; Kneller and McCaffrey, 2003; Goldfinger et al., 2008, 2012a; Gutiérrez Pastor et al., 2013). Local geologic variability and hydrodynamic factors may also contribute to the longitudinal variability of the turbidity current and, therefore, the vertical structure of a turbidite. For this and other reasons, it is difficult to interpret the physical components of a turbidite based on a single or a few cores without having core data sampled from upstream and downstream within the same channel system (Kneller and McCaffrey, 1995), and within multiple systems in the case of regionally triggered currents.

In Adams (1990) and Goldfinger et al. (2003, 2012a), eight plausible triggering mechanisms for turbidity currents were suggested: storm wave loads, earthquake loads, tsunami wave loads (local or distant), sediment loads, hyperpycnal flows, volcanic explosions, submarine landslides, and bolide impacts. In addition to these triggers, tidal bottom currents may be included in this list (Thomson et al., 2010). Of the possible landslide triggers listed in Adams (1990), Sultan et al. (2004), Goldfinger (2010), and Goldfinger et al. (2012a), only bolide impacts, hyperpycnal flows, tides, wave loads, and earthquakes can directly trigger submarine landslides, as other phenomena may simply precondition the slope for failure (Goldfinger et al., 2012a). This subset of triggers can be evaluated in terms of plausibility, expected frequency, sedimentology, aerial extent, and correspondence to other evidence onshore and other factors. Some suggest that turbidite structure is evidence that autocyclic forcing dominates turbidite deposition (Kneller and McCaffrey, 2003; Dennielou et al., 2006), but they do not consider a longitudinal change in sediment flux within the turbidity current. Others suggest that the allocyclic forcing of turbidity currents is preserved in the turbidite structure because the current flows were triggered by a shared source, possibly due to earthquakes (Goldfinger and Morey, 2004; Garrett et al., 2011; Goldfinger, 2011; Goldfinger et al., 2012b). Amalgamation is posed as an indicator that the turbidites were deposited from multiple turbidity currents, merging and forming a longitudinal structure reflected in the deposit (Nakajima and Kanai, 2000), possibly from multiple slides on slopes. In Lake Biwa, Nakajima and Kanai (2000) concluded that these multiple pulses are the results of synchronous triggering of multiple parts of the canyon system. Turbidite structure is likely a combination of

Geosphere, published online on 12 November 2015 as doi:10.1130/GES01066.1

these multiple factors. In Goldfinger et al. (2003, 2007, 2008, 2012a) and Goldfinger and Morey (2004), a seismogenic trigger to Cascadia and northern San Andreas turbidity currents was attributed through stratigraphic correlation of turbidites with shared sedimentary structures (i.e., fingerprints), supported by a framework of depositionally constrained radiocarbon ages and relative age tests, demonstrating that they represent synchronous deposition (Goldfinger et al., 2012a, 2013b).

The study of turbidite paleoseismology is best developed for the Cascadia subduction zone (CSZ; Goldfinger et al., 2012a, 2013a). The seminal work of Adams (1990) used a tephra datum (Mazama ash, ca. 7.7 ka; Bacon, 1983; Zdanowicz et al., 1999; Klug et al., 2002; Bacon and Lanphere, 2006) and a confluence of separate channels to constrain the number of turbidites above the tephra in each core (confluence test; Adams, 1990). This confluence test is, in part, the basis of the original case for seismogenic triggering of these turbidity currents. What also contributed to the success of the work in Cascadia was the extensive research done on both the turbidite systems offshore and the terrestrial paleoseismology in the region; this provided a chronologic framework with which to compare the submarine results (Duncan, 1968; Nelson, 1968; Nelson et al., 1968; Barnard, 1973; Griggs, 1969; Carlson, 1967; Nittrouer, 1978; Atwater, 1987; Atwater and Hemphill-Haley, 1997; Kelsey et al., 2002). Although several alternatives have been proposed based on 1960s core logs (Atwater and Griggs, 2012; Atwater et al., 2014), modern bathymetric, backscatter, and core data show these alternatives to be either too old, or nonexistent (Beeson and Goldfinger, 2013; Goldfinger et al., 2013a, 2014b). While others suggested that the CSZ might be seismogenic, using uplifted topography and rates of secular vertical motion (Adams, 1984), Atwater (1987) found the first geologic evidence of paleotsunami and paleodeformation related to subduction zone earthquakes along the CSZ in the form of sand sheets overlying coseismically subsided intertidal to supratidal deposits. Thereafter, more evidence of paleodeformation, paleotsunami, and paleoliquefaction was found and compiled into a catalog of paleoseismic events that had variations in space and time (Peterson and Madin, 1997; Obermeier and Dickenson, 2000; Kelsey et al., 2002; Leonard et al., 2004, 2010; Kelsey et al., 2005; Nelson et al., 2006; Goldfinger et al., 2008, 2012a; Graehl et al., 2014). Onshore, it was not possible to directly correlate stratigraphic evidence from site to site because the terrestrial sedimentary evidence was discontinuous between sites north to south and radiocarbon uncertainties preclude establishing synchronous occurrence (Nelson et al., 2006). It was not until the submarine record was developed that the spatiotemporal links could be made between offshore sites, with less certainty, to the existing terrestrial records (Goldfinger et al., 2008, 2012a; Witter et al., 2011, 2013). Unfortunately such an extensive terrestrial record for past earthquakes is not well developed for the SASZ.

In this paper we test the plausibility of a seismogenic trigger as a source for the observed turbidite stratigraphy in northern Sumatra primarily by (1) using tests for synchronous triggering of sedimentologically isolated turbidite systems and (2) using sedimentologic characteristics (e.g., structure) of the turbidites. We apply both lines of investigation to aid in discrimination between potential seismic and nonseismic trigger sources. Radiocarbon age estimates provide constraints to broadly establish the temporal stratigraphic sequences and to compare sequences between multiple sites. While individual radiocarbon ages have the same temporal limitations in the sea that they do onshore, in the marine environment, interevent sedimentation provides an independent temporal reference that can be used in integrated age models to improve precision and reduce uncertainties (Bronk Ramsey, 1995, 2009a, 2009b; Gutiérrez-Pastor et al., 2009; Goldfinger et al., 2012a; Enkin et al., 2013). Lithostratigraphic correlations and radiocarbon constraints can form a robust test of continuity of depositional sequences among sites (Goldfinger et al., 2012a).

Approach for Sumatra

Our rationale in Sumatra differs from that of Cascadia in several important ways, as the margin physiography and water depth range require a different approach. In general, our strategy was to seek sites that were sedimentologically isolated from terrestrial sediment sources and from each other. Limiting landslide trigger types is the initial filtering method we use to simplify the paleoseismic problem. Isolated deep-water sites with no terrestrial or shallow-water sediment source areas eliminate storm and tsunami wave loading, hyperpycnal flow, and to some extent self-failure due to sediment accumulation, leaving crustal, slab, and plate boundary earthquakes and localized self-failures as possible trigger mechanisms. With the problem reduced to the simpler case, if turbidites can be correlated between isolated sites separated by large distances, synchronous triggering and earthquake origin is likely; otherwise no correlation nor similarity of turbidite sequences is expected. Individual links are commonly subject to the uncertainties in correlation and radiometric age control, thus a large number of sites is preferred in order to improve the signal to noise ratio in the event that a coherent signal exists (Goldfinger et al., 2003, 2008, 2012a; Shiki, 1996; Gorsline et al., 2000; Nakajima, 2000; Shiki et al., 2000).

METHODS

We used primarily 10-cm-diameter piston and gravity cores to collect turbidite stratigraphy, supplemented with Kasten cores, box core, and multicores (the latter two are used to sample the sediment-water interface and the uppermost units with minimal disturbance); 20 cm by 20 cm square Kasten cores are useful because they provide a larger volume of sediment from which volume restricted age samples ($CaCO_3$ foraminiferid tests) are collected.

Site Selection and Coring

As in all geologic and paleoseismic investigations, selecting the best sites is critical in submarine paleoseismology (Goldfinger et al., 2014b). We use continental margin physiography to narrow the selection of sites to those most likely to preserve seismoturbidites, while seeking to exclude as many other

Geosphere, published online on 12 November 2015 as doi:10.1130/GES01066.1

sedimentary sources as possible. We sought core sites that would be most likely to preserve stratigraphy with deposits that have the greatest dynamic range in particle size (texture) above the background sediment particle size or density and with an expanded stratigraphic section. With a large dynamic range in texture, the distinction between hemipelagic mud and turbidite sediment is enhanced and vertical separation between turbidite deposits is increased. This distinction is important for calculating background sedimentation rates and sampling for age control. A large dynamic range in texture also helps with stratigraphic correlation (discussed in the following). Core sites that are too distal have turbidites with very little variation in density and particle size (Kneller and McCaffrey, 2003), making it difficult to characterize the structure of any given deposit. Distal sites in an unchannelized setting may fade very rapidly from local sources (Nelson et al., 1986; Baas et al., 2004, 2005; Johnson et al., 2005; Goldfinger et al., 2012a, 2014a, 2014b; Patton et al., 2013a). Conversely, core sites that are too proximal are commonly dominated by a series of amalgamated debrites (Bouma, 2004), making interpretation problematic.

Our rationale for selecting core sites also considers issues of age control, sedimentary isolation, and geospatial relevance to historic and prehistoric fault segments. We selected core sites in slope basins due to the absence of usable radiocarbon material in cores collected in the trench below the carbonate compensation depth (CCD). A benefit of these slope basin core sites is that they typically have isolated submarine landslide source areas. However, this is also a disadvantage for paleoseismology as most coring sites are therefore more proximal to their source, which may result in noisier and less distinguishable sedimentary structure that is more difficult to compare from site to site. We also collected a suite of trench cores paired for the most part with basin cores to test whether these could be correlated to the basin sites that have age control.

We initially focused our efforts on the basin-to-basin correlations because the addition of radiocarbon strongly constrains stratigraphic sequence comparisons. As in Cascadia, we began by correlating piston and trigger cores, then progressed to the nearest and least ambiguous sites. We then addressed more and more distant and or difficult sites. While basin sites are discrete spatially, trench sites have potential for along-trench transport, thus smearing the signal from earthquakes (or any source) along strike. The lack of long trench-parallel channel systems in Sumatra suggests that a given turbidity current will not travel a sufficient distance along the trench axis and confound its association with a given earthquake by its spatial extent and position alone, perhaps mitigating this problem to some extent.

We are not only interested in developing a chronology of earthquakes along this subduction zone, but we are also interested in investigating the spatial limits of past earthquake ruptures. Because most subduction zones and other major faults exhibit segmentation, and segmentation in historical and paleoseismic data in Sumatra strongly suggested it, we initially adopted these segments as an initial testable hypothesis. We used the proposed segments (Kopp et al., 2008) to guide our core site selection, although we did not have enough spatial coverage to discretely test all the segments rigorously. While this premise was untested in 2007, it has subsequently been supported by onshore paleoseismic work (Jankaew et al., 2008; Monecke et al., 2008; Sieh et al., 2008; Fujino et al., 2009; Meltzner et al., 2010, 2012; Dura et al., 2011; Philibosian et al., 2012, 2014). We chose core sites that are within these historic and recent prehistoric segments, as well as at the segment boundaries. Trench cores are more likely to include records from adjacent slip regions because the trench may transport these turbidity currents. The slope cores are less likely to do so, due to their smaller source areas and shorter transport paths parallel to the margin. The boundaries received less emphasis because they commonly have reduced earthquake slip and confusing records (Goldfinger et al., 2014a, 2014b). Because the effects of earthquakes taper rapidly with distance from the fault slip (deformation: Natawidjaja et al., 2004, 2006; Meltzner et al., 2006, 2010, 2012; Sieh et al., 2008; Philibosian et al. 2012; ground shaking: Arias, 1970; Keefer, 1984; Wilson and Keefer, 1985; Wilson, 1993; Campbell, 1997; Kayen and Mitchell, 1997; Youngs et al., 1997; Atkinson and Boore, 2003, 2011; Travasarou et al., 2003; Sorensen et al., 2007; Boore and Atkinson, 2008; Zhao and Xu, 2012; Black, 2014), the sedimentary evidence of these earthquakes may also be spatially limited. Sites that receive sedimentary input that was transported in the trench would violate this spatial limit premise (Black, 2014). Cores that are near segment boundaries may be difficult to correlate because they may either have diminished sedimentary records (deposits with lower dynamic range of density or lesser developed structure) or have records from the overlapping fault segments (possibly for larger magnitude earthquakes). At a more local scale, we selected sites close to local slopes and near the outlets of local canyons. Experience in Cascadia (Goldfinger et al., 2012a) has shown that unchannelized flows may have short run-out distances, thus broad basins were avoided. Our initial efforts have focused primarily on evidence in the region of the 2004 SASZ earthquake and other areas will be considered subsequently.

Multibeam mapping was essential for evaluating the physiographic setting for the relevant sedimentary systems. Multibeam bathymetry and backscatter data were collected with the Kongsberg EM-120 system on the R/V *Roger Revelle*, and edited on board using MBSystem (http://www.mbari.org/data/mbsystem/) so that coring sites could be chosen in real time (Patton et al., 2007; *Roger Revelle* Cruise RR0705 Superquakes07 cruise report, http://www.activetectonics.coas.oregonstate.edu/sumatra/report/index.html). Prior to the cruise, existing bathymetric data were compiled. Sumatra bathymetry was collected by expeditions (R/V *Natsushima*—Japan Agency for Marine Earth-Science and Technology, Jamstec; HMS *Scott*—UK Royal Navy and Southampton Oceanography Centre, NOCS; R/V *Marion Dufresne*—Institut Français de Recherche pour l'Exploitation de la Mer, IFREMER; R/V *Sonne*—German Federal Institute for Geosciences and Natural Resources, BGR) and shared utilizing a cooperative agreement with these international institutions and the Indonesian Government (Agency for the Assessment and Application of Technology, BPPT), without which our coring study would not have been possible (Henstock et al., 2006; Ladage et al., 2006). The EM 120 has a depth resolution of 10, 20, and 40 cm, for pulse lengths of 2, 5, and 15 ms, and covers depth ranges

Geosphere, published online on 12 November 2015 as doi:10.1130/GES01066.1

from 20 to 11,000 m. The resulting 100 m grid cell size is a function of the best resolution of the systems used. Several areas of higher (50 m) resolution data collected on the HMS *Scott* are also available for the outer Sumatra forearc in the 2004–2005 rupture areas (Tappin et al., 2007). After editing the raw data, we visualized and rendered the bathymetric data using Fledermaus (www.qps.nl/display/fledermaus) and ArcGIS (www.esri.com/software/arcgis) software applications in order to plan for potential core sites.

We extensively used 3.5 kHz compressed high-intensity radar pulse (CHIRP) shallow subbottom profiles to survey Holocene turbidite stratigraphy in trench and slope basins to aid in core site selection. We used a Knudsen 320BR (FM CHIRP mode typically sweeping 2–6 kHz) at full bandwidth and data rate. These lines were heave corrected in real time using the ships' PosMV320 motion sensor. We postprocessed the data using Sioseis (http://sioseis.ucsd.edu/sioseis.html; Henkart, 2011) using band pass filtering, muting, and a heave-filtering algorithm. Digital correlation processing of the CHIRP signal reduces the effective frequency, improving the signal to noise ratio and boosting the effective vertical resolution to ~25 cm, degraded somewhat by off-axis scatterers, vessel motion, and the water column. In addition to the utility of developing a potential core site, these seismic reflection data can reveal the continuity (or lack thereof) of repeated local turbidite sedimentation, local faulting, and mass wasting deposits both within and between sites.

After we selected a core site, we typically deployed a 6.66-cm-diameter gravity corer. This core was used as a reconnaissance tool due to the higher velocity that the core can be deployed to the seafloor (100 m/min, versus 40 m/min for larger diameter cores). For sites where good turbidite stratigraphy was found, we then deployed a 10.14-cm-diameter piston-trigger core pair. Due to equipment failures (sheave bearings below deck were incapacitated due to high temperatures near the equator), piston cores were mostly deployed on a railroad track constructed from spare parts mounted to the stern deck using the stern A-frame. This configuration limited the length of the piston corer to 2 core sections (10 ft each), with a maximum coring depth of 6.09 m. Trigger cores had a maximum coring depth of 3.05 m. The 1000–2200 kg weight stand (attached to the piston corer) drives the piston core into the seafloor with greater velocity than the trigger corer (possibly eroding surface sediment from the seafloor), thus core tops are occasionally lost from the piston core, but typically not the trigger or multicores (unless due to overpenetration). Kasten cores, box cores, and multicores collect the uppermost sediments in greater volume and detail.

All cores were scanned for geophysical properties (multisensor core logging including gamma density, low-resolution magnetic susceptibility (MS) using a loop sensor, P-wave velocity, and resistivity). Cores were then split lengthwise and imaged with a GeoTek high-resolution line-scan camera and described on lithostratigraphic data sheets including onboard micropaleontologic, mineralogic, and tephra data collection. We adopted the sedimentary terminology of laminae and beds from Campbell (1967). Subsequently, high-resolution point MS data were collected from each core using a point sensor (Bartington MS2E high-resolution surface sensor) at 0.5 or 1 cm intervals. Following the cruise, cores were then scanned with computed tomographic X-ray techniques (CT scans) using a Toshiba Aquilion 64 slice CT unit at 0.5 mm voxel resolution. CT data permit a refined view of the strata and the effects of core disturbance in high resolution and in three dimensions. CT data also provide densostratigraphic information (downcore variation in density) when CT imagery is used for downcore line-scan analysis. Gamma and magnetic data reflect signals that average these effects over a vertical distance related to the amount that the sediment is disturbed vertically. Grain-size analysis was done using laser diffraction particle size measurements using a Beckman-Coulter LS 13 320 laser counter (Blott and Pye, 2006) with a Fraunhofer based polarization intensity differential scattering optical model. Particle size analyses are limited to a size range of 0.040–2000 μm. In a limited number of cores we collected downcore X-ray fluorescence measurements and superconducting rock magnetometer measurements of natural remnant magnetization. Accelerator mass spectrometry (AMS) ^{14}C radiocarbon analyses, and ^{210}Pb and ^{137}Cs isotopic analyses were performed for age control. We also conducted neutron activation analysis on a multicore, seeking evidence of short-lived radionuclides and isotope chemistry. Core geophysical methods and radiometric age analyses are further summarized in Supplemental File S2[2].

Age Control

Age control for stratigraphy is provided by AMS ^{14}C, ^{137}Cs, and ^{210}Pb radiometric techniques. The ^{14}C data are based on decay with a half-life of 5730 yr and are useful for strata to ~50,000 yr old (Stuiver and Polach, 1977; Stuiver and Braziunas, 1993; Hughen et al., 2004; Fairbanks et al., 2005; Reimer et al., 2009, 2013). The ^{210}Pb data, based on a shorter half-life of 22.3 yr (Noller, 2000; Faure and Mensing, 2005), provide information about sedimentary deposition for the past ~150 yr. The ^{137}Cs data are based on the half-life of 30.17 yr (Faure and Mensing, 2005), but may have a shorter effective half-life closer to a decade (Robison et al., 2003). The ^{137}Cs age data can reveal the timing of sedimentation after A.D. 1952 (Robbins et al., 1978). We use ^{210}Pb and ^{137}Cs age data to constrain the timing of deposition for the most recently deposited sediments. While ^{210}Pb and ^{137}Cs have similar half-lives, ^{210}Pb input is continuous, while ^{137}Cs input is episodic (Faure and Mensing, 2005); the peak input for ^{137}Cs was during 1962–1963 as a result of fallout from above-ground nuclear testing. Nuclear accidents, like Chernobyl, are an additional source of ^{137}Cs (Faure and Mensing, 2005); ^{137}Cs has been detected in seawater (Alam et al., 1996) and sediments (Michels et al., 2003) in the northern Bay of Bengal.

In order to evaluate the timing of the possible 2004 turbidite with radiometric techniques, we collected sediment samples below the turbidite at 1 cm spacing. The ^{210}Pb samples were prepared and analyzed at the Institut des Sciences de la Mer de Rimouski (Flynn, 1968; St-Onge, 2004; Levesque et al., 2006). Other ^{210}Pb samples and ^{137}Cs samples were prepared and analyzed using gamma counting methods with the assistance of Rob Wheatcroft at Oregon State University (Gilmore and Hemingway, 1995; Wheatcroft and Sommerfield, 2005).

Citation:
Patton, J.R., Goldfinger, C., Morey, A.E., Ikehara, K., Romsos, C., Stoner, J., Djadjadihardja, Y., Udrekh, Ardhyastuti, S., Gaffar, E.Z., and Viscaino, A., 2015, A 6500 year earthquake history in the region of the 2004 Sumatra-Andaman subduction zone earthquake: Geosphere, v. 11, doi:10.1130/GES01066.1.

Supplemental File S2 Core Geophysics and Age Control Methods

Core Geophysics

The 109 cores collected offshore Sumatra (Supplemental File S1) were scanned at sea with a GEOTEK Multi Sensor Core Logger (MSCL), obtaining P-wave velocity, gamma ray density, resistivity, and loop magnetic susceptibility (MS) at 0.5 cm spaced intervals in 1.5-m length sections. Split cores were imaged with a high resolution line-scan digital camera and the lithostratigraphy was described. High resolution point MS data were collected using a Bartington MS2E point sensor at 0.5 cm spacing. The cores were imaged with the Oregon State University Aquilion 64 slice X-ray Computed Tomography (CT) system with a nominal voxel size of 0.5 mm.

Age Control Methods

Age control for stratigraphy is provided by Accelerator Mass Spectrometer (AMS) ^{14}C and ^{210}Pb radiometric techniques. ^{14}C data is based on decay with a half-life of 5,730 years and is useful for strata between ~300 - ~35,000 years old (Stuiver and Braziunes, 1993). ^{210}Pb data, based on a shorter half-life of 22 years (Noller, 2000), provides information about sedimentary deposition for the past ~150 years. We use ^{210}Pb age data to constrain the timing of deposition for the most recently deposited sediments.

To estimate ages of the turbidites using radiocarbon, we extract the calcium carbonate shells of planktic foraminifers preserved in the hemipelagic sediment below each turbidite to provide a maximum limiting age. We utilized planktic foraminiferid species as they most closely represent the age of the youngest sea water, the surface water that is most closely in ^{14}C equilibrium with the atmosphere. We sample below each turbidite because this is the sediment closest in age to the turbidite. We do not use the age of the sediment above the turbidite because the boundary between the top of the turbidite tail and the hemipelagic sediment is difficult to identify reliably and bioturbation is concentrated at this boundary. These methods are outlined in Goldfinger et al. (2012 a).

Supplemental File S2. Core Geophysics and Age Control Methods. A general overview of core geophysics acquisition methods is first presented. Age control methods are then discussed. The OxCal code for the regional age model is presented, followed by the output "log" file and a plot of the probability density functions for this age model. Please visit http://dx.doi.org/10.1130/GES01066.S2 or the full-text article on www.gsapubs.org to view Supplemental File S2.

[2]Supplemental File S2. Core geophysics and age control methods. A general overview of core geophysics acquisition methods is presented; age control methods are discussed. The OxCal code for the regional age model is presented, followed by the output "log" file and a plot of the probability density functions for this age model. Please visit **http://dx.doi.org/10.1130/GES01066.S2** or the full-text article on www.gsapubs.org to view Supplemental File S2.

Geosphere, published online on 12 November 2015 as doi:10.1130/GES01066.1

To estimate the ages of the possible turbidite using ^{210}Pb, we derive a sedimentation rate and use hemipelagic sediment thicknesses to estimate the age of the youngest turbidite. We calculate the sedimentation rate for sediment in core 96PC using the methods from Ghaleb (2009). We use the thickness of overlying hemipelagic sediment to calculate the timing of deposition for this turbidite from above. We also use the thickness of hemipelagic sediment beneath the possible 2004 turbidite and above a ^{14}C age determination to estimate the timing of deposition for this turbidite.

To estimate the ages of the turbidites using radiocarbon, we extract the calcium carbonate tests of planktic foraminifers preserved in the hemipelagic sediment below each turbidite to provide a maximum limiting age. We utilize planktic foraminiferid species because they most closely represent the age of the youngest seawater, the surface water that is most closely in ^{14}C equilibrium with the atmosphere. We sample below each turbidite because this is the sediment closest in age to the turbidite. We typically do not use the age of the sediment above the turbidite because the boundary between the top of the turbidite tail and the overlying hemipelagic sediment is difficult to identify reliably, and bioturbation is also concentrated at this boundary (methods outlined in Goldfinger et al., 2012a).

Sources of sampling error include basal erosion, sediment deformation from coring, differences in stratigraphic thickness between cores, and bioturbation. Some of these factors cannot be evaluated readily because of the coring-induced deformation of stratigraphic thickness and sedimentary structure (aleatory uncertainty; how well the sediment cores represent the real sedimentary thicknesses). Bioturbation is difficult to evaluate as a factor controlling age estimates because we do not have multiple cores in a single location that have both bioturbated sedimentary section and nonbioturbated sedimentary section. Erosion can be estimated in some cases (Goldfinger et al., 2012a), but the tests require multiple cores at a site, and thus we are unable to test this factor due to the lack of multiple cores at most sites. We attempted to estimate erosion using cores that were collected nearby (<10 km); however, some of these were not good candidates due to complex turbidite structure, bioturbation, or coring deformation. These confounding factors made it difficult to distinguish hemipelagic sediment from turbiditic sediment well enough to be useful in our interpretation.

Other sources of uncertainty include factors that affect some of our assumptions regarding how well the sediment age actually represents the time of deposition for the turbidite. Sources of this type of epistemic uncertainty include (1) changes in the age of the surficial seawater at the time of deposition; (2) changes in carbon export to the seafloor (rate of foraminiferid sedimentation); and (3) changes in species distribution through time. Changes of the age of seawater can be affected by upwelling, which brings older water to the surface, making the sediment appear older in radiocarbon years. If carbon flux to the seafloor increases during the time frame that the sample thickness represents, the age determination would be biased to an age representing the higher carbon flux (this would change the concentration of foraminiferid tests per unit volume of sediment, biasing the age toward the time that had a higher concentration of foraminiferid tests). If the species distribution changes through time (i.e., if deeper shallow-water species might dominate) the age of the sediment would be different. While we do not think errors 2 and 3 are significant, we do not have sufficient data to evaluate or test these sources of epistemic uncertainty. Error 1 is discussed in the following.

Sediment samples were removed from the cores while avoiding the 0.5 cm of material nearest the core walls to avoid visible or undetected deformation and friction drag along the core walls. In some cases highly irregular turbidite bases resulted in sampling an interval below the basal irregularities. We corrected these ages by subtracting the time represented by the sediment gap. Hemipelagic sediment samples were freeze-dried to separate clay particles to improve rinsing through a sieve, washed in a dilute Calgon (sodium hexametaphosphate) solution to keep the fine particles in suspension, sieved through a 125 µm stainless steel sieve, then dried in a warm oven. Typically 25–50 individual planktic foraminifers (depending on size and mass) are identified and removed from this dried >125 µm size fraction using a fine sable brush moistened with distilled water. Foraminiferal sample ages are determined using AMS methods at the Keck AMS facility at University of California, Irvine, in collaboration with John Southon.

Radiocarbon age reporting follows a set of standards (Stuiver and Polach, 1977). Laboratory radiocarbon ages are reported in years before present, B.P. (measured from A.D. 1950) with a 2 standard deviation laboratory error (Stuiver et al., 1998). We used OxCal V 4.2.3 to calibrate ^{14}C ages (Stuiver and Braziunas, 1993; Bronk Ramsey, 2009a, 2009b; Reimer et al., 2013). We applied a marine reservoir correction to account for the marine reservoir for marine radiocarbon samples. In addition to the global marine reservoir value, we apply an additional regional correction (ΔR) of 16 ± 78 yr using the IntCal13 and Marine13 databases (Reimer et al., 2013). Only two ΔR values are available for the Sumatra area and these (like nearly all ΔR values globally) are based on latest Holocene ages (located north and south of Sumatra). Squire et al. (2013) used samples along the Abrolhos Islands offshore of Western Australia and found ΔR for the past 3000 yr to be stable and to range from 54 ± 30 yr; their calculations are consistent with estimates made for sites between northwestern Australia and Java, 60 ± 38 yr (Gillespie, 1977; Gillespie and Polach, 1979; Bowman and Harvey, 1983; Bowman, 1985; Southon et al., 2002; Hua et al., 2004, and references therein; O'Connor et al., 2010). The ΔR value for the Cocos Islands, eastern Indian Ocean, is 66 ± 12 yr (Hua et al., 2004). Dutta et al. (2001) suggested that the variation in ΔR in the northern Indian Ocean is due to variations in the thermocline ventilation rates. Hua et al. (2004) suggested that the lower values of ΔR in the eastern Indian Ocean are because surface waters are influenced by seawater from the western Pacific sourced via the Indonesian Throughflow. These ΔR values are stable even given the increased potential variability imparted by ENSO (El Niño Southern Oscillation) and the influence of the western Pacific on the Indian Ocean via the Indonesian Throughflow (McGregor et al. 2008; Yu et al. 2010). The ΔR values decrease in magnitude from south to north, with the lowest values at the northern and southern tips offshore the Island of Sumatra (used in our analysis; Southon et al., 2002). Given the small variation

Geosphere, published online on 12 November 2015 as doi:10.1130/GES01066.1

in ΔR found in the eastern Indian Ocean, the relations between the hydrography of these sample sites and the RR0705 core sites (RR0705 core sites are located in places that are less likely to undergo upwelling-induced inflated ΔR values), and the relative stability of ΔR for the past 3000 yr, we consider a maximum possible ΔR of ~90. This ΔR is small when compared to the absolute ages that we use as a chronological framework for our stratigraphic correlations. While constraints are few for this correction and do not extend far into the past, we are correlating marine sites to other nearby marine sites, thus the local correlations are likely similar for each time range, even as the variability from an absolute scale is unknown (absolute ages will contain additional uncertainty).

We used a sedimentation rate–based age model that allows estimation of turbidite emplacement ages, accounting for gaps between the sample and turbidite base. We propagated all uncertainties using root mean square (RMS) calculations using estimates of the uncertainties at each step. This calculation included the laboratory uncertainties and resulted in the final reported 95.4% error range for each radiocarbon age (see OxCal code Supplemental File S2). We use a moving average hemipelagic sedimentation rate (see Supplemental File S2 for a more detailed description). This calculation includes the laboratory uncertainties and yields the final reported 95.4% error range for each radiocarbon age. No laboratory multipliers were applied to these data because laboratories now include this uncertainty in their results that was previously accounted for by the laboratory multiplier (Scott, 2003; Goldfinger et al., 2012a).

Age Models

We constructed a series of OxCal age models to incorporate stratigraphic information into the age calibrations. OxCal uses Bayesian statistics to incorporate prior information (e.g., stratigraphic or age progressive information) into the age calibrations (Bayes and Price, 1763; Bronk Ramsey, 2008). OxCal age models are constructed with two components: the model structure (priors) and the age measurements (likelihoods). Because age depositional models often have many independent parameters, OxCal uses Markov Chain Monte Carlo (MCMC) simulations to sample age distributions and generate a final distribution (Bronk Ramsey, 2009a). We also build our OxCal age models with nested functions, such as the Combine function (discussed in the following).

For our OxCal age models, we use two depositional models: Sequence and P_Sequence (Bronk Ramsey, 2009a). The Sequence model considers the stratigraphic order (superposition) of the ages. The P_Sequence model considers the stratigraphic order and the relative stratigraphic depth. We use the P_Sequence model for age calibrations within cores because we can make estimates of stratigraphic depth within a core. Because the relative depths are different between cores (due to differences in hemipelagic sedimentation rates, lack of erosion correction, and sampling errors), we cannot use P_Sequence, so we use a Sequence model.

For the P_Sequence model, we constrain the depth by using the hemipelagic depth for the samples (Bronk Ramsey, 2009a). Because turbidites represent instantaneous changes in sedimentation rate, they do not reflect the long-term sedimentation rate between turbidite emplacements. For this reason, we remove the depth associated with the turbidite thicknesses from the sample depth information. We also use the OxCal Date function to generate synthetic ages for the bases of turbidites that have no direct radiocarbon age sample (Bronk Ramsey, 2001). We apply a ±0.5 cm sampling error to the depth term in the age model.

For our Sequence age model (Bronk Ramsey, 2009a), we use ages from all slope cores in the region of the 2004 SASZ earthquake. There are three ways in which we estimate the age of the correlated turbidites: single ages, combined ages, and synthetic ages. Some correlated turbidites have only a single radiocarbon age determination and this is the age we include in our model. For correlated turbidites that have multiple ages, we use the OxCal Combine function (Bronk Ramsey, 2001). We use our stratigraphic correlations to determine which laboratory ages to consider for all age Combines. The Combine function takes the laboratory age Gaussian distributions and combines these distributions. OxCal performs tests to evaluate how well the combined ages fit their combined age distributions. We discuss ways in which we discriminate ages that do not pass these tests of best fit. The results of these tests are included in the log file (Supplemental File S2). As with the P_Sequence model, for turbidites that do not have radiocarbon age determinations, we generate synthetic ages with the OxCal Date command.

We also provide temporal limits to the posterior age distributions with the OxCal Boundary function (Bronk Ramsey, 2008, 2009a), a "prior." OxCal boundaries exert a temporal limitation to the output probability density functions of the calibrated ages by limiting the age range of the probability density functions. We place a Boundary at the beginning of the model (oldest) so that the modeled age determination for the earliest age does not significantly extend into the past. We place a Boundary at the end of the model (youngest) because the sediment cannot be younger than A.D. 2007, the year the sediment was collected. We use these Boundary functions in the P_Sequence and Sequence age models.

The Combine function calculates a chi-squared test to determine if the sampled ages represent the same age population. For each Combine, a T value is given and a threshold value is given. If the T value rises above the threshold value, the Combine fails the chi-squared test. The Combine function also calculates agreement indices, as described here. While this is simply an analytical test that ignores geologic variability, it remains a useful filter in the absence of other prior information.

The P_Sequence and Sequence analyses, as well as Combine functions, use MCMC simulations to determine the degree to which the prior model agrees with the observations (in terms of likelihoods) with the agreement indices, A, A_{comb}, A_{model}, and $A_{overall}$; A identifies which samples do not agree with the model; A_{comb} tests whether the distributions can be combined. A_{model} tests to see if the model can be used given the ages used in the model. $A_{overall}$ is a product of the other agreement indices. In order to pass, OxCal agreement indices should be >60% (Bronk Ramsey, 2008); this represents the area of overlap of the probability density functions (PDFs). We adopt these criteria in our age models.

Geosphere, published online on 12 November 2015 as doi:10.1130/GES01066.1

When OxCal age Combines fail the chi-squared and agreement index tests, we remove outliers manually as an iterative process (Bronk Ramsey, 2009b). We first include all ages for potentially correlated strata. When tests fail, we examine the geologic context and manually remove the most probable outlier to examine whether failure was due to the outlier, or lack of good fit among the tested group (Bronk Ramsey, 1995, 2009b). We begin with the ages that have the lowest agreement index or are clearly older outliers.

Lithostratigraphic Correlation

We use integrated stratigraphic correlation techniques, including visual lithostratigraphic description (color, texture, and structure), CT image analysis, and lithostratigraphic log correlation of multisensor core logging (MSCL) geophysical data (Fukuma, 1998; Karlin et al., 2004; Abdeldayem et al., 2004; St-Onge et al., 2004; Hagstrum et al., 2004; Waldmann et al., 2011) to correlate turbidites based on the turbidite architecture (Amy and Talling, 2006). Stratigraphic correlation using geophysical signatures representing vertical turbidite structure is a primary tool for testing individual deposits for their areal extent, a significant part of the criteria used to discriminate seismoturbidites from other possible types. A positive correlation, regardless of the originating details, is indicative of a cogenetic origin. Downcore geophysical properties for individual turbidites are reflections of the vertical grain-size distribution of the bed (Kneller and McCaffrey, 2003; Amy et al., 2005; Karlin and Seitz, 2007; Goldfinger et al., 2012a). Lithostratigraphic correlation techniques have been used to correlate stratigraphic units since the 1960s (Prell et al., 1986; Lovlie and Van Veen, 1995). In detail these fingerprints represent the time history of deposition of the turbidite and, in several cases linked to plate boundary earthquakes, have been shown to correlate between independent sites separated by large distances and depositional settings (Goldfinger et al., 2008, 2013b). The turbidite is commonly composed of single or multiple coarse fraction fining-upward stacked units termed pulses. The rarity of a fine tail (Bouma Td and Te units; Bouma, 1962) or subsequent hemipelagic sediment between pulses indicates that there is commonly little or no temporal separation between units. The lack of temporal separation of the pulses in Cascadia has been inferred to represent deposition over minutes to hours, so most likely represent subunits of a single turbidite (Goldfinger et al., 2012a). We combine all these correlation tools when possible. The more tools that can be applied to an individual prospective correlation, the more robust the interpretation will be.

The most sensitive criteria for correlating fine-grained turbidites (which may not be visible to the naked eye) is the density profile (Inouchi et al., 1996), which we augment with very high-resolution CT density profiles and three-dimensional CT imagery. In the RR0705 cores, density and MS tend to covary with particle size; larger particles and magnetic minerals are generally denser (Thompson and Morton, 1979). An exception to this is tephra; while tephras have larger MS values, they are not denser than the overlying or underlying hemipelagites. The other MSCL data (P-wave velocity) were less effective because the sensors do not make sufficient contact with the core liner, so there are large gaps and excursions in the data. Resistivity shows a longer wavelength response to the sedimentary structure than the other geophysical data, so much so that we do not use this proxy (Fig. 2).

We verified the efficacy of the geophysical data as a grain-size proxy for the Sumatra lithologies with particle size analysis (cores 96 and 55; Fig. 2). In our figures, core geophysical data are plotted versus depth from left to right (gamma density, CT density, point MS [PMS], MS). Core particle size data are plotted versus depth from left to right (mean, median, mode, and d10, the particle size for which 90% of the particles are larger). For these cores exclusively, we plot resistivity (RES, in ohms) versus depth. Local maxima in particle size data match with local maxima in the geophysical data.

We distinguish between multipulse turbidites and a series of closely spaced single pulse turbidites with some sedimentologic and geophysical criteria. When there is hemipelagic sediment between coarse pulses (lack of fine laminations, presence of oxidation), those pulses are from turbidites that were deposited at different times, time separated as evidenced by the hemipelagic sediment or oxidation. In some cases it is difficult to distinguish between single-pulse and multipulse turbidites in this way, so we use the core geophysical data. We use the same criteria developed in Goldfinger et al. (2012a), by which background sedimentation typically has a lower geophysical (CT and gamma density; MS) value and the turbidites have higher values, verified by direct observation, color change, lithic smear slides, and micropaleontology. Turbidites that have coarser bases and fine upward have geophysical data that have larger values at the base and lessen upsection until the values reach that of the background hemipelagic sedimentation. When there are multiple coarse pulses, there are geophysical maxima for each coarse pulse that plot above the background geophysical values. A good example is T-20 in core 104PC. The CT and true color (red-green-blue, RGB) imagery shows four main coarse pulses and two finer pulses in the tail. The CT density plot also shows these four main and two minor pulses; each of the pulses coarsen upward. The PMS data show how these pulses progressively decrease in magnitude toward a background value and are the main evidence that T-20 is a multipulse turbidite in core 104PC. In core 103PC, T-20 does not have the detailed structure that is found in core 104PC, so we rely on the structure in core 104PC in this case.

We distinguish between individual single-pulse or individual multiple-pulse turbidites from a series of stacked single-pulse or multiple-pulse turbidites using sedimentologic characteristics. We consider characteristics of deposits within a single core, as well as these characteristics from adjacent cores where they are likely correlated. Local variability is inherent in these and all geologic records, thus the determination of single versus multipulse turbidites may not be apparent in all examples, but is taken from the best example of each bed in a correlated series. A detailed example of this was given in Goldfinger et al. (2012a). All correlated turbidites therefore inherit the classification from the best example of turbidite beds that are correlated along strike. We list the characteristics used to constrain turbidite deposition timing and sedimentation characters, and classify turbidites into three categories based on the following criteria.

Geosphere, published online on 12 November 2015 as doi:10.1130/GES01066.1

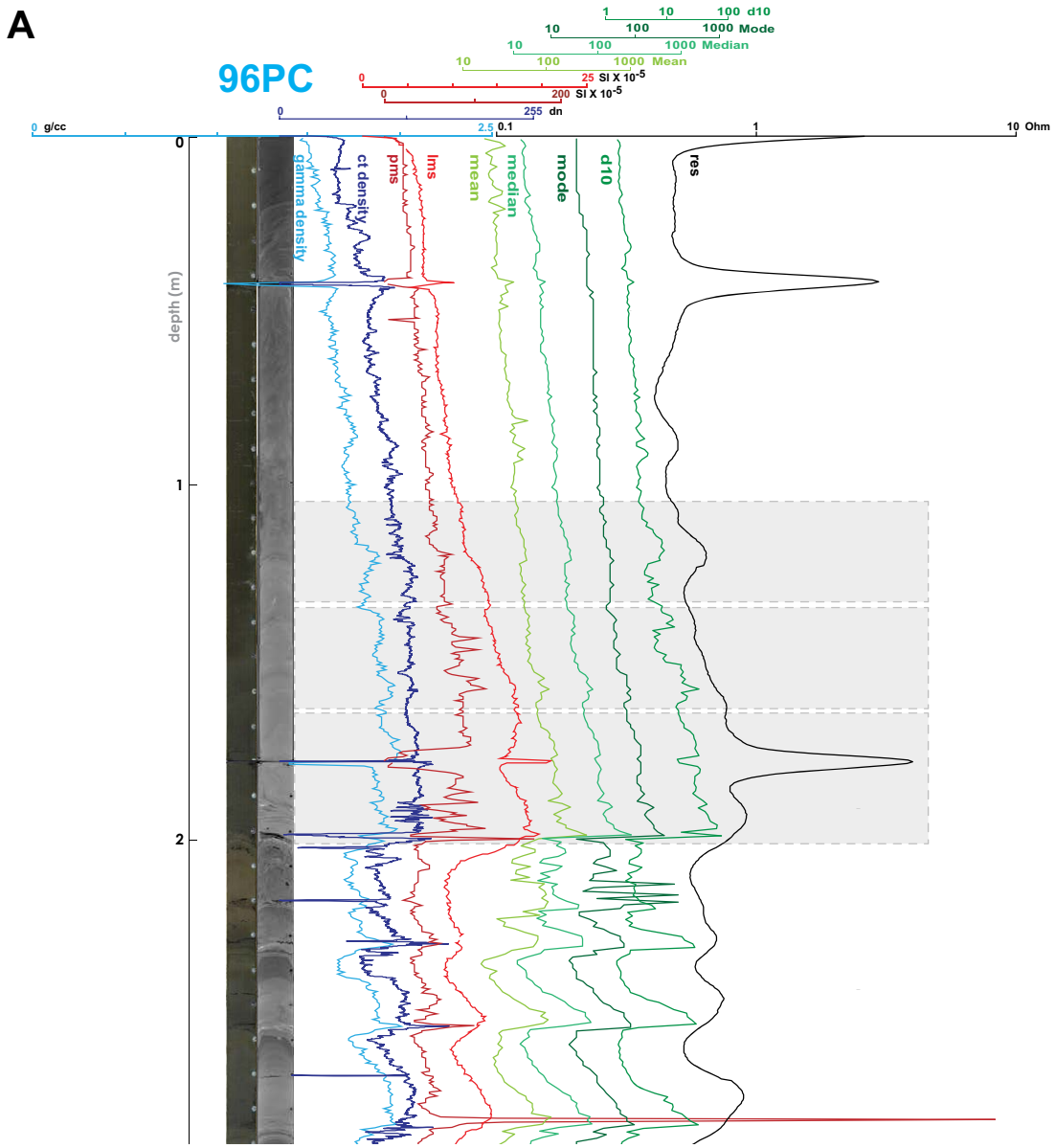

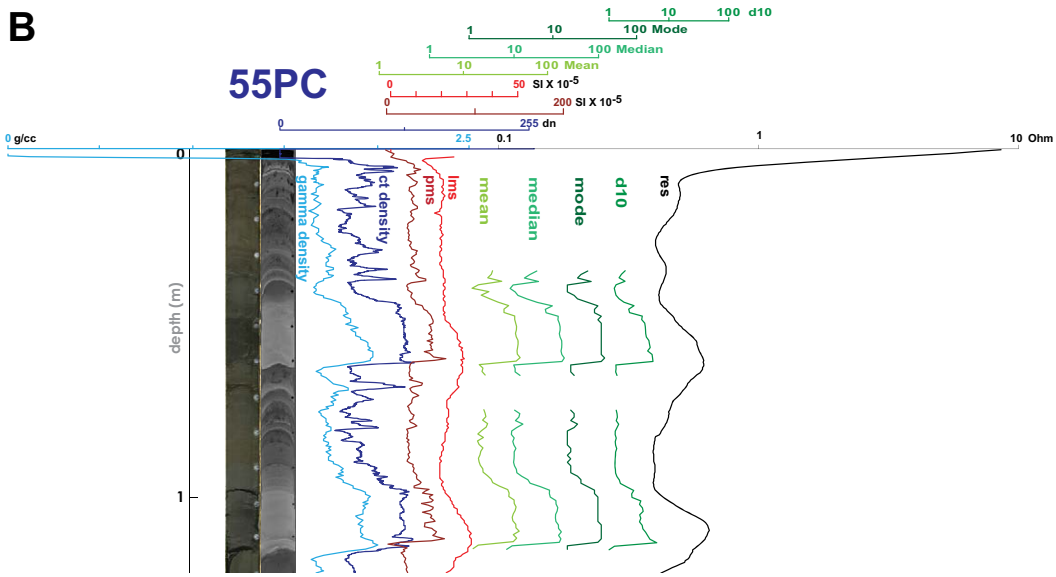

Figure 2. Core geophysical data are compared with particle size data. Plots are RGB (red-green-blue) imagery, CT (ct, computed tomographic X-ray) imagery, gamma density (g/cm^3, light blue), CT density (dn, image digital number, 0–255, dark blue), point magnetic susceptibility (pms, Si × 10^{-5}, dark red), loop point magnetic susceptibility (lms, Si × 10^{-5}, light red), mean, median, mode, and d10 particle size (μm, green; 90% of particles are larger than this size) on a logarithmic scale, and resistivity (Ohm, brown). (A) Core 96PC. (B) Core 55PC. Gray rectangles denote the three major peaks in the core geophysical data.

Geosphere, published online on 12 November 2015 as doi:10.1130/GES01066.1

Turbidite Classification Criteria

1. Impulsive base (IB): coarser sediment overlying finer sediment with a sharp (<1 mm) lithologic contact with fine-grained underlying sediment.

2. Erosive base (EB): evidence for an unconformity at the base of the turbidite, due to erosion during turbidite emplacement; may be evident as an angular and/or irregular base.

3. Underlying hemipelagic sediment (UHS-RGB): hemipelagic sediment is lighter in color than turbiditic sediment; this can be seen visually and in the RGB imagery.

4. Underlying hemipelagic sediment (UHS-CT): hemipelagic sediment is massive (lacks laminae) and low in density; this can be seen visually in the CT imagery.

5. Underlying brown oxidation laminae (UBOL): oxidation of sediment at the seafloor is not instantaneous and represents a time period much longer than the time required for the deposition of a turbidite. If there is oxidation between two turbidite beds, they are possibly (but not necessarily) the result of separate turbidity currents. Such contacts must be distinguished from oxidation fronts which move through the core with time.

6. Geophysical property relation (GPR): at least one of the core geophysical properties match the typical vertical profile of a typical turbidite-hemipelagite pair. The profile of a typical turbidite shows at least one maximum associated with a density or particle size increase at the base of the turbidite, with an upward decrease in value associated with the turbidite tail, and a further diminishing value to a background value associated with the hemipelagite.

7. Sediment Loading Structures (SLS): Evidence for sediment loading structures.

We define three classes, or categories, of turbidite beds based on these criteria: (1) more certainly a single-pulse or a multipulse turbidite; (2) less certainly a single-pulse or a multipulse turbidite; (3) indeterminately a single-pulse or multipulse turbidite (or possibly not a turbidite).

Category 1 includes turbidites that satisfy four of the seven criteria we list. Based on these multiple criteria, we find that there is a highest likelihood of the bed being a single turbidite. If three of the seven criteria we list below are met, then we are less certain with our interpretation and place the turbidite into category 2. If fewer than two criteria are met, we place the sedimentary deposit into category 3. Our preferred correlations are composed of category 1 and category 2 turbidites, but not category 3 turbidites. Some beds may be included in category 3 if they are incomplete, particularly at the base.

We make extensive use of industry techniques known as flattening and ghost tracing to examine turbidite sequences for correlation or lack thereof. Flattening core data to particular stratigraphic horizons (Major et al., 1998) is a test of the hypothesis that the stratigraphic sequences in the cores correlate and represent the same sedimentary history. This hypothesis can be tested with unlimited combinations of cores and requires only the assumption that the turbidite deposition consumes zero time. In practice, this is accomplished by the use of ghost geophysical traces from different cores that are iteratively compared to search for the presence or absence of a similar stratigraphic sequence. If correlations are found that satisfy the radiocarbon temporal constraints, a proposed sequence is then flattened, that is all of the geophysical and image data in the core diagram are hung on proposed uniform time horizons, represented by the bases and tops of each turbidite. The proposed correlation lines are then horizontal, or flat. This is accomplished by changing the vertical scale of each core to match a reference core. The thicknesses of the turbidites naturally vary between cores at a single site and between cores from different sites for a variety of reasons. Because turbiditic and hemipelagic sedimentation rates vary for cores at different sites, the thicknesses of stratigraphic units also vary for those core sites. It is this variability in stratigraphic thickness that is removed when several core sequences are flattened, scaling the core data to match these variations in thickness and sedimentation rate and placing the cores on a time basis in the vertical axis (Tearpock and Bischke, 2002) This allows the interpreter to see the stratigraphy as if there were a simple pancake stratigraphy with the first-order depositional variability largely removed and the characteristics if each bed emphasized.

Application to Sumatra

We review the rationale developed for the attribution of seismogenic triggering of turbidity currents in Cascadia and elsewhere modified here in our investigation of the stratigraphy offshore of Sumatra.

Distinguishing seismoturbidites from turbidites triggered by other mechanisms can be very difficult, and in some cases impossible. Two approaches can be applied, separately or in concert, to make this distinction: (1) sedimentology of the deposits, and (2) correlation of deposits to establish regional synchronous deposition unlikely to be caused by processes other than earthquakes. The principle basis for attributing a seismogenic trigger to a regionally extensive synchronously deposited bed is that regional and synchronous deposition is unlikely to have been generated by a trigger other than an earthquake (Goldfinger et al., 2007, 2008, 2012a; Patton et al., 2013a).

Radiocarbon is used to establish the chronostratigraphic framework; however, radiocarbon ages cannot be used to establish synchronous deposition because the uncertainties generally preclude this; they can be used to establish consistency, but not synchroneity. However, synchroneity need not mean establishing the exact timing of events at multiple sites; the requirement is to test whether or not the deposits were laid down at the same time. To do this, we use relative age tests, lithostratigraphic correlation methods, and comparisons of turbidite bed sequences at isolated sites to assess whether turbidites are likely the same turbidite, or sequence of turbidites, deposited at the same time, individually or in sequences. Note that this does not require a physical connection between turbidites at isolated sites, which may or may not exist. Such turbidites may be deposited synchronously at isolated sites by a common trigger, without a physical connection.

Geosphere, published online on 12 November 2015 as doi:10.1130/GES01066.1

Relative Age Tests

One way to examine turbidite sequences for synchronous deposition includes the confluence test, and Cascadia turbidites pass this test (Adams, 1990; Goldfinger et al., 2003, 2007, 2008, 2012a). This test poses that if the channel system has the same number of turbidites above and below a confluence, the deposits in all locations were laid in the same short period of time lasting minutes to hours (Goldfinger et al., 2012a). Because of this similarity in stratigraphy between cores in this example, the researchers conclude that the trigger for these turbidity currents likely affected a broad region (thousands of square kilometers). This test was applied to Cascadia (Goldfinger et al., 2012a), the northern San Andreas (Goldfinger et al., 2007, 2008), Japan (Nakajima and Kanai, 2000), and Chilean lakes (VanDaele et al., 2014). Similarity of sequences can also be compared between isolated basin sites that, like the confluence test, should not have very similar sequences if the triggering mechanisms are neither regional nor synchronous.

Isolated Sites and Synchronous Deposition

Well-log correlations between sites in Cascadia have been used to test links between sites. In support of findings, Goldfinger et al. (2003, 2008, 2012a) correlated turbidites in cores that sample unique source areas (Cascadia Seachannel with Juan de Fuca Canyon and Hydrate Ridge Basin West with Rogue canyon 250 km southward along strike), a correlation test independent of the confluence test that further supports the areal extent of the trigger for these turbidites.

Controls on the Physical Structure of Turbidites and Log Correlation

The detailed depositional structure of turbidites is likely a combination of several turbidity current forcing factors. Because turbidite deposition is a sedimentary result of the passing turbidity current, the forcing factors probably also control the structure of the turbidite. Factors that promote allocyclic forcing (i.e., sedimentation and erosion controlled by the source or input of sediment flux; Underwood et al., 2005) can include the source of the initial landslide, such as whether the turbidity current is from hyperpycnal flow or a seismogenically triggered landslide (Seilacher, 1969; Shiki et al., 2000; Mulder et al., 2003; Goldfinger and Morey, 2004; Garrett et al., 2011; Goldfinger et al., 2012a, 2012b). Factors that promote autocyclic forcing (i.e., sedimentation and erosion controlled by local or site processes) include flow dynamics, site geomorphology, and proximity (Middleton, 1967; Nelson et al., 1986; Muck and Underwood, 1990; Kneller and McCaffrey, 1995; Kneller and Buckee, 2000; Baas et al., 2004, 2005; Amy et al., 2005; Amy and Talling, 2006; Dennielou et al., 2006; Felix and Peakall, 2006). These forcing factors may compete depending upon core location, local physiography, and distance to the source region of the turbidity current. If trigger source forcing dominates over a sufficiently large region, turbidites deposited by those turbidity currents that share this common forcing may also share a common turbidite structure. As a result, these turbidites may also share a common fingerprint. Although we may not yet know precisely why correlation is effective in detail, if a strong correlation can be established, it can be used to link deposits, or to show lack of evidence for links.

As in prior work done in Cascadia (Goldfinger et al., 2012a), we use lithostratigraphic correlation of geophysical logs as discussed herein to test for potential links between basin sites with radiocarbon support, between basins and the trench (with radiocarbon in the basin only), and between trench sites that lack radiocarbon support. In addition to individual turbidite correlation, we consider sequences of turbidites, supported by turbidite mass, ages, number of coarse pulses, geophysical log signatures, and the number of turbidites above or between external chronostratigraphic datums (e.g., the Mazama ash or a Pleistocene-Holocene faunal boundary; Griggs and Kulm, 1970). Turbidite sequences may comprise a unique series of turbidites identifiable using any or all of these features. The linking of a turbidite series, as with individual turbidite correlations, was used in Goldfinger et al. (2012a) to correlate turbidites along strike; that correlation information was used to estimate the rupture length of the causative earthquakes. CHIRP subbottom profiles are used at this stage to assist in comparison of stratigraphic sequences. These subbottom profiles provide us with the ability to look deeper in the sedimentary section than is reachable by our cores. The 20–25 cm resolution of these profiles (verified with the core data) is capable of imaging many of the larger turbidite beds, to establish consistency of stratigraphy within a depocenter, and for intersite comparison.

Because of the difference in basin and site effects and turbidite channel architecture between Sumatra and Cascadia (Patton et al., 2013a), the tests for seismogenic triggering are slightly different. As in Cascadia, we base our correlations largely on three factors: (1) sedimentary source isolation, (2) deposit geophysical property fingerprint, and (3) timing or age control. Sumatra cores in slope basins are isolated from each other and most of them are completely isolated from terrestrial or shallow-water sediment sources, so links between them are used as a primary way to test for regionality of triggers. Most alternate triggers, such as hyperpycnal flow and wave loads, fail this simple test because these mechanisms do not affect regions of thousands of square kilometers or hundreds of kilometers along strike.

Turbidites and turbidite sequences are compared between sites using the criteria here. Turbidites and turbidite sequences that satisfy all or most of the criteria herein are considered correlated to varying degrees as indicated by the line symbol on the plots. If turbidites can be correlated between cores across a sufficient distance with high confidence, we assign a T-number to that correlation. There are additional turbidites in our cores that fail these tests to a degree that they are not considered correlated.

RESULTS

Slope sites used in this study include cores 109, 108, 104, 103, 102, 97, 96, 95, and 90, all of which have isolated sediment sources. In the trench, cores 03, 05, 107, 105, 99, 98, 94, 93, and 88 receive sediment from both upstream

Geosphere, published online on 12 November 2015 as doi:10.1130/GES01066.1

(up trench) in the trench and from downslope transport from the continental slope (Patton et al., 2013a). Figure 3 shows the possible source areas and flow relations for the cores that we primarily use for our correlations (all regional cores are shown in Supplemental File S3[3]).

We placed core sites in both trench locations and continental slope basin locations. Core locations are given in Table 1 and shown in Figures 1 and 3 and Supplemental File S1. The light gray (in CT imagery) sand bases of turbidites are easily identified and MSCL maxima in gamma density and MS correlate well with the CT density maxima (Fig. 3H). We note that the spatial resolution of the various geophysical traces varies with the thickness, volume, density, and magnetic content of the turbidites (see discussion of methods). The high-resolution CT data represent finer detail than do the gamma density and magnetic data. While all data are registered on the same vertical scale, there are some vertical differences in the apparent position of features in the cores stemming from geophysical edge effect, in addition to small changes in the cores over the several years of data collection.

The lithostratigraphy in the northern Sumatra slope and trench cores is dominated by turbidites interbedded with massive hemipelagic mud and less common tephras. Bioturbation is common and core-induced deformation is observed in some cores. Turbidites are composed of coarse silt to coarse sand bases, occasional ripup clasts, and fining-upward sand and silt to clay subunits; slope cores have abundant forams. The coarse fraction is composed of mica and quartz grains with rare mafics, consistent with a Himalaya source from the accreting Bengal and Nicobar fans (Stow et al., 1990). Basal turbidite subunits are composed of primarily foraminiferal hash in some piggyback basin cores. Sand subunits commonly range in thickness from 0.5 to ~20 cm, are parallel laminated and cross-laminated, and commonly underlie massive sand beds. Finer material is composed of silt- to clay-sized particles (Fig. 2). Primary tephras 0.5–10.5 cm thick are rare and can be correlated between sites using electron microprobe and laser ablation inductively coupled plasma mass spectroscopy data (Salisbury et al., 2010, 2012). Turbidite stratigraphy with these general characteristics is found in all slope basins (cores 108, 104, 103, and 96) and trench sites (cores 107, 105, 98, and 94), spanning 230 km along strike.

We describe the turbidite structure in the RR0705 cores using Bouma (1962), van der Lingen (1969), Stow (1977), and Piper (1978) fine-grained classification system divisions, and label the sedimentary layers according to these systems (Stow, 1985; Fig. 4A). A complete Bouma sequence (Bouma, 1962) would comprise superposed divisions Ta, Tb, Tc, Td, Te, and F. Stow and Piper (1984) divisions fit within the Bouma division Te, in superposed order, E1, E2, E3 or T0, T1, T2, T3, T4, T5, T6, T7, and T8. The complete sequence, for either division scheme, is not typically found in most turbidites.

We show typical turbidites, some multipulse, from cores 96PC and 108PC in Figure 4B. Multipulse turbidites may have superposed and repeated divisions (e.g., core 108PC, 312–294 cm: Tc-d, Td, Tc, T3, T6, T7) or just superposed divisions (e.g., core 108PC, 291–280 cm: Td, T3, T4, T7). All multipulse turbidites have multiple maxima in the geophysical data (commonly reflecting grain-size variations) that correspond to the structural divisions.

We analyzed 46 radiocarbon ages and 37 ^{210}Pb samples for the cores within the 2004 SASZ earthquake region. Table 2 lists the ^{14}C ages used in our OxCal age models and includes the laboratory age (in radiocarbon years), calibrated age (calendar yr before present, or A.D. 1950, i.e., cal yr B.P.), and the moving average hemipelagic sedimentation rate for that sample. The sample name is a compilation of the cruise name, the core number and type, the sample interval (in centimeters), and the sample number. We use the sample name in OxCal to track core and stratigraphic information through the age modeling. Calibrated ages are plotted in core figures and are used to establish the framework for lithostratigraphic correlation. We found no age inversions (where older ages superpose younger ages) in these age data that span the middle to late Holocene.

Surficial Turbidite in the 2004 Rupture Zone

The uppermost turbidite in 21 cores (01GC, 05PC, 26GC, 88TC, 87PC, 87TC, 93TC, 94PC, 95PC, 96PC, 96TC, 97MC, 99MC, 102MC, 104PC, 104TC, 105TC, 107PC, 108PC, 108TC, and 109MC); and second uppermost turbidite in two cores (93TC and 88TC) share common characteristics suggesting recent deposition based on the lithostratigraphic descriptions, radiometric age estimates, and relative age evaluations (GC, gravity core; PC, piston core; TC, trigger core; MC, multicore; Supplemental Files S1, Se). Five cores do not appear to contain the complete uppermost deposit and just have the base of what may be the 2004 deposit (01, 26, 104, 107, and 108). It is not possible to evaluate the completeness of the section in six cores due to coring deformation (05, 88, 93, 94, and 109). One core set has a complete deposit when adjacent cores 96PC, 96TC, and 97MC are composited. Two additional cores may have the entire deposit (93TC and 88TC; Supplemental File S3). Sediment in 96PC and 96TC is deformed and compressed in places, so it is difficult to assess the true thickness of the turbidite in these cores. Core 102MC may also have the entire turbidite section, though in a thinner deposit (~6 cm thick; Supplemental File S3).

We use core 96 for our discussion of the sedimentologic characteristics because it is probably complete and has the most expanded section of young uppermost deposit, though many of these sedimentologic qualities (e.g., the unconsolidated soupy nature of the uppermost turbidite) are shared in all 21 cores. We scale the TC to the PC based on common stratigraphic contacts, resulting in an estimated thickness of 308 cm (Fig. 5). We could not determine if multicore 97MC included sediment missing from the top of 96TC, so we did not use this core in our composite estimate of sedimentary thickness. Core 96 is located in an enclosed basin (Fig. 6A) and has an extensive record of the uppermost turbidite as revealed by CHIRP seismic data collected in a cross-basin transect (Figs. 6A, 6B). In this core the uppermost turbidite is described as soupy and water laden (lithologic notes, 120 cm, 170 cm; Fig. 5A). The water content was so high that, during the shipboard lithologic description, care was required to prevent the sediment from pouring out of the core when placed horizontally. The reflectivity of the RGB image is consistent with these observations (the wet sediment is shiny, especially noticeable between 5 and 10 cm).

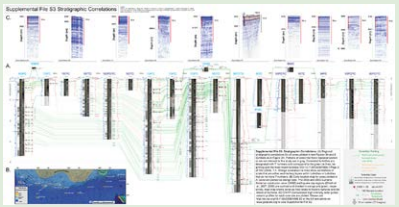

[3]Supplemental File S3. Stratigraphic correlations. (A) Regional stratigraphic correlations for all cores plotted in text Figures 3A and 8. Symbols as in Figure 3H. Portions of cores that have repeated section or are not relevant to this study are in gray. Correlated turbidites are designated with T numbers and correspond to the green tie lines, beginning with the most recent turbidite (2004), T-1. Orange correlation tie lines show correlations of strata that are either sedimentary layers within turbidites or turbidites that do not have T numbers. (B) Core location map for cores plotted in A; cores are plotted as orange dots. The 2004 and 2005 Sumatra-Andaman subduction zone (SASZ) earthquake slip regions (Chlieh et al., 2007, 2008) are outlined and shaded in orange and green, respectively. Inset map shows cores as they relate to historic ruptures and the Island of Sumatra. (C) CHIRP (compressed high-intensity radar pulse) seismic profiles for each core site are plotted. Please visit http://dx.doi.org/10.1130/GES01066.S3 or the full-text article on www.gsapubs.org to view Supplemental File S3.

Geosphere, published online on 12 November 2015 as doi:10.1130/GES01066.1

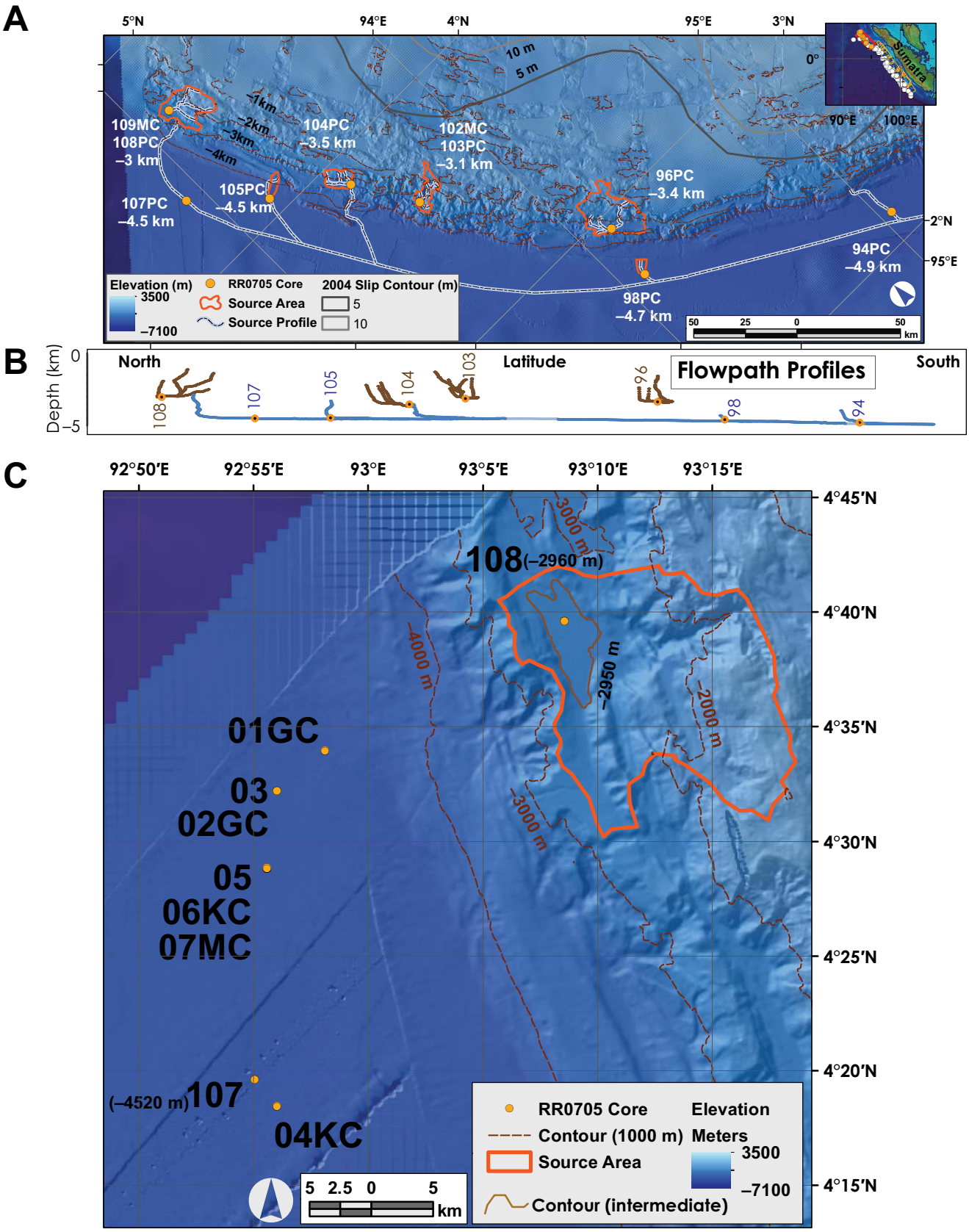

Figure 3 (*on this and following two pages*). Regional core sites, source areas, and key core stratigraphy. (A) Core locations (orange dots) on bathymetric map; key channel flow paths (light blue) to eight core sites are shown. Slope basin and trench source areas (orange) were determined by outlining drainage divides surrounding all submarine topography contributing potential gravity flows to a given core site. While the region that drains to core 104PC then drains to the trench, the three other slope basins are enclosed (they do not drain to the trench). (B) Flow path profile depth (km) versus forearc distance (degrees latitude) is plotted in brown for basin flow paths and blue for trench flow paths. (C) Shaded relief map showing core sites 108 and 107 as orange dots. Cores are labeled with their core number and the seawater depth at the core sites in meters. Depth contours are in meters. An intermediate contour of –2950 m depicts the shape of the low-relief basin floor where core 108 is located.

Geosphere, published online on 12 November 2015 as doi:10.1130/GES01066.1

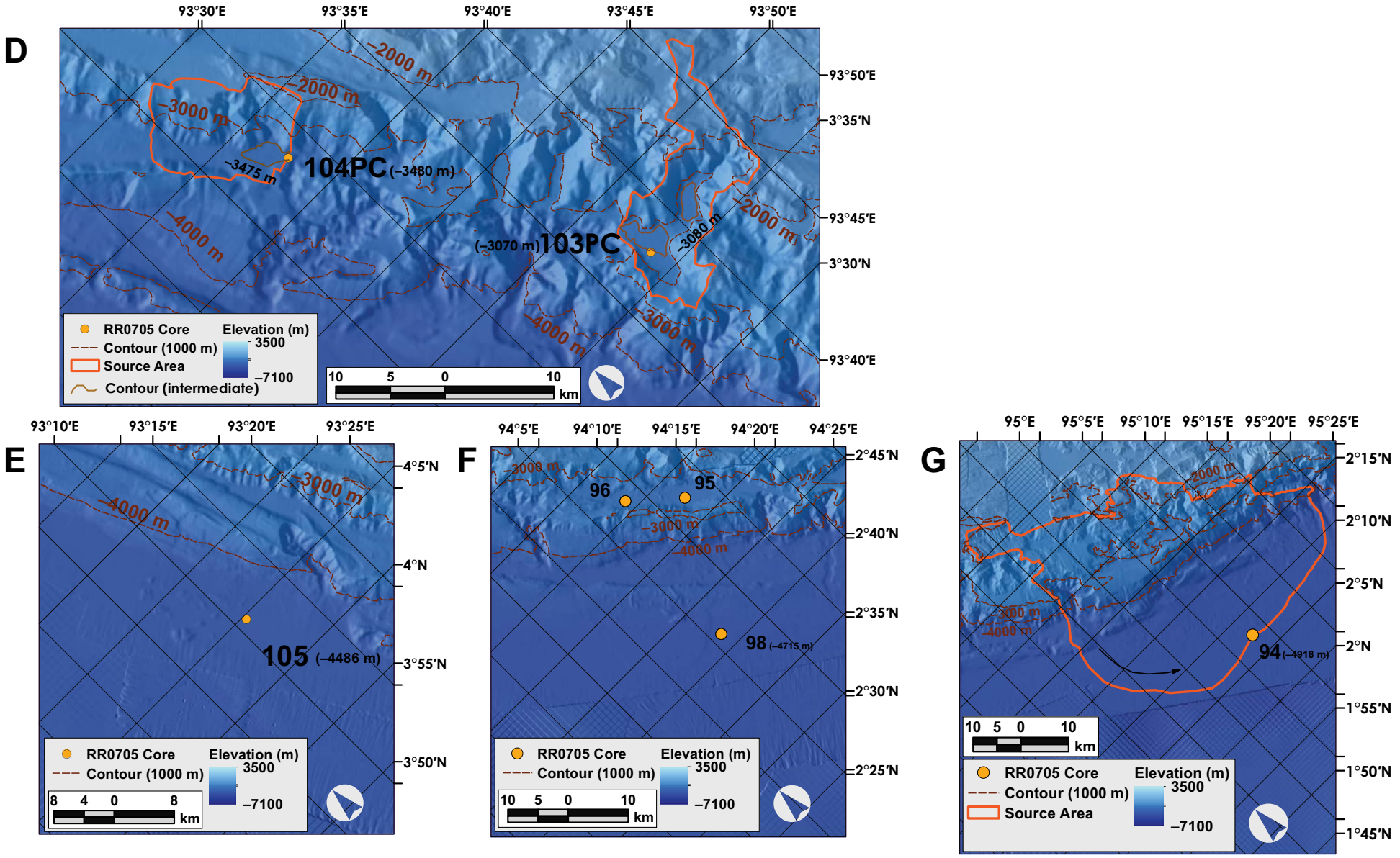

Figure 3 (*continued*). (D) Core sites 103 and 104 are plotted as orange dots, with the core depth in meters. Intermediate contours of –3475 m and –3080 m depict the shape of the basins. (E) Core site 105 is plotted with the core depth in meters. (F) Core site 98 is plotted with the core depth in meters. (G) Core site 94 is plotted with the core depth in meters.

Geosphere, published online on 12 November 2015 as doi:10.1130/GES01066.1

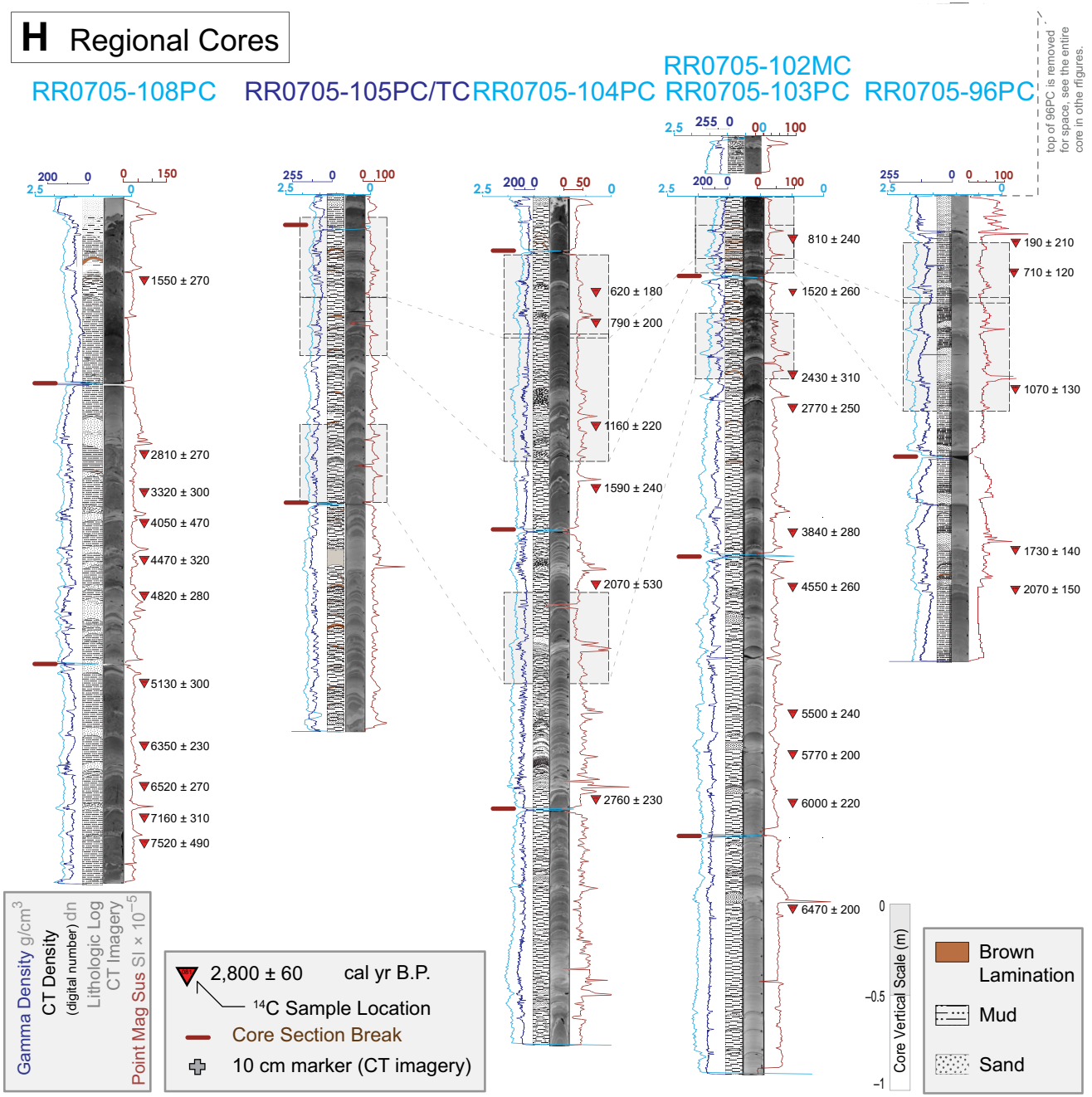

Figure 3 (*continued*). (H) Five principle cores that we use in our correlations and age models are plotted versus depth in cm. Multisensor core logging geophysical data are plotted [gamma density, CT (computed tomographic X-ray) density, point magnetic susceptibility (Mag Sus), from left to right] and CT imagery displays lower density material in darker gray and higher density material in lighter gray. Slope cores are labeled in light blue; trench cores are labeled in dark blue. ^{14}C ages are reported in calendar (cal) yr B.P. (A.D. 1950). Gray rectangles refer to Figure 8.

Geosphere, published online on 12 November 2015 as doi:10.1130/GES01066.1

TABLE 1. CORE LOCATION COORDINATES AND CORE INFORMATION

Core	Lat (°N)	Long (°E)	Water depth (m)	Core length (m)
RR0705-03TC	4.5365	92.9339	4483	1.91
RR0705-03PC	4.5365	92.9339	4483	2.73
RR0705-05TC	4.4804	92.9267	4498	0.91
RR0705-05PC	4.4804	92.9267	4498	3.08
RR0705-16GC	3.2866	94.0353	1911	1.95
RR0705-18GC	3.2761	94.0198	1820	3.14
RR0705-55PC	–4.5197 °S	100.2131	6046	2.61
RR0705-88TC	1.3115	96.2635	5197	0.91
RR0705-88PC	1.3115	96.2635	5197	4.71
RR0705-90MC	1.52	96.3793	3836	0.14
RR0705-93TC	1.7209	95.8124	5040	1.20
RR0705-93PC	1.7209	95.8124	5040	4.92
RR0705-94PC	2.1242	95.051	4918	3.81
RR0705-95PC	2.8745	94.2061	3418	2.23
RR0705-96TC	2.9336	94.139	3410	1.33
RR0705-96PC	2.9336	94.139	3410	4.40
RR0705-97MC	2.9336	94.139	3412	0.68
RR0705-98TC	2.6921	9.1	3410	1.22
RR0705-98PC	2.6921	94.1	3410	4.77
RR0705-102MC	3.6051	93.6315	3073	0.22
RR0705-103TC	3.6051	93.6315	3073	1.63
RR0705-103PC	3.6051	93.6315	3073	4.74
RR0705-104TC	3.8716	93.4747	3476	1.92
RR0705-104PC	3.8716	93.4747	3476	4.58
RR0705-105TC	4.0787	93.181	4486	0.55
RR0705-105PC	4.0787	93.181	4486	2.75
RR0705-107TC	4.327	92.9177	4518	1.79
RR0705-107PC	4.327	92.9177	4518	0.81
RR0705-108TC	4.6598	93.1428	2959	1.28
RR0705-108PC	4.6598	93.1428	2959	3.70
RR0705-109MC	4.6598	93.1428	2959	0.06

The uppermost sedimentary deposit consists of a multipulse, upward-fining, quartz-mica, medium sand to silty clay turbidite. The turbidite has three main pulses, with additional smaller pulses, as evidenced in the particle size, CT density, gamma density, CT imagery, and sedimentary texture data (Fig. 5A). The three main pulses are resolvable in these seismic reflection data (brown dots; Fig. 6B).We classify the turbidite structures (Figs. 5A, 5B) with the same system as in Figure 4A. There is little to no bioturbation in the top of the deposit, possibly indicating minimal postdepositional time before collection (Fornes et al., 2001). There is no oxidation in the surficial sediment, which may also indicate relative postdepositional time. Oxidation of surficial sediments commonly takes months to a few years (Sayles et al., 1994; Martin and Sayles, 2003) and was not present at the time of collection, 2.5 yr after the 2004 earthquake. Foraminifera are absent in surficial sediment in this and other cores, indicating a probable lack of hemipelagic sediment at the surface. We see no evidence of hemipelagic material overlying the young deposit in cores 94, 96, 97, 99, 102, and 109, while cores 01, 05, 26, 88, 93, 95, 99, 104, 107, and 108 are likely missing their tops and offer no constraint on the presence of hemipelagic sediment at the surface (Supplemental File S3).

The base of the turbidite has some interesting characteristics that may reveal details about the nature of deposition (erosional versus depositional) and length of time of deposition (rapid or slow). The lowermost laminations include embedded mud clasts, possibly of the underlying sediment. The basal contact of the turbidite shows further evidence of the turbidite penetrating the underlying mud in scours or intrusions. The shape of the basal contact also suggests that the turbidite loaded the underlying mud (i.e., pushed downward, deforming the upper contact of the underlying mud).

It is remarkable that the CT density of the coarse section of the 102MC uppermost turbidite is quite similar to the geophysical data from core 96PC (Figs. 3 and 5). In the trench, downtrench and south of the 2004 earthquake slip zone, cores 88TC and 93TC contain turbidites that also appear to have similar structure (three upward-fining subunits, reflected by the geophysical proxies) to that found in core 96PC (Supplemental File S3).

We also use core 96PC to present an example of our turbidite classification system. We plot a portion of core 96PC that has turbidites of all three classes (Fig. 5E). The core data are shown as in the other cores. The class is designated by the relative percent gray of rectangles to the left of the core imagery data. For each turbidite, we list, by number, the criteria that are satisfied. We also outline and label the locations in the core where our observations support the criteria. These criteria are color coded. Turbidite classifications are shown for this and other cores in Supplemental File S3.

Age Constraints

Core 96PC and core 102MC were among the better candidates for age dating. We did not sample beneath the uppermost turbidite in cores 108 and 104 because the CT imagery shows evidence of erosion and stratigraphic (possibly coring) disturbance. Nevertheless, there remains a thin turbidite between the radiocarbon sample and the uppermost turbidite in core 96PC. Age determinations and calibrations for these two cores are given in Table 3. We report the laboratory age (radiocarbon facility reported age), the simple calibrated age (a gap correction age model), the Sequence age (age model for within the cores for 96PC and 102MC), and the P_Sequence model (a second age model for within the core for 96PC). Core 102MC is not a candidate for a P_Sequence model because there is only one age sample. Laboratory ages are reported to 2σ error and calibrated ages are reported to 95.4% error. The simple calibrated age is only constrained by the priors accounting for the correction for the thickness of the overlying hemipelagic sediment between the sample and the event base. The Sequence age is only slightly better constrained with the priors of stratigraphic order and the collection time as a boundary, so the boundary priors do not substantially affect the results. The age calibration that includes the most prior information is the P_Sequence age, including stratigraphic

Geosphere, published online on 12 November 2015 as doi:10.1130/GES01066.1

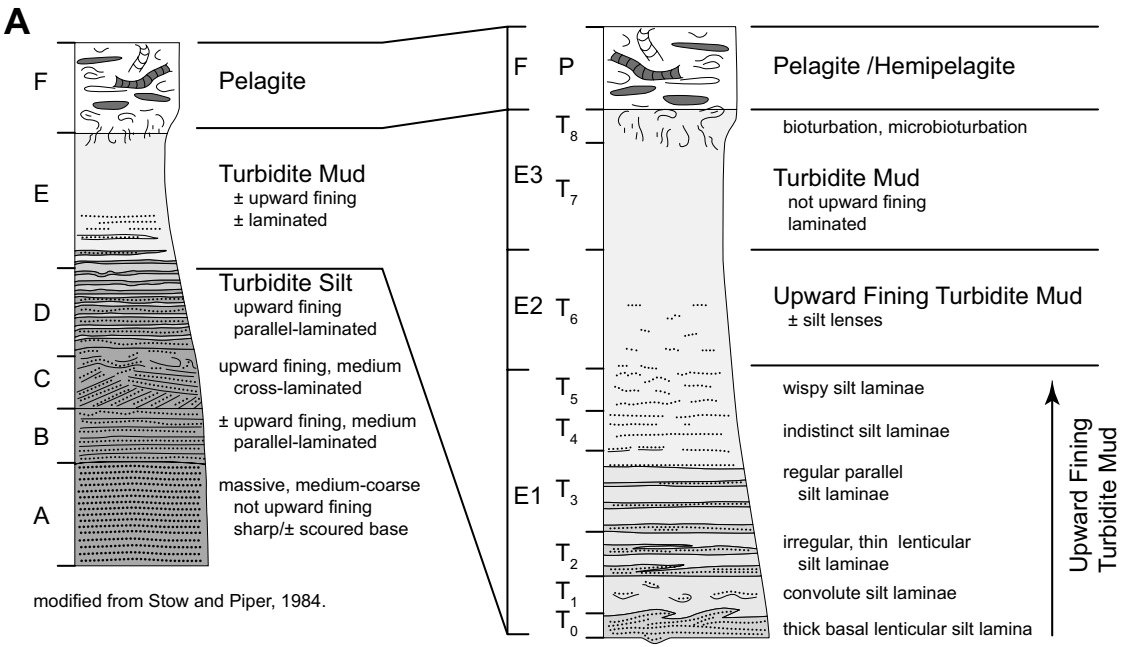

Figure 4 (*on this and following page*). Turbidite division classification. (A) Bouma (1962) and van der Lingen (1969) turbidite structure classification for fine grained turbidites is shown at left. Divisions are designated by letters A–F, typically designated with a preceding T. Stow (1977) and Piper (1978) turbidite structure classification system for fine-grained turbidites is shown at right. Piper (1978) divisions are designated by E and F. Stow (1977) divisions are designated with T-. Both Stow and Piper divisions fit within the Bouma Te division.

position and stratigraphic order. The stratigraphic position in the event-free (hemipelagic) sedimentary sequences adds a strong prior constraint and is responsible for the narrower uncertainties.

We do not prefer any single age model over another, but all their uncertainty ranges span recent decades, including the year 2004. The age ranges (relative to A.D. 1950) for these three models are: calibrated model age: –30 ± 60 (A.D. 1980 ± 60, core 96PC), Sequence model: 50 ± 160 (A.D. 1900 ± 160, core 96PC), and P_Sequence model: 60 ± 150 (A.D. 1890 ± 150, core 96PC). The model ages for core 102MC result in slightly older ages of 40 ± 40 for the simple calibrated, and 50 ± 60 for the Sequence model (Table 3). The 102MC age models include a gap correction, thus if the sedimentation rate is slightly underestimated, the age results would be older, and younger if overestimated.

We also used the exponential decay of ^{210}Pb activity with depth, and in the presence or absence of ^{137}Cs, indicative of deposition since 1952, to evaluate the timing of deposition for these uppermost sediments. Sediment from cores 94PC and 105PC were analyzed for ^{210}Pb and ^{137}Cs activity using gamma counting (see discussion of methods). Results are plotted in Table 4A and Figure 7. Sediments from cores 96PC, 96TC, and 102MC were analyzed for ^{210}Pb activity using the other gamma counting system (described in methods). Results are plotted in Table 4B and Figure 7. No ^{137}Cs activity was detected in core 94PC or core 105PC. The absence of ^{137}Cs can be interpreted as either decay below detection limits, implying a very young age, or simply that not enough material was initially present; the presence of ^{137}Cs in the Southern Hemisphere is reportedly patchy, so this is a distinct possibility (Alam et al., 1996).

Each of the five sampling sequences show evidence of excess ^{210}Pb activity underlying the uppermost turbidite in these cores, indicating deposition within at least the past 150 yr. The spacing of samples in 94PC and 105TC was chosen simply to test for the presence or absence of ^{137}Cs and ^{210}Pb. Both cores show evidence of recent deposition. We improved our sampling strategy for analyzing the age in 96PC, 96TC, and 102MC by sampling directly beneath the turbidites in depth-adjacent sample locations. Cores 96PC and 102MC show exponential decay, but 96TC does not, suggesting the lowermost sediment sampled in 96TC is very young and probably mixed.

We use hemipelagic sediment thickness from above and below, along with a ^{210}Pb derived sedimentation rate, to estimate the timing of deposition for the possible 2004 turbidite. Based upon the sedimentation rate calculation methods of Ghaleb (2009), we determine the sedimentation rates for 96PC and 102MC to be 0.015 cm/yr and 0.016 cm/yr respectively. There is no hemipelagic sediment overlying the youngest turbidite in either core, 96PC or 102MC. We cannot directly estimate the age of deposition for the possible 2004 turbidite with this method. The thickness of hemipelagic sediment beneath the possible 2004 turbidite and above the ^{14}C age sample is 0.5 mm and 0.5 mm for cores 96PC and 102MC respectively (Figure 7). The combination of the low sedimentation rate and the thickness of hemipelagic sediment provide ^{210}Pb derived ages that are, within error, not different than the ^{14}C age used for these calculations.

Geosphere, published online on 12 November 2015 as doi:10.1130/GES01066.1

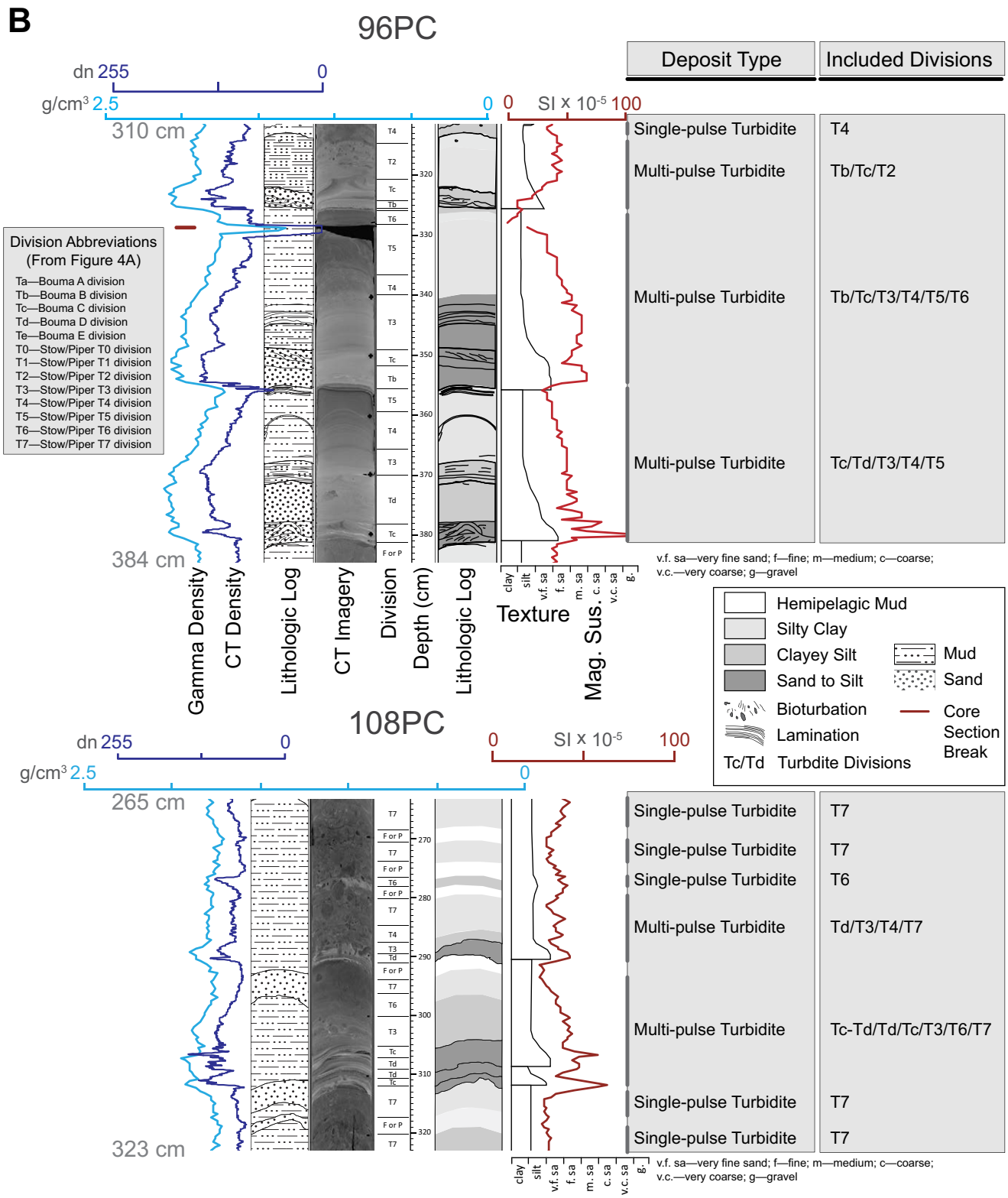

Figure 4 (*continued*). (B) Turbidites in cores 96PC and 108PC are plotted with turbidite division systems in displayed in A. Plotted from left to right are gamma density, ct (computed tomographic X-ray) density, lithologic log (pattern), CT imagery, turbidite division, core depth (cm), lithologic log (grayscale texture), texture (particle size phi scale including, from left to right, clay, silt, very fine sand, fine sand, medium sand, coarse sand, very coarse sand, and gravel), and point magnetic susceptibility (Mag. Sus.). The deposit type (single pulse or multipulse) and turbidite structure divisions present (included divisions) are listed for each turbidite.

Geosphere, published online on 12 November 2015 as doi:10.1130/GES01066.1

TABLE 2. RADIOCARBON AGE RESULTS FOR AGES ANALYZED IN THE 2004 SUMATRA-ANDAMAN SUBDUCTION ZONE EARTHQUAKE REGION

Sample number	Laboratory sample number*	Sample name	Core number	Depth (cm)	Laboratory age† (yr)	Laboratory age error	Calibrated age§ (yr)	Calibrated age error	Hemipelagic sedimentation rate (cm/k.y.)**	Sedimentation rate error
SUM-172	76995	RR0705_108TC_020_022_SUM-172	108TC	21	1930	20	1380	540	16	2
SUM-080	65294	RR0705_108PC_039_041_SUM-080	108PC	40	2020	20	1550	270	16	2
SUM-081	65295	RR0705_108PC_132.5_134.5_SUM-081	108PC	133.5	3040	20	2810	270	13	1
SUM-083	65296	RR0705_108PC_156_158_SUM-083	108PC	157	3500	20	3320	300	12	1
SUM-046	54321	RR0705_108PC_175_177_SUM-046	108PC	176	4070	20	4050	470	5	1
SUM-194	76996	RR0705_108PC_194_196_SUM-194	108PC	195	4340	20	4470	320	19	2
SUM-045	54320	RR0705_108PC_212.5_214.5_SUM-045	108PC	213.5	4630	20	4820	280	22	2
SUM-042	54303	RR0705_108PC_257_259_SUM-042	108PC	256	4840	20	5130	300	19	2
SUM-044	54305	RR0705_108PC_290.5_292.5_SUM-044	108PC	291.5	5950	20	6350	230	13	1
SUM-043	54304	RR0705_108PC_312.5_314.5_SUM-043	108PC	313.5	6120	20	6520	270	9	1
SUM-041	54302	RR0705_108PC_330_332_SUM-041	108PC	331	6690	30	7160	310	4	0
SUM-195	77247	RR0705_108PC_345_347_SUM-195	108PC	346	7180	20	7520	490	4	0
SUM-176	77107	RR0705_104TC_011_013_SUM-176	104TC	12	710	20	320	340	2.9	0
SUM-175	77106	RR0705_104TC_047.5_049.5_SUM-175	104TC	48.5	1220	20	770	360	2.9	0
SUM-060	65529	RR0705_104PC_049.5_051.5_SUM-060	104PC	50.5	1070	20	620	180	9	1
SUM-062	54325	RR0705_104PC_067.5_069.5_SUM-062	104PC	68.25	1270	20	790	200	10	1
SUM-061	65530	RR0705_104PC_122_124_SUM-061	104PC	123	1630	50	1160	220	10	1
SUM-082	65531	RR0705_104PC_158_160_SUM-082	104PC	159	2040	20	1590	240	10	1
SUM-115	65532	RR0705_104PC_207_209_SUM-115	104PC	208	2420	220	2070	530	10	1
SUM-235	107807	RR0705_104PC_326_328_SUM-235	104PC	327	3000	40	2760	230	30	3
SUM-177	76991	RR0705_103TC_012.5_014.5_SUM-177	103TC	13.5	1310	20	850	180	2	0
SUM-178	76992	RR0705_103TC_036_038_SUM-178	103TC	37	1890	20	1440	190	3	0
SUM-179	76993	RR0705_103TC_039_041_SUM-179	103TC	40	2070	20	1650	290	3	0
SUM-180	76994	RR0705_103TC_079_081_SUM-180	103TC	79.5	2990	20	2760	260	3	0
SUM-084	65297	RR0705_103PC_020_022_SUM-084	103PC	21	1230	20	810	240	11	1
SUM-054	54323	RR0705_103PC_049_051_SUM-054	103PC	50	1940	30	1520	260	21	2
SUM-085	65298	RR0705_103PC_092_094_SUM-085	103PC	93	2710	20	2430	310	11	1
SUM-055	54324	RR0705_103PC_111_113_SUM-055	103PC	112	2990	20	2770	250	8	1
SUM-087	65299	RR0705_103PC_174_176_SUM-087	103PC	175	3930	20	3840	280	11	1
SUM-050	54306	RR0705_103PC_209_211_SUM-050	103PC	210	4360	20	4550	260	11	1
SUM-052	54322	RR0705_103PC_277_279_SUM-052	103PC	278	5100	20	5500	240	16	2
SUM-053	65528	RR0705_103PC_300.5_302.5_SUM-053	103PC	301.5	5360	30	5770	200	13	1
SUM-224	107805	RR0705_103PC_324_326_SUM-224	103PC	325	5580	30	6000	220	17	2
SUM-253	107804	RR0705_103PC_383_385_SUM-253	103PC	384	6020	30	6470	200	23	2
SUM-249	117616	RR0705_102MC_065_075_SUM-249	102MC	7	460	20	50	60	NA	NA
SUM-227	107808	RR0705_96PC_206_208_SUM-227	96PC	207	480	20	150	220	5	0
SUM-228	107806	RR0705_96PC_222_224_SUM-228	96PC	223	1150	20	710	130	14	1
SUM-089	65300	RR0705_96PC_287.5_289.5_SUM-089	96PC	288.5	1490	20	1070	140	19	2
SUM-090	65301	RR0705_96PC_374_376_SUM-090	96PC	375	2120	20	1730	140	27	3
SUM-232	107809	RR0705_96PC_399_401_SUM-232	96PC	400	2410	20	2070	160	25	3
SUM-199	80463	RR0705_18GC_000_001_SUM-199	18GC	0.5	3850	20	3800	2250	0.9	0
SUM-200	80464	RR0705_18GC_020_021_SUM-200	18GC	20.5	12180	30	13620	2230	1.4	0
SUM-201	80465	RR0705_18GC_040_041_SUM-201	18GC	40.5	15380	30	18180	1090	1.9	0
SUM-249	107821	RR0705_16GC_005_007 _SUM-249	16GC	6	2800	20	2490	620	3.5	0
SUM-250	107822	RR0705_16GC_021_022_SUM-250	16GC	21.5	8800	30	9410	610	2.4	0
SUM-251	107823	RR0705_16GC_041_042_SUM-251	16GC	41.5	17,740	80	20,830	1350	1.2	0

Note: Radiocarbon concentrations are given as fractions of the modern standard, $\delta^{14}C$, and conventional radiocarbon age, following the conventions of Stuiver and Polach (1997). Size-dependent sample preparation backgrounds have been subtracted based on measurements of ^{14}C-free calcite. All results have been corrected for isotopic fractionation according to the conventions of Stuiver and Polach (1997), with $\delta^{13}C$ values measured on prepared graphite using the accelerator mass spectrometry (AMS). These can differ from $\delta^{13}C$ of the original material, if fractionation occurred during sample graphitization or the AMS measurement, and are not shown. NA (Not Applicable)—There are insufficient ages with which to calculate a sedimentation rate.

*Radiocarbon samples analyzed at the Keck Carbon Cycle Accelerator Mass Spectroscopy Facility (Earth System Science Department, University of California, Irvine).

†Laboratory-reported age errors reported to 2 standard deviations; reported in radiocarbon years.

§Calibrated age ranges before A.D. 1950 according to Stuiver and Reimer (1998); calculated using marine reservoir correction and regional ΔR offset ($\Delta R = 16 \pm 78$); errors are reported to 95.4%. Ages are reported in calendar years.

**Calculated by dividing unit thickness by the calibrated age.

Geosphere, published online on 12 November 2015 as doi:10.1130/GES01066.1

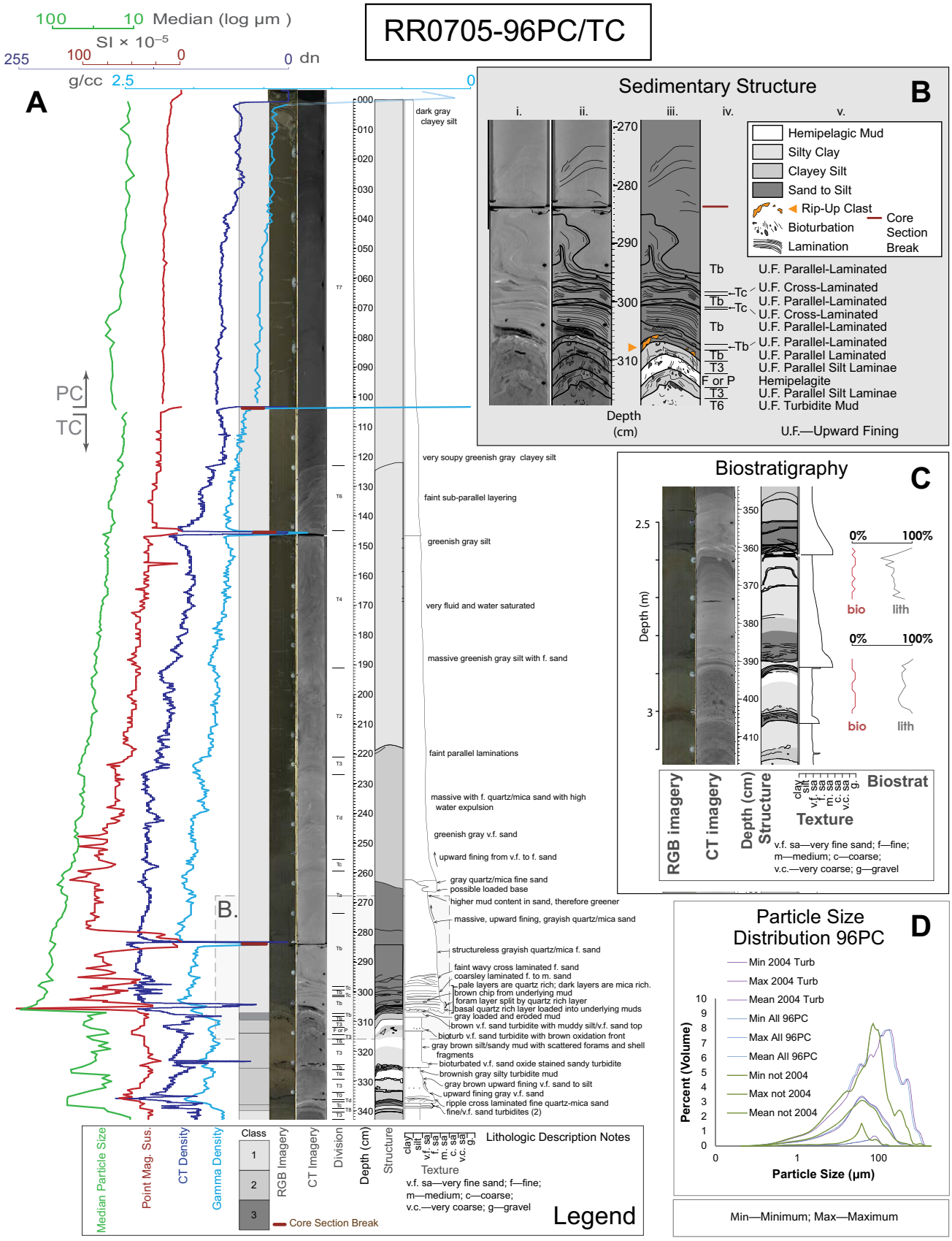

Figure 5 (*on this and following page*). The uppermost (2004?) turbidite from site RR0705 cores 96PC and 96TC, plotted as a composite core. (A) From left to right: median particle size, point magnetic susceptibility, CT (computed tomographic X-ray) density, gamma density, turbidite classification, RGB (red-green-blue) imagery, CT imagery, turbidite structure classification division, depth (cm), turbidite structure (lithologic log), texture, and the lithologic notes are plotted versus depth. Geophysical log symbols and grain sizes as in Figure 2. Mag. Sus.—Magnetic Susceptibility; RGB—red, green, blue; CT—computed tomography; v.f. sa—very fine sand; f. sa— fine sand; m. sa— medium sand; c. sa—coarse sand; v.c. sa— very coarse sand; g— gravel. (B) Detailed turbidite structure based on CT imagery. From left to right: i—CT imagery uninterpreted; ii—CT imagery interpreted; iii—turbidite structure interpretation; iv—turbidite structure division classification; v—turbidite structure description (U.F.—upward fining). Ta—Bouma A; Tb—Bouma B; Tc—Bouma C; Td—Bouma D; T0—6—Stow Division 0—6; F or P—Bouma F, Hemipelagite, or Pelagite. (C) Results from smear slide based vertical biostratigraphic transects for core 96PC. Percent biogenic (bio) and percent lithologic (lith) are plotted versus depth (in m). (D) The mean, minimum, and maximum particle size distribution for sediments collected within the uppermost turbidite (in purple) and within hemipelagic sediments underlying the uppermost turbidite (in green) are plotted. These are compared with the combined distributions (in blue). Turb—Turbidite.

Geosphere, published online on 12 November 2015 as doi:10.1130/GES01066.1

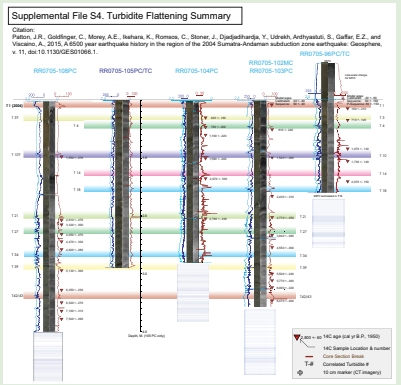
Supplemental File S4. Turbidite Flattening Summary

[4]Supplemental File S4. Turbidite flattening summary. Core data (geophysical data, imagery data) are flattened to stratigraphic horizons as in Figures 9 and 10 using symbols as in Figure 8. This effectively renders the stratigraphy on a time basis across the area, thus each turbidite represents a time horizon. The vertical scales are nonlinear except for 105PC, which is the reference core and is plotted at the true vertical scale. Grid below cores except 105 is the flattening matrix, and shows the vertical scale changes required, bars were originally evenly spaced. Cores 102MC and 103PC are composited together, as are 96PC and 96TC. Local variability is quite high in this core set, best illustrated by the ~3 m thickness of the 2004 bed in 96PC; this bed is more typically 10–15 cm thick at other sites. The anomalous depositional style at the site of 104PC is also illustrated well. Many turbidites that have low structural complexity at other sites are interpreted as the same events in 104, but with a common depositional mode with numerous laminae composing a single bed. We interpret this depositional style as potentially the result of amalgamation of numerous small local failures or possible headward progressive failures following the initial ground failure. Similar site effects are apparent at the site of 96PC/TC, which for all events shows an expanded, sandier version of what we interpret to be correlative beds seen elsewhere. The 2004 bed is the most extreme of these, but all other beds at this site show a similar expanded structure. Also illustrated are periods of low rates of turbidite emplacement at some sites in restricted time periods. For example, in 108PC, few turbidites are deposited post T-21 time, about 2800 yr ago. While the likely 2004 bed is present, only ~4 beds were emplaced between these times. That time interval may contain other events too diffuse for robust interpretation. The turbidite sequence is older than ~2800 yr, well represented, and correlated to other sites. This site either became a poor recorder of events after 2800 yr ago, our preferred interpretation, or the site could alternatively have been a site of lower ground motions after 2800 yr ago. Please visit http://dx.doi.org/10.1130/GES01066.S4 or the full-text article on www.gsapubs.org to view Supplemental File S4.

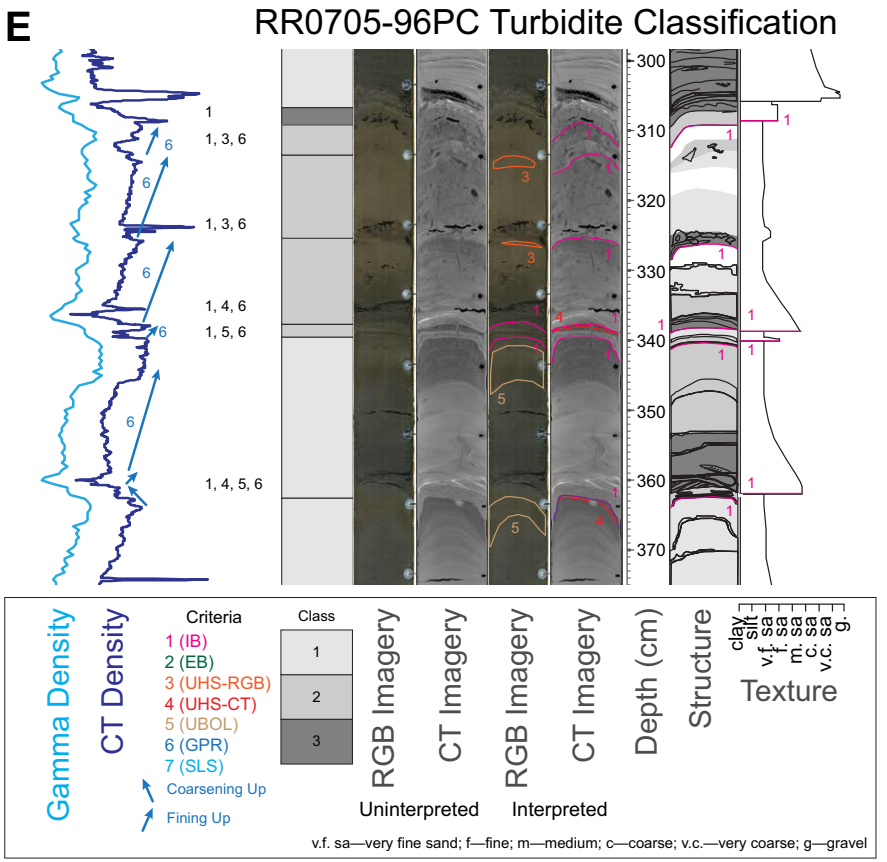

Figure 5 (*continued*). (E) Core 96PC is plotted versus depth (in cm), from left to right: gamma density, CT density, turbidite criteria, turbidite classification, uninterpreted imagery, interpreted imagery, depth (cm), turbidite structure, and texture. Each criterion met is listed for each turbidite (numbered 1–7). The locations for where, in the core, these criteria are met are labeled and designated by color (see legend; criteria are listed and described in the text). IB—Impulsive Base; EB—Erosive Base; UHS-RGB—Underlying Hemipelagic Sediment–RGB Imagery; UHS-CT—Underlying Hemipelagic Sediment - CT Imagery; UBOL—Underlying Brown Oxidation Laminae; GPR—Geophysical Property Relation; SLS—Sediment Loading Structures.

Turbidite Class

1	More Certainly a Single-Pulse or a Multi-Pulse Turbidite
2	Less Certainly a Single-Pulse or a Multi-Pulse Turbidite
3	Indeterminately a Single-Pulse or a Multi-Pulse Turbidite

Regional Lithostratigraphy within the 2004 Rupture Zone

In Figure 8 and Supplemental Files S3 and S4[4] we show the compilation of 43 turbidites across the 2004 rupture area. Figure 8 and Supplemental File S3 show these at true vertical scale; Supplemental File S4 is a working diagram with the turbidite sequence flattened to key horizons in the sequence. Tie line line-weight thicknesses and patterns on the plots reflect our confidence in individual ties based on the individual and stratigraphic sequence log correlations, age similarity, and number of sites correlated. Of these 43, 28 are found in core 108, 39 are in core 105, 36 are in core 104PC, 43 are in cores 102MC and 103PC, and 17–18 are in core 96PC. The correlation framework is based on four primary factors: (1) the turbidites are in similar stratigraphic sequence; (2) the turbidites comprise distinctive subgroups of beds observed at multiple sites; (3) the turbidites have shared fingerprints with distinctive details; and (4) they have compatible timing based on radiocarbon ages. The turbidite structure or fingerprint varies among the turbidite beds. Those beds or subgroups of

Geosphere, published online on 12 November 2015 as doi:10.1130/GES01066.1

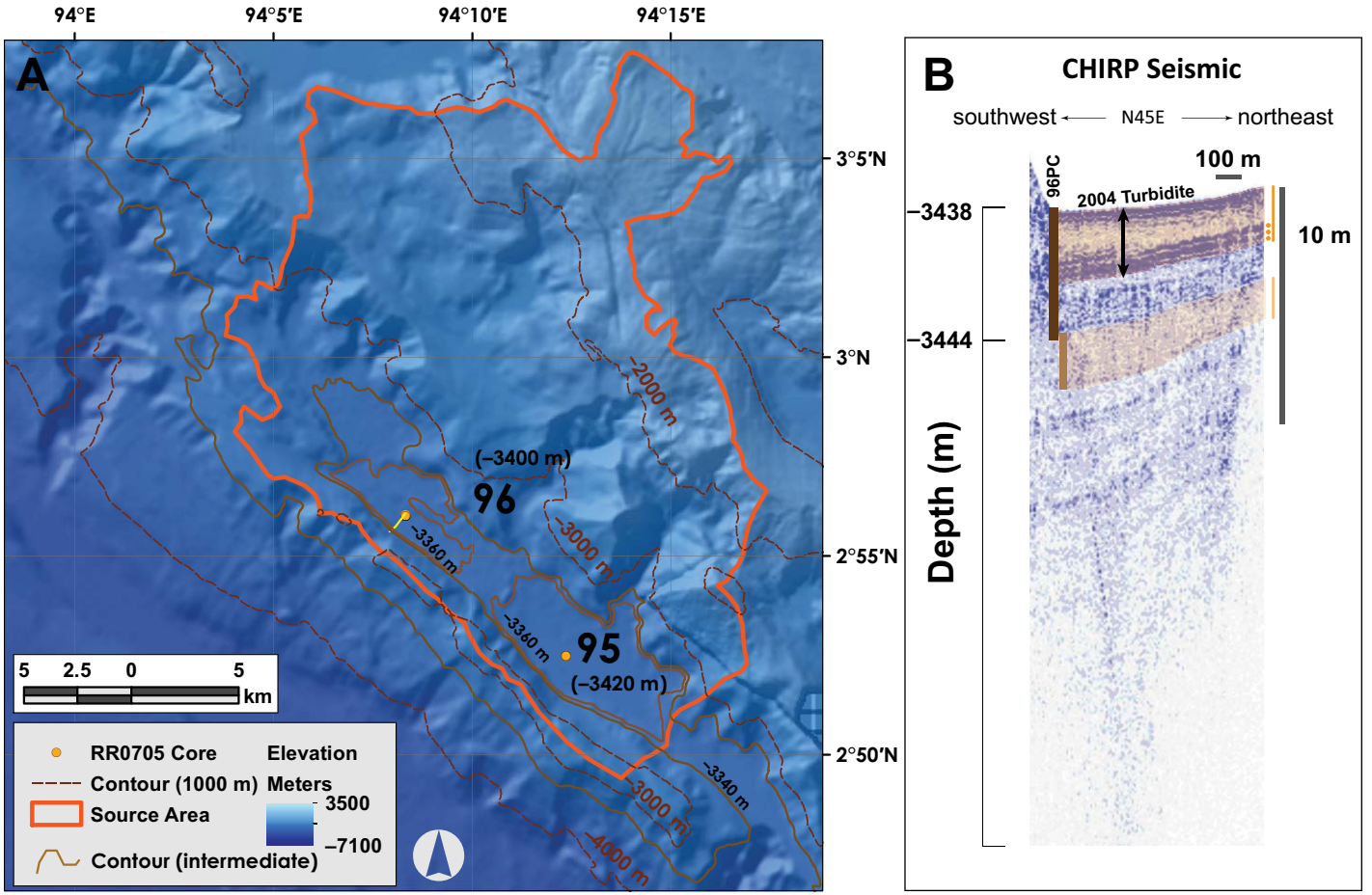

Figure 6. (A) Core sites 96 and 95 are plotted as orange dots, with the seawater depths (–3400 and –3420 m respectively). Depth contours are in meters. Intermediate contours of –3360 m and –3340 m depict the shape of the basins. The CHIRP (compressed high-intensity radar pulse) seismic profile track line is plotted on the map as a yellow line crossing the core 96 core site. (B) The CHIRP seismic profile crossing the basin at the core 96 core site. The core length of 96 is plotted in dark brown. We speculate that T-18 is imaged in the subsurface along this southwest-northeast CHIRP profile. The depth for turbidite T-18 is plotted as a light brown vertical line (discussed in text). The turbidite boundary interpreted in seismic data is overlain in transparent brown. Southeast-northeast profile transect has an orientation of N45E. The lighter brown line and lighter brown polygon designates a possible thick turbidite (T-18), the uppermost tail of which is at the base of core 96PC.

beds with particularly distinctive signatures anchor the correlation, defining the more confident ties, while others that are less distinctive but still in a consistent temporal and stratigraphic sequence are shown with lower confidence symbols. The superposition and sequence of these deposits with unique signatures provides boundary conditions within cores, between cores (PC and TC pairs) and between core sites. When turbidites can be correlated between cores 96, 103, and 104 or from 103, 104, 105, and 108, representing a strike length longer than accretionary prism faults (Kopp et al., 2008), they are given a T-number. There may be additional correlatable turbidites, but they do not have geophysical signatures sufficient to uniquely identify them. Figure 8 shows that the strongest correlated deposits include regional turbidites T-1–T-12, T-16, and T-18–T-21 (boldest tie lines). Of these, key correlated beds designated T-1, T-3, T-4, T-10, T-21, T-27, T-34, T-39, and T-42 and T-43 are the distinctive beds highlighted in Supplemental File S4, and those to which the regional stratigraphy has been flattened. Supplemental File S4 represents conversion of the vertical scales to time scales, with each bed representing a time horizon.

Geosphere, published online on 12 November 2015 as doi:10.1130/GES01066.1

TABLE 3. RADIOCARBON AGES UNDERLYING THE UPPERMOST TURBIDITE IN CORES 96, 102, AND 90

Core	Sample name	Laboratory age*	Error	Calibrated age†	Error	Sequence age§	Error	P_Sequence age§	Error
96PC	RR0705_96PC_206_208_SUM-227	480	20	–30#	60	50	160	60	150
102MC	RR0705_102MC_065_075_SUM-249	460	20	40	40	50	60	NA	NA
90MC	RR0705_90MC_002_003_SUM-250	410	20	40	30	40	40	NA	NA

Note: NA (Not Applicable)—There are insufficient ages with which to to construct a P_Sequence age model.
*Laboratory-reported age errors reported to 2 standard deviations; reported in radiocarbon years.
†Calibrated age ranges before A.D. 1950 according to Stuiver and Reimer (1998); calculated using marine reservoir correction and regional ΔR offset (ΔR = 16 ± 78); errors are reported to 95.4%. Ages are reported in calendar years.
§Refer to text for the definition of Sequence and P_Sequence.
#The calibrated age is 1950 – –30, or, 1980 AD.

Cores 104, 103, and 96 are in sedimentologically isolated slope basins and core 105 is in the trench (Fig. 3A). Together these cores span ~170 km of the margin. Core 104 source areas may be somewhat shared with core 105, but a landward-vergent fold in the trench probably isolates 105 from these sources. Figure 9 shows an example of how the turbidites are tested for correlation from core to core. For each sequence, there are two panels: (1) the unscaled cores and (2) the flattened geophysical properties and flattened CT imagery. The unscaled core figures are vertically clipped versions of the main core figures, clipped to the stratigraphic section of interest. From left to right, the core figures show gamma density (light blue), CT density (dark blue), the lithologic log, the CT scan, and PMS (red). Green tie lines show the correlations for the bases of these turbidites, as in Figure 8. We then group each geophysical property trace from each core. Each data set has the same range of values for the horizontal axes (gamma density = 0–2.5 g/cm^3; CT density = 0–255 dn, gray-scale digital number, scaled in these figures for viewing ability; and PMS = 0–150 SI × 10^{-5}). These geophysical data maintain their original vertical scale. The lower panel shows how geophysical data are flattened to the bases and tops of the turbidites using one core at the fixed 100% vertical scale (note that the tie lines are horizontal). We choose one core (labeled in purple in Fig. 9) to hold at a fixed vertical scale and then scale (flatten) the data from other cores to that core. We do this iteratively to test possible links or lack thereof between sites. Flattened sequences should fail to show similarities between sites and or violate age constraints if sequences are unrelated.

Basin-Basin Comparisons

Turbidite series T-3–T-5 is correlated between cores 105, 104, 103, and 96, based on the stratigraphic sequence shared between these cores. T-3 and T-4 are multipulse turbidites with fine and very fine sand that fines upward to medium to coarse silt. T-3 and T-4 are both preceded by thinner multipulse coarse to medium silt turbidites, here noted as T-5. In core 105PC these turbidites comprise ~3 main upward-fining pulses; overall, the sequence coarsens upward (each superposed bed is coarser than its underlying bed). While the other cores have lower turbiditic sedimentation rates, the geophysical data show a concomitant upward trend in turbidite mass (coarsening upward), with a multipulse geophysical property trend. Cores 104PC and 103PC have turbidites underlying T-3 that are slightly different (upward fining in core 104PC; a low mass overall for core 103, resulting in an indistinguishable geophysical fingerprint). The two ^{14}C ages underlying T-3 have overlap in their error ranges.

With a similarly large regional extent, we correlate T-6 and T-8 between these same cores 105PC, 104PC, 103PC, and 96PC (Figs. 8 and 9B). The overlying sequence of T-3–T-5 provide an upper boundary condition for these correlations. T-7 in these cores forms a sequence of a thin muddy turbidite overlain by a thicker and coarser multipulse turbidite. T-8 is a fine sand to silt, multipulse turbidite with upward-fining beds. Overall, the turbidite is upward coarsening in cores 96PC and 103PC (each superposed bed is coarser than its underlying bed), and upward fining in cores 105PC and 104PC. T-6 is fine sand to silt, multipulse, upward-fining turbidite. In core 104, the base of T-7 is a sequence of ~32 coarse silt to very fine sand, 1–3-mm-thick, upward-fining laminations. Also in core 104PC, this coarser turbidite head is overlain by a tail that has 1–3 cm coarse silt laminations interbedded with ~6 very fine sand, 1–3-mm-thick laminations. T-7 in other cores has a similar depth-density sequence, but in 96 and 104 it has a more expanded section, so the stratigraphic details are less observable in the other cores. The 2 ^{14}C ages in cores 96PC and 104PC have overlap in their 95.4% error ranges.

Due to the poor preservation of turbidite structure and the fine texture of turbidites T-12–T-17 in 96PC, these turbidites are here only correlated between cores 105PC, 104PC, and 103PC (Figs. 8 and 9C). These cores span ~70 km and represent a region of at least 2100 km^2. This turbidite sequence shows how stratigraphic order (superposition) plays a role in addition to the geophysical property trend fingerprints. A key turbidite is T-18, a fine sand to silt, upward-fining multipulse turbidite. We compare the sequence T-20–T-17 in regard to the sequential upward change in relative trends of CT density and PMS data. For PMS, T-20 has relative intermediate values, T-19 has lowest values, and T-18 has the largest values. The gamma density sequence begins with the lowest values for T-20, intermediate values for T-19, and the largest values for T-18. These sequential trends match across all three cores, though the variability in

Geosphere, published online on 12 November 2015 as doi:10.1130/GES01066.1

TABLE 4A. ^{210}Pb RESULTS FOR CORES 94PC, 105TC

	Sample identification†	^{210}Pb (dpm/g)	Error	Depth (cm)
RR0705-94PC				
	PR0705-94 PC 02 04	4.876	0.371	4
	PR0705-94 PC 15 17	1.266	0.323	18
	PR0705-94 PC 17 19	0.000	0.249	20
	PR0705-94 PC 19 21	0.000	0.265	22
	PR0705-94 PC 21 23	0.000	0.207	24
	PR0705-94 PC 23 25	0.130	0.309	26
RR0705-105TC				
	PR0705-105 TC 02 04	1.611	0.431	3
	PR0705-105 TC 04 06	0.000	0.347	5
	PR0705-105 TC 07 09	0.000	0.367	8
	PR0705-105 TC 10 12	0.000	0.331	12
	PR0705-105 TC 17 19	0.000	0.244	18
	PR0705-105 TC 21 23	0.000	0.339	22

TABLE 4B. ^{210}Pb RESULTS FOR CORES 96PC, 96TC, and 102MC

Sample Number*	Sample identification†	^{210}Pb (dpm/g)	Error	Depth (cm)
RR0705-96PC				
7169	PR0705-96 PC 22-23	7.926	0.256	222.5
7170	PR0705-96 PC 23-24	7.303	0.236	223.5
7171	PR0705-96 PC 24-25	10.369	0.338	224.5
7172	PR0705-96 PC 25-26	11.220	0.363	225.5
7173	PR0705-96 PC 26-27	8.995	0.298	226.5
7174	PR0705-96 PC 27-28	4.312	0.145	227.5
7175	PR0705-96 PC 28-29	3.968	0.134	228.5
7176	PR0705-96 PC 29-30	6.082	0.206	229.5
7177	PR0705-96 PC 30-31	2.463	0.086	230.5
RR0705-96TC				
7240	PR0705-96 TC 126-127	4.553	0.186	126.5
7241	PR0705-96 TC 127-128	4.615	0.193	127.5
7242	PR0705-96 TC 128-129	4.208	0.176	128.5
7243	PR0705-96 TC 129-130	4.197	0.176	129.5
RR0705-102MC				
7254	PR0705-102 MC 6-7	16.999	0.581	5.5
7253	PR0705-102 MC 7-8	14.010	0.489	6.5
7252	PR0705-102 MC 8-9	6.639	0.238	7.5
7251	PR0705-102 MC 9-10	4.507	0.160	8.5
7250	PR0705-102 MC 10-11	5.527	0.226	9.5
7249	PR0705-102 MC 11-12	5.417	0.219	10.5
7248	PR0705-102 MC 12-13	2.759	0.119	11.5
7247	PR0705-102 MC 13-14	2.465	0.116	12.5
7246	PR0705-102 MC 14-15	2.768	0.128	13.5
7245	PR0705-102 MC 15-16	2.385	0.117	14.5
7244	PR0705-102 MC 16-17	2.525	0.120	15.5

Note: dpm—disintegrations per minute.
*Sample Number assigned in the laboratory during analysis.
†Sample identification lists the cruise name, the core name, and the sample interval.

trends of the geophysical data for each deposit reflects how these proxies for grain size are imperfect. T-21 has unique sequences that are shared between cores in slope cores (96PC, 103PC, 104PC, and 108PC) and trench cores (105PC, 03PC, 05PC; Patton et al., 2013a). T-21 is a thicker multipulse, upward-fining, fine sand to silt turbidite (Figs. 8 and 10). PMS data show a large maxima near the base of this deposit, most remarkable in cores 105PC and 104PC, although it is in 108PC and 103PC as well. In cores 108PC and 105PC, T-21 is 60 cm and 23 cm thick respectively, with a 20-cm-thick sandy base in each core. Core 108PC has several upward-fining pulses of laminated and massive mud that are only ~3 cm thick in core 105PC. The 3 ^{14}C age estimates underlying T-21 in cores 108PC, 104PC, and 103PC overlap in each of their error ranges.

In addition to the well-correlated deposits, we also describe some of the less-well correlated or uncorrelated deposits. Some of these turbidites are well correlated between some cores, but not in others. Between 108 and 105, T-4, T-6, and T-11 are not well correlated possibly due to the high bioturbation in core 108. There are fewer turbidites in 108 younger than T-21, suggesting a change in either the site or the delivery mechanisms younger than T-21 time, making it problematic to correlate individual beds to 108 during that time span.

Core 96PC bottomed in T-18, and thus T-18 is partially contained in core 96PC (Fig. 8). Core 96PC appears to have the muddy tail for the T-18 turbidite, but this is difficult to test since the base of the T-18 deposit is absent. If the lowermost turbidite in core 96PC is T-18, a coarse sandy base of the turbidite, as found in other cores, is missing. Considering the thickness of the tail of this turbidite and turbidites with similar tail thicknesses in other cores, the sandy base may be on the order of tens of centimeters, and likely stopped the penetration of core 96PC. Possibly supporting this hypothesis is the seismic reflection data, which shows an acoustically opaque deposit below the depth of the core that appears to fade upward to a depth overlapped by the core depth (dark brown vertical line in Fig. 6B). The spatial limit of the seismic reflection profile is designated by a yellow line in Figure 6A.

Basin-Trench Comparisons

The first basin to trench comparison is between core 108 in a slope basin and core 107 in the trench 44 km distant. Core 108 is in a small basin that has a 25-m-high sill to the north and a 200-m-high sill to the south (Figs. 3A, 3C). This basin probably partially drains to the north, given that turbidity current flow depths may be >100 m (Muck and Underwood, 1990; Völker et al., 2008). Core 107 is in the trench axis 45 km to the southwest of core 108. The stratigraphy in cores 108PC and 108TC correlates well, with no apparent missing sediment from core 108PC. The TC has ~45 cm of repeated stratigraphic section, which happens if the core penetrates the seafloor multiple times (which may occur when the ship is heaving sufficiently). We observe that core 107 has more turbidites than in core 108, between T-3 and T-21. Core 108PC is bioturbated in this section, possibly confounding the geophysical property representation of those deposits, making it more difficult to uniquely correlate strata. T-14 in core

Geosphere, published online on 12 November 2015 as doi:10.1130/GES01066.1

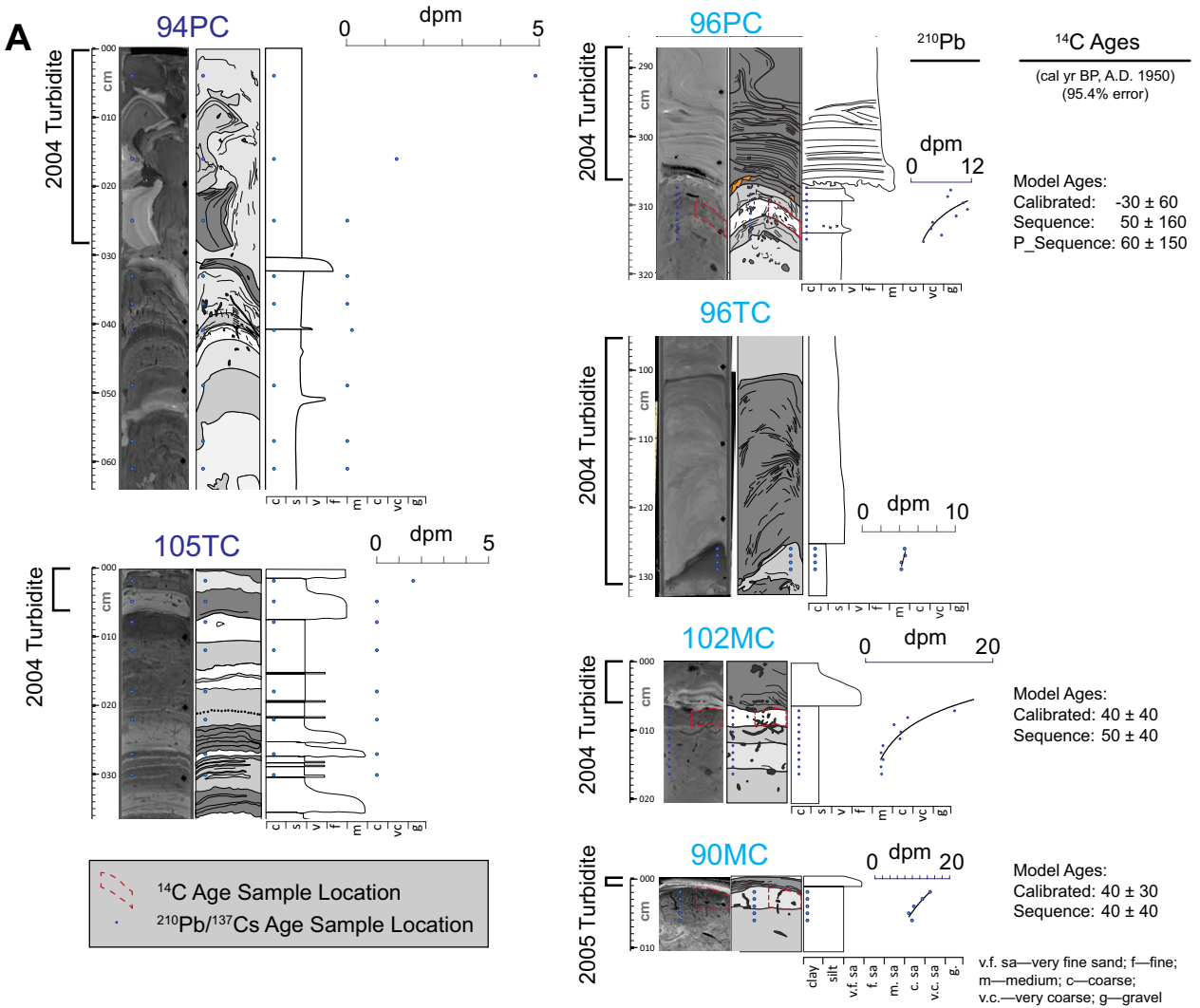

Figure 7 (*on this and following page*). Radiometric ages of the uppermost turbidite. Several examples of the likely 2004 and 2005 deposits are presented. (A) Lithologic details and ^{210}Pb analytical results are plotted for cores 94PC, 105TC, 96PC, 96TC, 102MC, and 90MC. ^{210}Pb decay per minute are plotted vs. depth with blue dots, alongside core data. Regressions are plotted for the cores that have depth-continuous samples. Core data include core depth (cm), CT (computed tomographic X-ray) imagery, turbidite structure, and sedimentary texture. ^{14}C ages are reported as cal yr BP with 95.4% uncertainty. Calibrated, Sequence, and P_Sequence ages are presented as discussed in the text (Table 5). ^{14}C sample locations are outlined in dashed red lines.

108 also has an indistinct geophysical property trend, although it fines upward in both cores. Based solely on the comparison of T-14 between these two cores, this is at best a poor correlation. The correlation of T-14 between cores 108 and 107TC is supported by the correlation between cores 107TC and 105PC.

Moving southward, we compare strata between two trench cores, 107 and 105, 40 km apart (Supplemental Files S1 and S3). Core 107 is located in the axis of the trench at 4520 m water depth. While collecting core 107, the core tripped prematurely at ~1134 m water depth. This changed the depth configuration of the PC and the TC, leaving the PC at a lower position (the PC cored sediment before the TC). T-1 is present in 107PC, but not 107TC, the reverse of the normal situation where the TC is more likely to sample the uppermost sediment. Sediment in core 107PC is highly disturbed from coring, but is sufficiently preserved to tentatively correlate with 107TC. Core 105 is located on a ≥20-km-wide terrace that is ~100 m above the depth of the trench axis at a

Geosphere, published online on 12 November 2015 as doi:10.1130/GES01066.1

B Sedimentation Rate = -(ln2/(slope * 22.3))

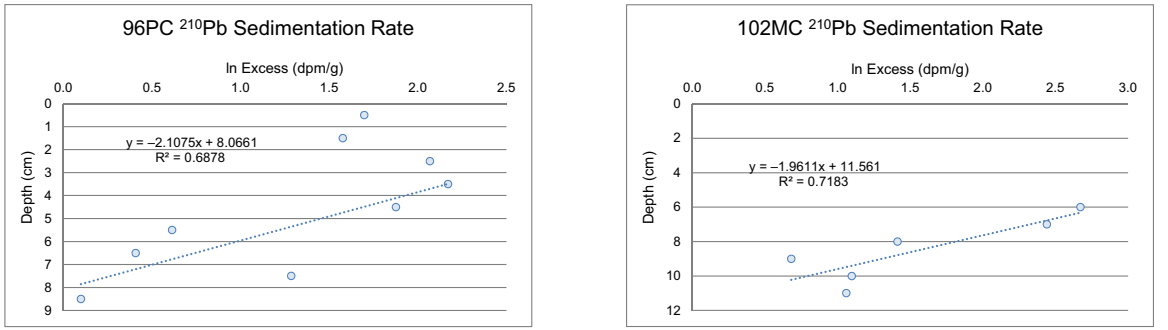

96PC Sedimentation Rate = 0.015 cm/yr

102MC Sedimentation Rate = 0.016 cm/yr

C

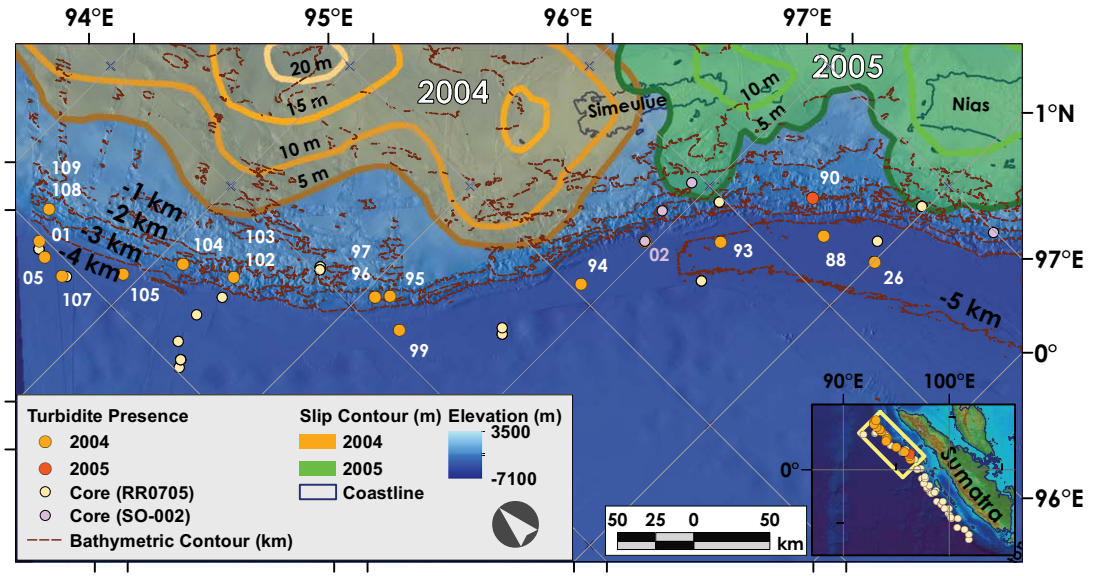

Figure 7 (*continued*). (B) Plots of Excess ^{210}Pb for 96PC and 102MC. Sedimentation rates for 96PC and 102MC are calculated with the method in Ghaleb (2007). (C) Map showing the cores that contain a deposit that may have resulted following the 2004 Sumatra-Andaman subduction zone earthquake. Cores with a possible 2004 seismoturbidite are plotted in light orange. Core 90MC, with a possible 2005 seismoturbidite, is plotted in dark orange. Other RR0705 cores are plotted in yellow and SO002 cores are plotted in pink. SO002 core 02, labeled in pink, possibly has the 2004 seismoturbidite (Sumner et al., 2013). The 2004 and 2005 slip contours are shown in orange and green, respectively (Chlieh et al., 2007, fig. 11 therein; Chlieh et al., 2008, fig. 20 therein).

depth of 4480 m, 11 km from the trench axis, which has a depth of 4550 m. Core 105 is west of a gently sloping, 0.5-km-high landward-verging anticline (Henstock et al., 2006; Graindorge et al., 2008; Sultan et al., 2009) that shields this site from direct sedimentation from higher relief bathymetry to the east. 105TC sampled ~15 cm more sediment than 105PC, so core 105 is shown as a PC-TC composite core. T-1 is apparently present in core 105TC. The uppermost ^{210}Pb sample has presence of activity beneath this young deposit (Fig. 7). The gamma and CT density data for T-2 in cores 105TC and 107TC match nicely. While T-3 in core 107TC has a low dynamic range in turbidite texture and geophysical property trends, we correlate the sequence of T-4 and T-5 with higher confidence (Figs. 8 and 9; Supplemental File S3); considering the sequence above T5, this supports our correlations of T-2 and T-3. We correlate T-7, T-10, and T-11 from cores 107TC to 105PC, with higher confidence due to shared sequences of geophysical property trends and shared patterns of turbidite structures. In core 107TC, turbidites underlying T-10, down to T-14, are disturbed due to coring and are therefore more difficult to correlate.

Geosphere, published online on 12 November 2015 as doi:10.1130/GES01066.1

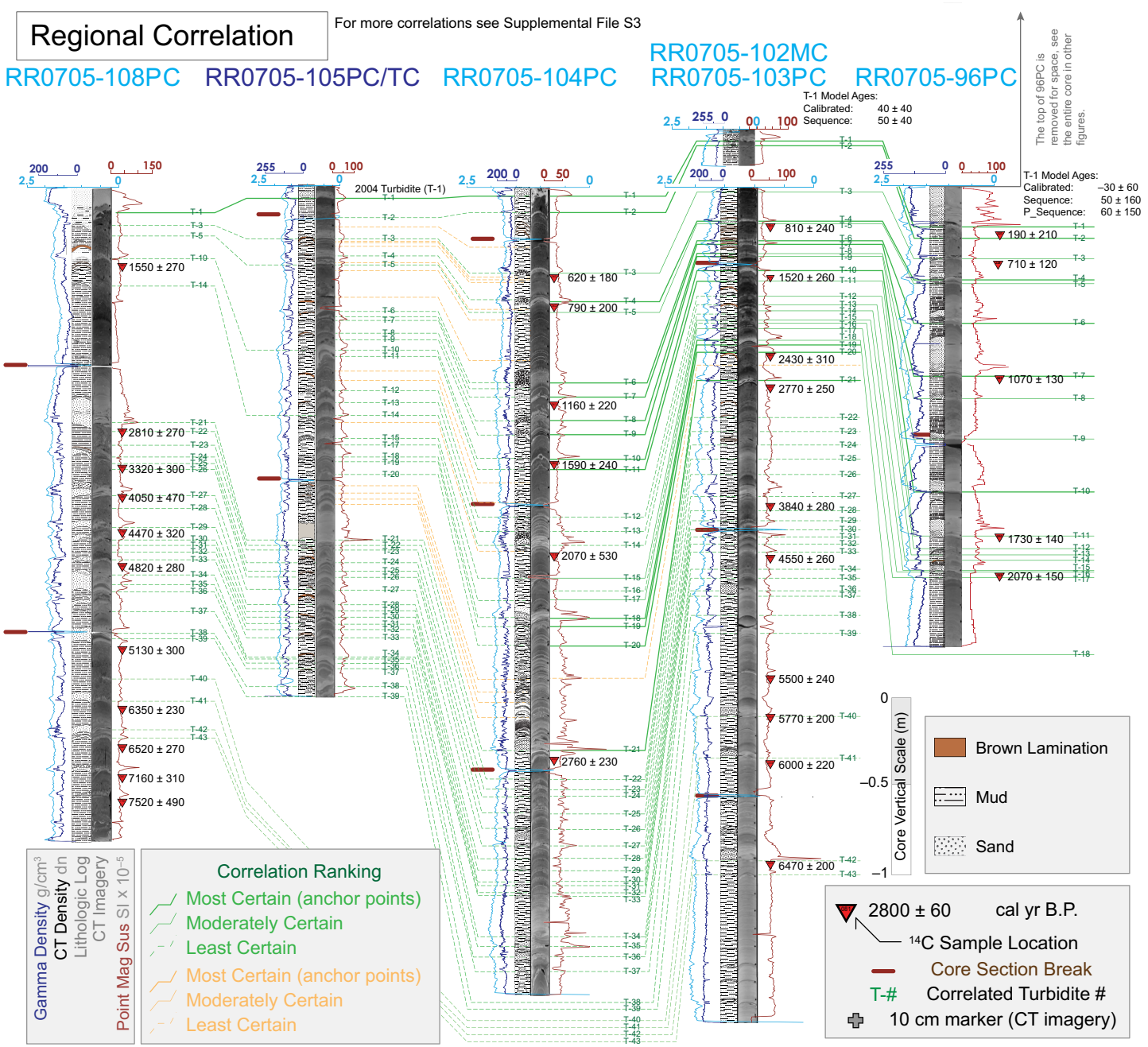

Figure 8. Regional stratigraphic correlations. Stratigraphic correlations between key cores use lithology, CT (computed tomographic X-ray), core geophysical properties (see Fig. 2 caption), and ^{14}C data. Multisensor core logging (MSCL) data are plotted as in previous figures. CT imagery displays lower density material in darker gray and higher density material in lighter gray. Slope cores are in light blue; trench cores are in dark blue. The ^{14}C ages are reported in calendar (cal) yr B.P. (A.D. 1950). Green correlation tie lines designate correlation confidence with line thickness and pattern and are positioned generally at the base of the turbidites. Correlated turbidites are designated with T-, and correspond to the green tie lines, beginning with the most recent turbidite (T-1, 2004). Orange correlation tie lines show correlations of strata that are either sedimentary layers within turbidites or turbidites that do not have numbers. The complete correlation diagram with all cores and turbidite classification is shown in Supplemental File S3. Model ages are presented for T-1 in cores 102MC and 96PC (Fig. 7; Table 3).

Geosphere, published online on 12 November 2015 as doi:10.1130/GES01066.1

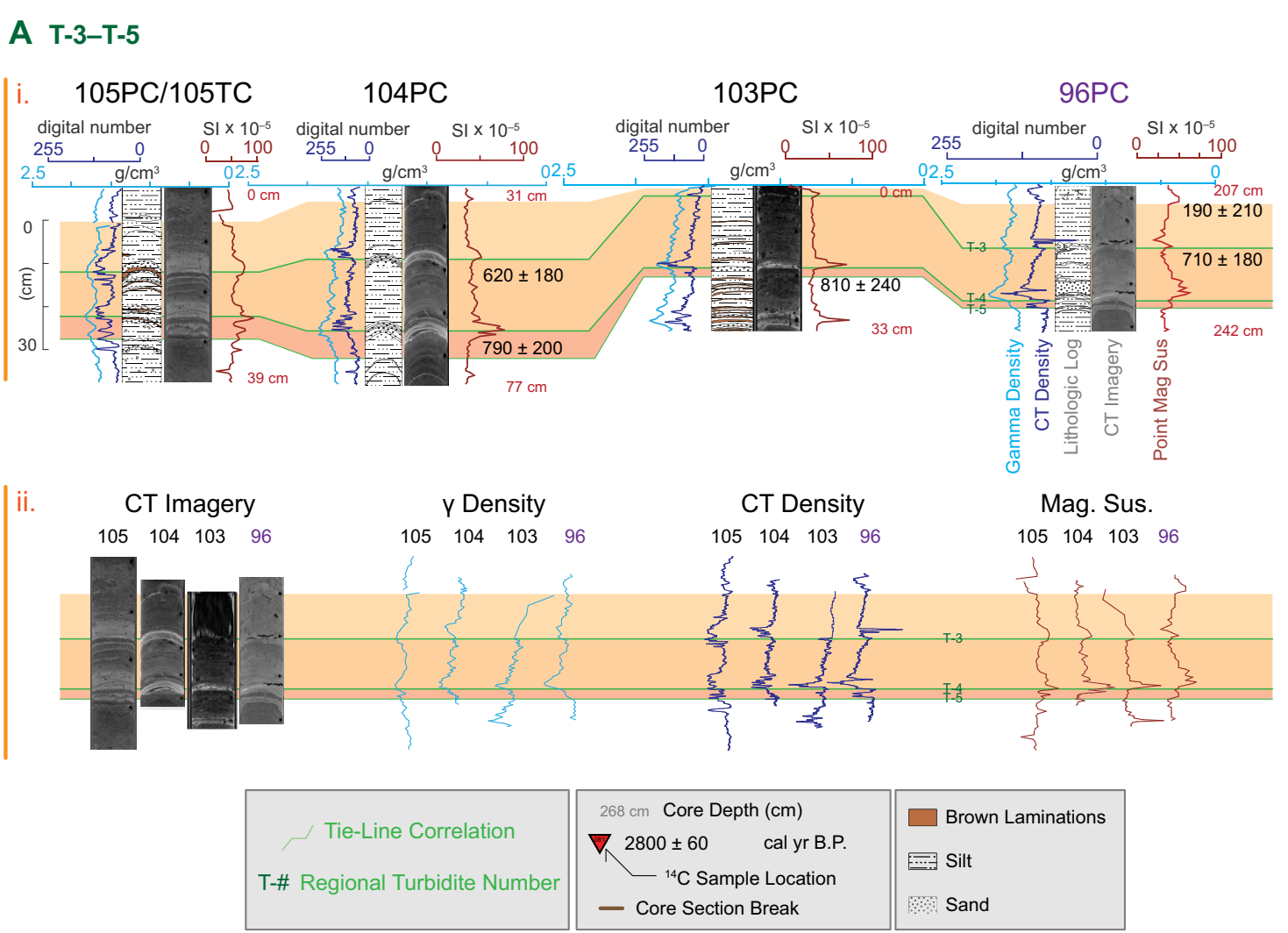

Figure 9 (*on this and following two pages*). Geophysical flattening process is displayed for some correlated turbidites. Geophysical traces are plotted as in Figure 8. Each turbidite sequence has three panels with different core configurations [left to right: gamma density, CT (computed tomographic X-ray) density, RGB (red-green-blue) imagery, CT imagery, point magnetic susceptibility (Mag. Sus.), and ^{14}C ages with 95.4% error]. (i) Vertically true scale of core data. (ii) Geophysical data are flattened to stratigraphic contacts. Green correlation tie lines are aligned at the general base of the turbidites and designate correlation confidence with line thickness and pattern. (A) Turbidites T-3–T-5 are correlated between cores 105PC, 104PC, 103PC, and 96PC. Core data are flattened to core 96PC.

In core 107, the turbidites underlying T-14 are muddy and have low dynamic range in density, so do not have characteristic trends in geophysical properties. We correlate the lower turbidites in core 107TC with core 105PC with low confidence. Because there are no ^{14}C ages in the trench cores, all correlations are designated with dashed lines in Figure 8 and Supplemental File S3.

Cores 105 and 104 are 40 km apart; core 104 is located at 3480 m water depth near the base of an ~1.5-km-tall cliff, within and near the edge of a slope basin that is being dissected by a submarine canyon from the southeast (Fig. 3). Cores 104PC and 104TC contain very similar uppermost stratigraphy, including the coarse sandy base of T-1 (core 104TC also includes two sections of repeated stratigraphic section). The turbidites in core 104 are more thinly laminated than those in 105, but the geophysical property trends match well for most of these correlated turbidites. Correlations of T-3–T-8 and T-17–T-20 are presented here (Fig. 9). Laminae between T-20 and T-21 are closely spaced and difficult to interpret in core 104PC. We are not certain whether these are laminations in the upper part of T-21, or separate turbidites. T-21 provides a

Geosphere, published online on 12 November 2015 as doi:10.1130/GES01066.1

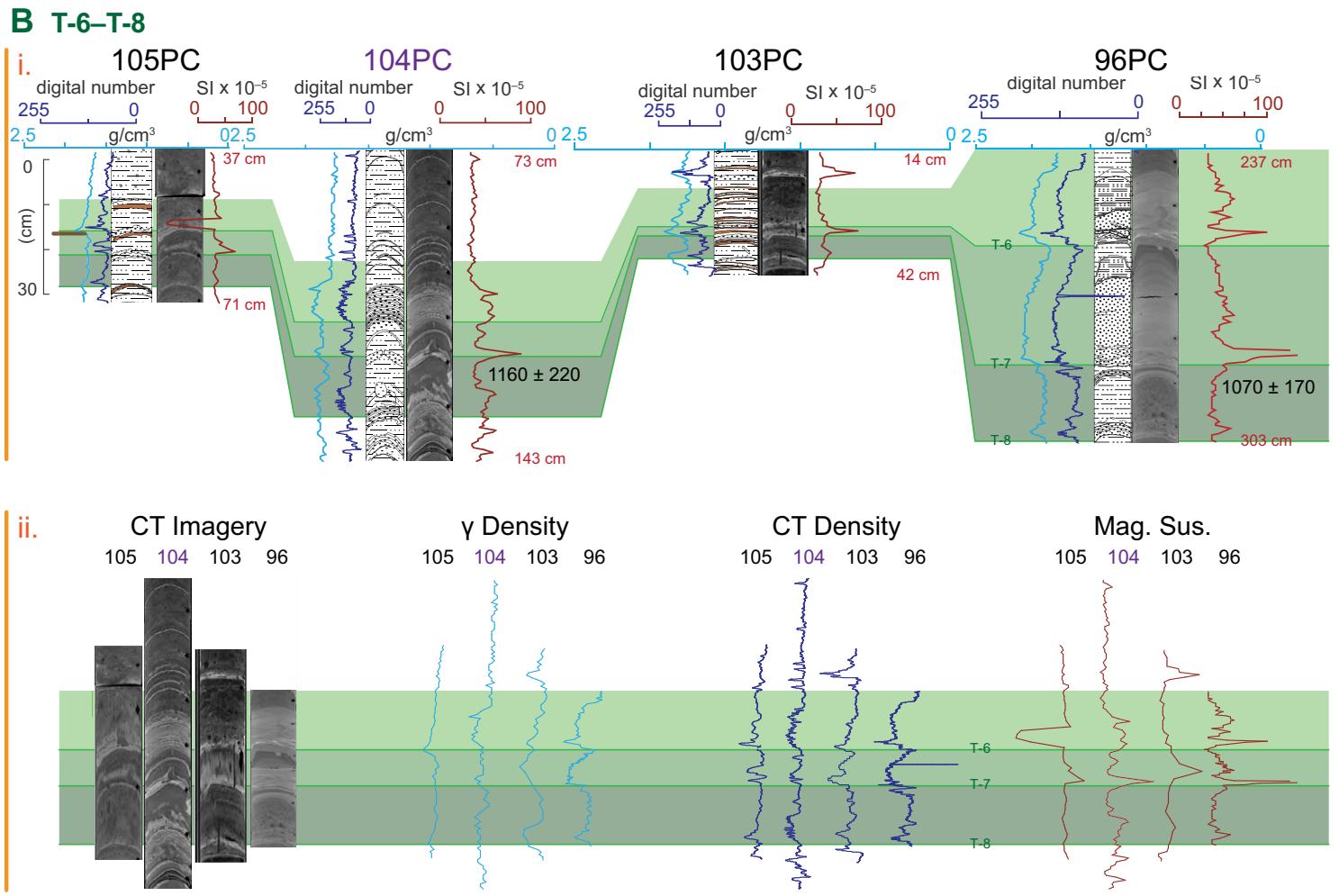

Figure 9 (*continued*). (B) Turbidites T-6–T-8 are correlated between cores 105PC, 104PC, 103PC, and 96PC. Core data are flattened to core 104PC.

robust anchor point and boundary condition for the underlying correlations T-22–T-37. We correlate turbidites T-22–T-34 with lower confidence due to the closely spaced finely laminated turbidites in core 104. These finely laminated turbidites are difficult to distinguish from each other within core 104.

Cores 104 and 103, the next trench-slope core pair, are 34 km apart. Core 103, at a depth of 3070 m, is located near the center of a 2–4-km-wide flat-bottomed slope basin that slopes upward at ~1° to the east, with no resolvable channels (Fig. 3). The basin is enclosed by a 20 m sill on the northwestern boundary, which probably permits partial flows of sediment outside of this basin. When combined with 102MC, at the same site, we correlate turbidites between cores 103, 102MC and core 104 with high confidence, ranging from T-1–T-11, T-15, and T-17–T-21. Core 103 is missing T-1, but T-1 and T-2 are sampled in core 102MC (Supplemental File S3). The lowest ~50 cm of 103TC contains repeated stratigraphic section. Turbidites in core 103 are much thinner overall than in core 104 (e.g., the base of T-7 is at a depth of 32 cm in core 103PC and at a depth of 119 cm in core 104PC). In cores 103PC and 104PC, the sequence of T-8–T-9 shows an overall upward increase in PMS values, helping to uniquely identify these correlated turbidites. The sequence T-10–T-11 also has matching and superposed geophysical fingerprints in cores 103PC and 104PC, best viewed in the PMS data. The turbidites between T-12 and T-17 are too

Geosphere, published online on 12 November 2015 as doi:10.1130/GES01066.1

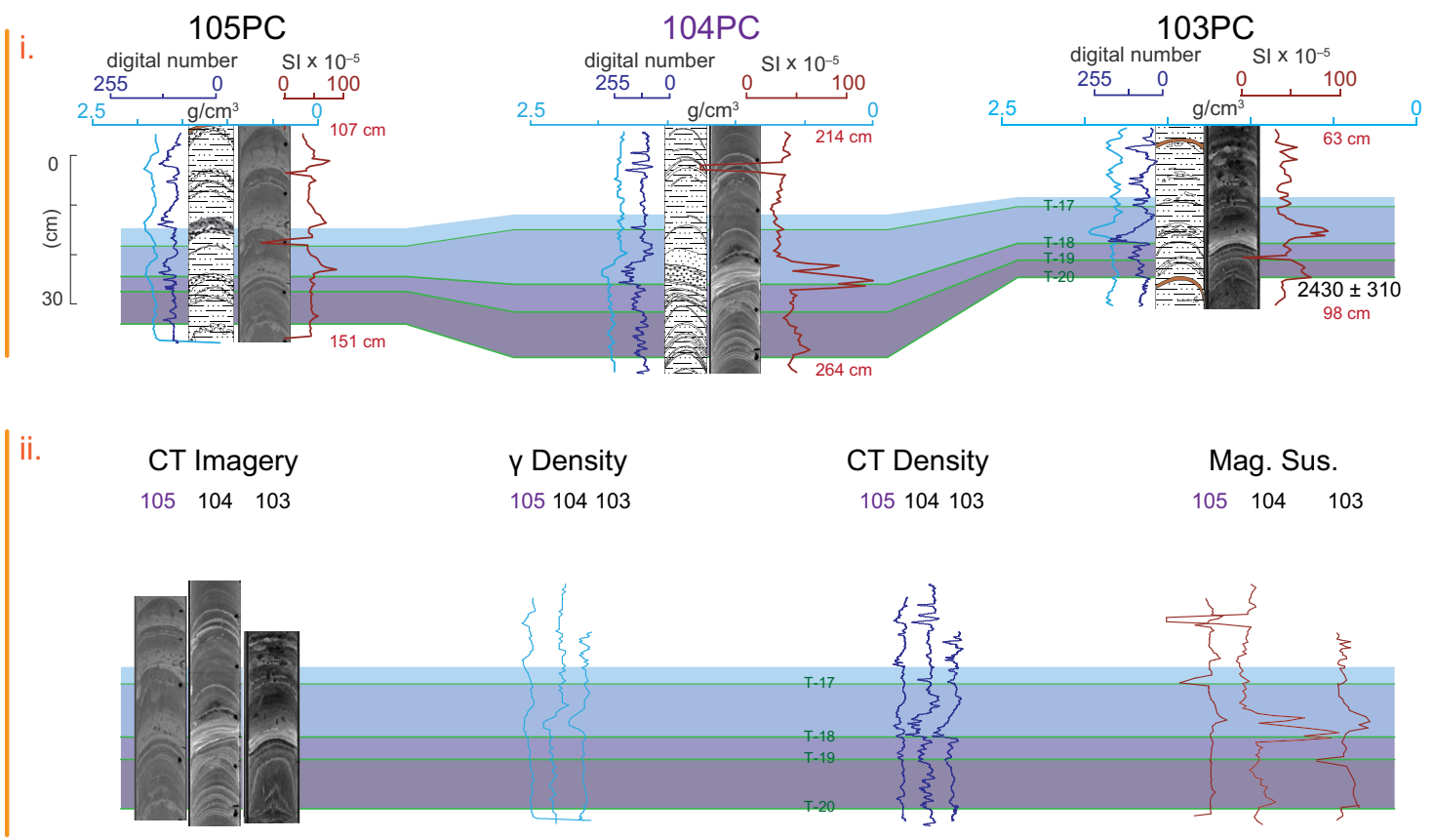

Figure 9 (*continued*). (C) Turbidites T-17–T-20 are correlated between cores 105PC, 104PC, and 103PC. Core data are flattened to core 105PC.

bioturbated in core 103PC, and thus have weak geophysical property trends; those correlations are shown with less confidence. The sequences of T-18–T-20 also have matching and superposed geophysical fingerprints in cores 103PC and 104PC, especially noticeable in the PMS data. The sequence of T-18–T-20 in cores 103PC and 104PC also shares a common densostratigraphic series visible in the CT imagery and the CT density geophysical data. This T-18–T-20 sequence demonstrates the multiproxy correlation method, using not only the flattening of core geophysical data for individual turbidites, but the entire stratigraphic sequence as well. In addition to the T-18–T-20 sequence, T-21 has a higher mass than the overlying and underlying turbidites and in some examples a distinctive simple structure, providing an anchor for those other correlations. Cores 103PC and 104PC have very distinct PMS and CT density trends for T-27, which provide support for this correlation. There are more turbidites that appear to correlate between cores 104 and 103 than observed in other cores, but we do not assign these turbidites T numbers due to their limited aerial extent. Due to the closely spaced laminations and lack of hemipelagic sediment in core 104PC, there are few ^{14}C ages in the lower section. This makes it difficult to temporally constrain these correlations independently.

We compare cores 103 and 95PC, 96, and 97MC (Figs. 3 and 8; Supplemental File S3). Cores 95PC and 96, 97MC are located in two small (~50 km^2) enclosed basins, within a larger slope basin that partially drains to the south over a 70-m-high sill at 3350 m water depth (Fig. 6A). Core 95PC contains strata that appear correlated with strata in core 96, but the sediments in core 95PC are quite disturbed, so we leave that core out of the correlation figures and later discussion. The overlap in stratigraphy between 96PC and 96TC and 97MC was presented here (see results discussion). Based on the downcore trend in

Geosphere, published online on 12 November 2015 as doi:10.1130/GES01066.1

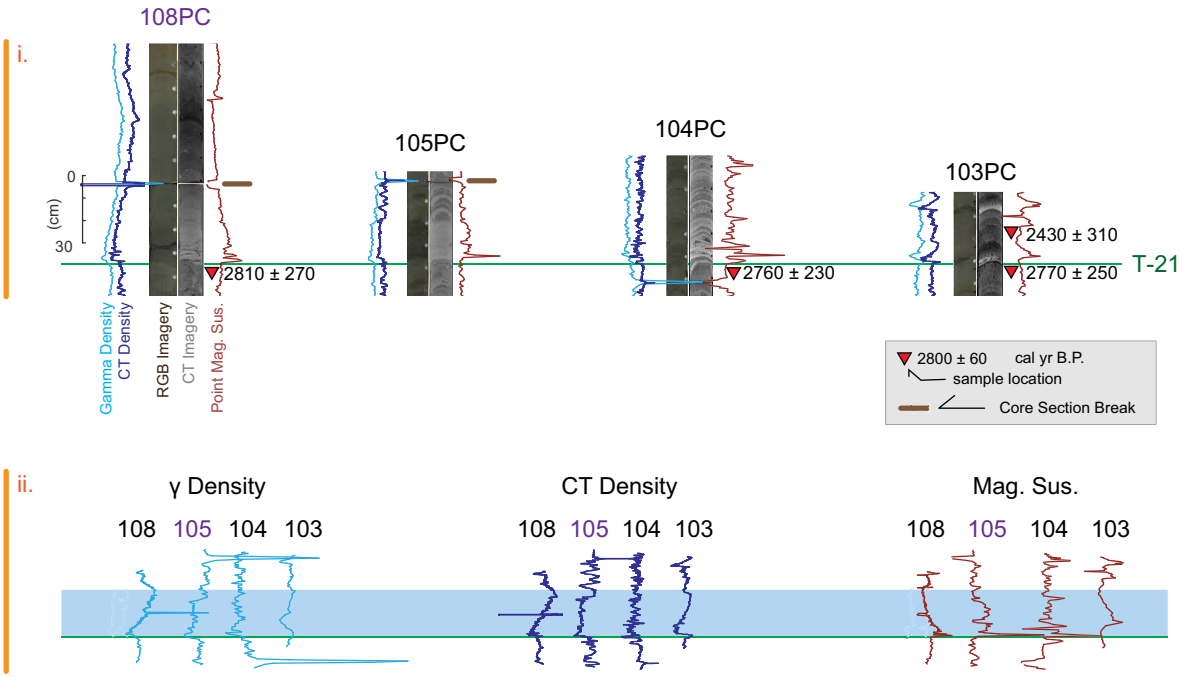

Figure 10. Turbidite T-21 is correlated between cores 108PC, 105PC, 104PC, and 103PC using the same configuration as Figure 8. This sedimentary sequence has 2 panels with different core configurations. Ages are in cal yr B.P. (i) Vertically true scale of core data [left to right: gamma density, CT (computed tomographic X-ray) density, RGB (red-green-blue) imagery, CT imagery, point magnetic susceptibility (Mag Sus), and ^{14}C ages with 95% error]. (ii) Geophysical property data are flattened (scaled vertically) to stratigraphic contacts. Core data are flattened to core 105PC. The green correlation tie line designates the base of T-21.

^{210}Pb data, the ~5-cm-thick sediment underlying T-1 in core 96TC is likely from the seafloor, and therefore likely is repeated section, probably containing sediment from the surficial mixed layer. Based on this observation, it is possible that the base of T-1 is not in core 96TC. Turbidites in core 96PC are generally thicker and less bioturbated than those in core 103. In addition to the high confidence correlations presented earlier in Figure 9, the turbidites underlying T-11 in core 96PC are more bioturbated, thinner, and finer in texture than most overlying turbidites, contributing to the lower confidence in our correlations between cores 103 and 96. Because T-18 is not entirely within core 96, this correlation is less certain and untestable.

Trench cores 98 and 94PC are the southernmost trench cores in the 2004 earthquake slip region (Fig. 7). Core 98 is west of a gently sloping 0.5-km-high landward-verging anticline, possibly isolating this core from direct sedimentation from higher relief bathymetry to the east. Core 94PC is located off axis from the trench and downslope of several potential landslide source areas in the form of submarine canyons, base of slope apron fan channels, and local landslide amphitheater complexes (Patton et al., 2013a). In the trench, cores 98PC and 98TC overlap completely and neither sampled the sediment-water interface, evidenced by core 99MC, which has the uppermost turbidite we interpret to be T-1 (Supplemental File S3). Most turbidites in core 98OC–98TC are muddy with low dynamic range in particle density and size. This, coupled with the lack of ^{14}C ages, leads to less confident correlations. At the southern limit of the 2004 earthquake slip region, core 94PC sampled the uppermost turbidite that we interpret as T-1. Core 94PC is highly deformed and lacks ^{14}C age control, so these correlations are also less certain (Supplemental File S3). However, the very young soupy surface turbidite, the lack of surface oxidation, and ^{210}Pb age data are compatible with our interpretation that this is likely the 2004 turbidite.

Farther south, in cores 93TC and 88TC, we make moderately confident correlations with the turbidite underlying the uppermost turbidite in these cores. We correlate these second turbidites in these two cores to T-1 found in the cores to the north (Supplemental File S3). The geophysical property trends are almost identical between these cores and are very similar to the geophysical fingerprint of T-1 in core 96PC; therefore the uppermost turbidite in 93TC and 88TC is likely younger than the probable 2004 deposit We tentatively interpret the uppermost turbidite in cores 93TC and 88TC to be the result of the 2005 M 8.7 earthquake (Hsu et al., 2006; Briggs et al., 2006).

Radiocarbon Age Results

Here we present the results of our age model based calibrations for deposits older than T-1 (raw calibrated ages are in Table 2). Bayesian modeling of radiocarbon calibrations takes into account varying degrees of stratigraphic

Geosphere, published online on 12 November 2015 as doi:10.1130/GES01066.1

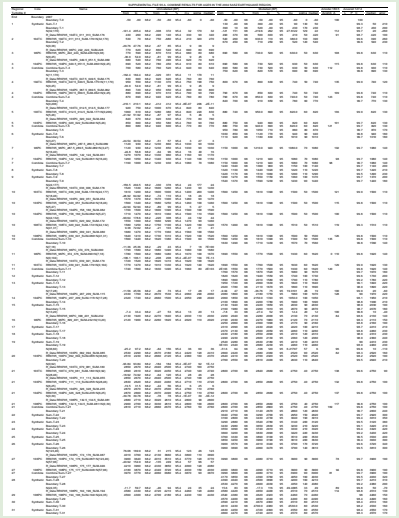

[5]Supplemental File S5. Radiocarbon age modeling. OxCal combinations (Bronk Ramsey, 2009a) and single ages used to provide age control for timing of turbidite deposition (Fig. 3). Single ages are calibrated as discussed in text and Supplemental File S2. (A) OxCal output for the regional combine analysis. Age results in this table are direct results from the OxCal code in Supplemental File S2. (B) OxCal output for the singe core P_Sequence analyses. Please visit http://dx.doi.org/10.1130/GES01066.S5 or the full-text article on www.gsapubs.org to view Supplemental File S5.

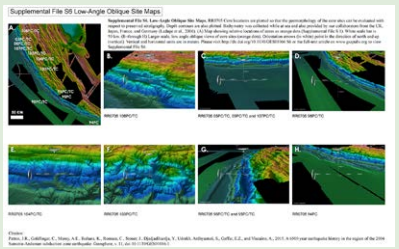

[6]Supplemental File S6. Low-angle oblique site maps. RR0705 core locations are plotted so that the geomorphology of the core sites can be evaluated with respect to preserved stratigraphy. Depth contours are also plotted. Bathymetry was collected while at sea and also provided by our collaborators from the UK, Japan, France, and Germany (Ladage et al., 2006). (A) Map showing relative locations of cores as orange dots (Supplemental File S1). White scale bar is 50 km. (B–H) Larger scale, low-angle oblique views of core sites (orange dots). Orientation arrows (in white) point in the direction of north and up (vertical). Vertical and horizontal units are in meters. Please visit http://dx.doi.org/10.1130/GES01066.S6 or the full-text article on www.gsapubs.org to view Supplemental File S6.

information as prior constraints for these calibrations. We utilize P_Sequence age models for within-core age calibrations and present these results in Figure 8 and Supplemental File S5[5]. We use Sequence age models for the region-wide comparison of ages between cores, and summarize these age model results in Table 5. All ages initially considered in our model are in Table 5A. Ages that we consider in our final age model are in Table 5B, with selection criteria discussed here. We present the P_Sequence age model results in Table 5C.

Where multiple ^{14}C ages exist for correlated turbidites, and where ages do not suggest erosion or other problems, we test whether they are compatible with our stratigraphic correlation model by using the Combine function in OxCal software (Bronk Ramsey, 2008). Combined ages for turbidites T-3, T-4, T-5, T-7, T-10, T-11, T-21, and T-27 are computed with the combination of 2–5 ages (Table 5B; Supplemental File S5). OxCal takes the laboratory ages and calculates a pooled mean laboratory age prior to calibration. The result is a probability density function age range, based on the contribution of all combined ages. We evaluate the Combine results using three criteria: a chi-squared test, the OxCal agreement index A_{comb} (>60), and convergence integral C (>95) (Bronk Ramsey, 1995, 2009a, 2009b). The Combine function is normally used with the prior information that the samples come from either the same sample, or from the same horizon (Bronk Ramsey, 2008). Our lithostratigraphic correlations are the basis for interpreting these groups as coming from the same horizon, though with far less certainty than if they were from the same bed in an outcrop. We acknowledge that our combine results may impart a shorter time range of uncertainty than realistic given our inability to quantify erosion, bioturbation, and other departures from a uniform age sequence.

We present the results of our criteria tests for Sequence age model and how we used these criteria to test for and manually remove outlier ages from our age model (Bronk Ramsey, 2009b). Of the results shown in Table 5A, there were no chi-squared or agreement index failures for the P_Sequence age models (Bronk Ramsey, 2009b). The Sequence age model had two failures for the age combinations (Combine function; Table 5A). The Combine for T-33 initially fails the chi-squared test at 5% and with A_{comb} = 56.6%. For the T-33 Combine, we manually removed SUM-050 from the Combine because the Agreement Index A was lower at 44.0%, leaving a single age calibration for the T-33 age estimate. The Combine for T-41 initially fails the chi-squared test at 5% and with A_{comb} = 17.1%. For the T-41 Combine, we manually removed SUM-044 from the Combine because the Agreement Index A was lower at 25.8%, leaving a single age calibration for the T-41 age estimate.

Regional Stratigraphic Correlation Summary

In general, the more certain correlations temporally span 2.8 k.y. (T-1–T-21) in core 108PC, ~2.8 k.y. in core 104PC (T-1–T-21), ~2.8 k.y. in cores 102/103 (T-1–T-21), and 2 k.y. in core 96PC (T-1–T-11; Figs. 3 and 8). These more certain correlations include 6 turbidites in core 108PC, 17 turbidites in core 104PC, 17 turbidites in core 103PC, 11 turbidites in core 96PC, 1 turbidite in core 98PC, 1 turbidite in core 94PC, 1 turbidite in core 93TC, and 1 turbidite in core 88TC. When we include less confident correlations, there are 28 turbidites in core 108PC, 21 in core 107TC, 39 in core 105C–105TC, 37 in core 104PC, 43 in core 103PC, and 18 in core 96PC. Based on the lowermost correlated turbidite in any given core, we find that cores 108, 107TC, 105, 104, 103, 102MC, and 96 contain 65%, 49%, 91%, 86%, 100%, and 42% of these correlated turbidites, respectively.

We have tested potential correlations between sites within the 2004 rupture zone iteratively using the available age control, patterns of variability in the overall sequence of turbidites, and detailed comparisons for intrasite and intersite similarity between individual turbidites. We find that in some cases, individual turbidite characteristics are similar enough, within and between sites, that they may be used to track individual turbidites in a sequence. The stratigraphic sequences with the most unique fingerprints (Goldfinger et al., 2013a) carry the strongest correlative weight and act as anchors for our correlations (Fig. 8), supported by ^{14}C age control. We designate turbidites with numbers corresponding to their order down from the seafloor. Turbidites are assigned T-numbers that designate these deposits to be regionally correlative, counting down from the uppermost turbidite (T-1). Turbidites that have sediment with low dynamic range (e.g., fine-grained turbidites) and nonunique sedimentary structure (possibly with nonunique geophysical properties) are more difficult to correlate with confidence. Because we cannot correlate these turbidites, we do not include them in this discussion.

DISCUSSION

2004 Turbidite

We found the uppermost turbidites in cores 01GC, 05PC, 26GC, 109MC, 108PC-108TC 107PC, 105TC, 104PC-104TC, 102MC, 99MC, 97MC, 96PC-96TC, 95PC, 94PC, 93TC, 88TC, and 87PC-87TC to be composed of gray sediment with a very high water content (i.e., soupy), particularly at the seabed. These represent 21 discrete examples of the uppermost young bed, of 54 cores and core attempts within the 2004 region. The 2 uppermost turbidites in cores 93, 88, and 87 also share this soupy characteristic. There is no hemipelagic sediment overlying these deposits, and we do not observe oxidation in the uppermost sediment in any of these cores. This deposit, if correlated, spans as much as 500 km and 230 km, in the trench and along the slopes, respectively, and is present in cores with unique and isolated sediment source areas (Figs. 3 and 6; Supplemental Files S1 and S6[6]). Of the remaining 33 cores within the 2004 area, cores 107TC, 105PC, 103PC-103TC, 93PC, and 88PC are missing their tops; cores 98PC-98TC are indeterminate; 03TC-03PC had bioturbated and oxidized tops with no young surface bed; 10GC, 11GC, 12GC, and 13KC were 55 km west of the margin, likely well out of the turbidity current extent; 15GC and 16GC were on the top of the forearc plateau and taken for other purposes. Cores 106PC-106TC are very distal control cores ~170 km west of the margin;

Geosphere, published online on 12 November 2015 as doi:10.1130/GES01066.1

TABLE 5A. RADIOCARBON AGE OXCAL MODELING RESULTS FOR TURBIDITE AGES IN THE 2004 SUMATRA-ANDAMAN SUBDUCTION ZONE EARTHQUAKE REGION

Regional turbidite number	Core number	Sample/combine name*	Unmodeled median age (yr B.P.)†	1σ error (yr)	Modeled median age (yr B.P.)§	1σ error (yr)	Acomb**	A††	Excluded
End	Boundary	2007							
1	Synthetic	Sum-T-1	–	–	50	120	–	–	
2	104TC	RR0705_104TC_011_013_SUM-176+N(32,170)	270	320	370	130	–	–	
3	Combine	Combine Sum-T-3	640	60	630	50	111.6	–	
3	104PC	RR0705_104PC_049.5_051.5_SUM-060+N(9,45)	610	80	630	50	–	115.0	
3	96PC	RR0705_96PC_222_224_SUM-228+N(9,38)	680	80	630	50	–	107.6	
4	Combine	Combine Sum-T-4	780	80	740	50	122.9	–	
4	104TC	RR0705_104TC_047.5_049.5_SUM-175+N(11,170)	750	190	740	50	–	135.4	
4	104PC	RR0705_104PC_067.5_069.5_SUM-062+N(9,45)	790	90	740	50	–	108.6	
5	Combine	Combine Sum-T-5	770	80	820	60	120.9	–	
5	103TC	RR0705_103TC_012.5_014.5_SUM-177+N(0,206)	830	220	820	60	–	135.8	
5	103PC	RR0705_103PC_020_022_SUM-084+N(5,46)	760	90	820	60	–	101.3	
6	Synthetic	Sum-T-6	–	–	940	90	–	–	
7	Combine	Combine Sum-T-7	1080	70	1080	70	97.8	–	
7	96PC	RR0705_96PC_287.5_289.5_SUM-089+N(327)	1030	90	1080	70	–	102.2	
7	104PC	RR0705_104PC_122_124_SUM-061+N(16,40)	1150	100	1080	70	–	98.0	
8	Synthetic	Sum-T-8	–	–	1220	110	–	–	
9	Synthetic	Sum-T-9	–	–	1370	100	–	–	
10	Combine	Combine Sum-T-10	1500	60	1500	50	134.6	–	
10	103TC	RR0705_103TC_036_038_SUM-178+N(24,177)	1400	200	1510	50	–	121.0	
10	103PC	RR0705_103PC_049_051_SUM-054+N(18,46)	1460	100	1500	50	–	114.9	
10	104PC	RR0705_104PC_158_160_SUM-082+N(5,47)	1590	110	1500	50	–	99.8	
10	108TC	RR0705_108TC_020_022_SUM-172+N(44,132)	1420	160	1500	50	–	118.8	
10	108PC	RR0705_108PC_039_041_SUM-080+N(41,31)	1520	100	1500	50	–	125.5	
11	Combine	Combine Sum-T-11	1650	80	1620	60	120.3	–	
11	96PC	RR0705_96PC_374_376_SUM-090+N(7,18)	1670	100	1620	60	–	109.4	
11	103TC	RR0705_103TC_039_041_SUM-179+N(0,104)	1620	140	1620	60	–	129.5	
12	Synthetic	Sum-T-12	–	–	1720	90	–	–	
13	Synthetic	Sum-T-13	–	–	1820	100	–	–	
14	104PC	RR0705_104PC_207_209_SUM-115+N(17,28)	2040	290	1920	90	–	–	
15	Synthetic	Sum-T-15	–	–	2000	80	–	–	
16	96PC	RR0705_96PC_399_401_SUM-232+N(1320)	2020	110	2070	60	–	–	
17	Synthetic	Sum-T-17	–	–	2160	90	–	–	
18	Synthetic	Sum-T-18	–	–	2260	110	–	–	
19	Synthetic	Sum-T-19	–	–	2350	110	–	–	
20	103PC	RR0705_103PC_092_094_SUM-085+N(36,60)	2370	130	2460	90	–	–	
21	Combine	Combine Sum-T-21	2760	50	2750	40	168.7	–	
21	103TC	RR0705_103TC_079_081_SUM-180+N(0,92)	2740	140	2750	40	–	137.3	
21	103PC	RR0705_103PC_111_113_SUM-055+N(28,46)	2720	110	2750	40	–	131.5	
21	104PC	RR0705_104PC_326_328_SUM-235+N(6,25)	2760	110	2750	40	–	136.3	
21	108PC	RR0705_108PC_132.5_134.5_SUM-081+N(0,39)	2800	100	2750	40	–	116.4	
22	Synthetic	Sum-T-22	–	–	2920	150	–	–	
23	Synthetic	Sum-T-23	–	–	3120	200	–	–	
24	Synthetic	Sum-T-24	–	–	3320	210	–	–	
25	Synthetic	Sum-T-25	–	–	3530	200	–	–	
26	108PC	Sum-T-26	–	–	3720	170	–	–	

(*continued*)

Geosphere, published online on 12 November 2015 as doi:10.1130/GES01066.1

TABLE 5A. RADIOCARBON AGE OXCAL MODELING RESULTS FOR TURBIDITE AGES IN THE 2004 SUMATRA-ANDAMAN SUBDUCTION ZONE EARTHQUAKE REGION (*continued*)

Regional turbidite number	Core number	Sample/combine name*	Unmodeled median age (yr B.P.)†	1σ error (yr)	Modeled median age (yr B.P.)§	1σ error (yr)	Acomb**	A††	Excluded
27	Combine	Combine Sum-T-27	3870	90	3900	90	80.5		
27	103PC	RR0705_103PC_174_176_SUM-087+N(123,46)	3770	120	3900	90	–	78–.7	
27	108PC	RR0705_108PC_175_177_SUM-046+N(57,96)	4030	150	3900	90	–	93.2	
28	Synthetic	Sum-T-28	–	–	4190	150	–	–	
29	108PC	RR0705_108PC_194_196_SUM-194+N(24,35)	4430	130	4440	60	–	–	
30	108PC	Sum-T-30	–	–	4510	70	–	–	
31	Synthetic	Sum-T-31	–	–	4570	80	–	–	
32	Synthetic	Sum-T-32	–	–	4630	80	–	–	
33	Combine	Combine Sum-T-33	4650	90	4690	70	56.6	–	
33	103PC	RR0705_103PC_209_211_SUM-050+N(3,31)	4480	120	4690	70	–	44.0	
33	108PC	RR0705_108PC_212.5_214.5_SUM-045+N(37,27)	4790	120	4690	70	–	89.8	yes
34	Synthetic	Sum-T-34	–	–	4770	90	–	–	
35	Synthetic	Sum-T-35	–	–	4840	100	–	–	
36	Synthetic	Sum-T-36	–	–	4930	100	–	–	
37	Synthetic	Sum-T-37	–	–	5010	100	–	–	
38	Synthetic	Sum-T-38	–	–	5090	90	–	–	
39	108PC	RR0705_108PC_257_259_SUM-042+N(44,23)	5070	120	5190	60	–	–	
40	103PC	RR0705_103PC_300.5_302.5_SUM-053+N(0,23)	5710	90	5760	70	–	–	
41	Combine	Combine Sum-T-41	6160	70	6160	70	17.1	–	
41	103PC	RR0705_103PC_324_326_SUM-224+N(17,29)	5940	110	6160	70	–	30.9	
41	108PC	RR0705_108PC_290.5_292.5_SUM-044+N(15,26)	6340	90	6160	70	–	25.8	yes
42	103PC	RR0705_103PC_383_385_SUM-253+N(13,22)	6410	90	6430	60	–	–	
43	108PC	RR0705_108PC_312.5_314.5_SUM-043+N(47,39)	6480	100	6560	60	–	–	
Start	Boundary	Boundary Start	9950	–	9950	–	–	100.0	

Note: dashes indicate no data.
*Sample names that are indented are the ages included in the combine function, named above them.
†Calibrated age and errors reported to 1 standard deviation and are reported in calendar years. Calibrated age ranges before A. D. 1950 according to Stuiver and Reimer (1998) calculated using marine reservoir correction and regional delta R offset (ΔR = 16 ± 78). These ages are the result of simple calibrations, prior to any statistical manipulation during the Combine analysis (i.e., unmodeled; see text). Synthetic age estimates are designated with sample names Sum-T-# and have no unmodeled ages.
§These are the results of calibration with the Combine function. Years are reported as in the unmodeled results.
**Agreement Index Acomb.
††Agreement Index A.

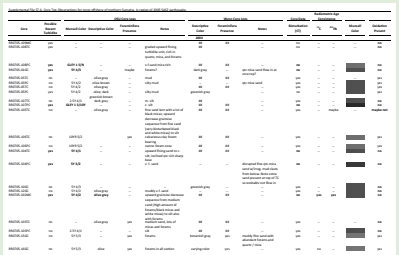

[7]Supplemental File S7. Core top observations. Core top observations for cores offshore of northern Sumatra are presented. (A) Cores in the 2004 Sumatra-Andaman subduction zone (SASZ) earthquake region. (B) Cores in the 2005 SASZ earthquake region. Please visit http://dx.doi.org/10.1130/GES01066.S7 or the full-text article on www.gsapubs.org to view Supplemental File S7.

cores 19GC, 20GC, and 21GC were all 22 km west of the margin, outside axial the axial trench channel system; cores 94TC, 02GC, 03GC, 04KC, 07MC, 08GC, 09GC, 14GC, and 17KC had no recovery for various reasons. The lack of the 2004 turbidite is well explained for most these cores. Only cores 18GC, 101GC, 100MC were in a seemingly suitable mid-slope basin, yet lacked a young surface turbidite. On closer inspection, however, these cores are located in a wide flat basin of the type we have found unsuitable for unchannelized turbidity current deposition (Patton et al., 2007; Goldfinger et al., 2014a; see Supplemental File S7[7] for supporting core top data).

Oxidation of sediment provides a qualitative assessment of relative age and oxidation of the uppermost sediment is rapid in most settings. Turbidite tails typically have relatively high organic content compared to hemipelagic and pelagic sediments (e.g., Cowie et al., 1998), reducing the time constant for surface oxidation. In several studies, the response time for oxidation of the upper sediments has been quantified. Hammond et al. (1996) modeled the reactions responsible for O_2 and NO_3 profiles in the central equatorial Pacific. The uppermost sediments were assumed to be mixed at rates described by ^{234}Th and ^{210}Pb profiles. Hammond et al. (1996) described a dominant and more labile fraction that oxidized in days to months, and a less labile fraction that oxidized in decades. Sayles et al. (2001) also found response time to be short at 0.3–1.6 yr for high flux sites, and 5–80 yr for very low flux sites in the Southern Ocean. Smith (1987) found response times of 0.1–0.2 yr for high flux sites and 1–5 yr for low flux sites, in the eastern and central North Pacific between California and Hawaii. While detailed data on oxidation rates do not exist for Sumatra, we infer from these studies that oxidation would most likely be apparent if the uppermost turbidite were

Geosphere, published online on 12 November 2015 as doi:10.1130/GES01066.1

TABLE 5B. RADIOCARBON AGE OXCAL MODELING RESULTS FOR TURBIDITE AGES IN THE 2004 SUMATRA-ANDAMAN SUBDUCTION ZONE EARTHQUAKE REGION

Regional turbidite number	Core number	Sample-combine name*	Unmodeled median age (yr B.P.)†	1σ error (yr)	Modeled median age (yr B.P.)§	1σ error (yr)	Acomb**	A††
End	Boundary	2007	–	–	–	–	–	–
1	Synthetic	Sum-T-1	–	–	50	130	–	–
2	104TC	RR0705_104TC_011_013_SUM-176+N(32170)	270	320	390	130	–	–
3	Combine	Combine Sum-T-3	640	60	630	50	111.6	–
3	96PC	RR0705_96PC_222_224_SUM-228+N(9,38)	680	80	630	50	–	108.2
3	104PC	RR0705_104PC_049.5_051.5_SUM-060+N(9,45)	610	80	630	50	–	114.8
4	Combine	Combine Sum-T-4	780	80	740	50	122.9	–
4	104TC	RR0705_104TC_047.5_049.5_SUM-175+N(11170)	750	190	740	50	–	135.4
4	104PC	RR0705_104PC_067.5_069.5_SUM-062+N(9,45)	790	90	740	50	–	108.5
5	Combine	Combine Sum-T-5	770	80	820	60	120.9	–
5	103TC	RR0705_103TC_012.5_014.5_SUM-177+N(0,206)	830	220	820	60	–	135.8
5	103PC	RR0705_103PC_020_022_SUM-084+N(5,46)	760	90	820	60	–	101.4
6	Synthetic	Sum-T-6	–	–	940	90	–	–
7	Combine	Combine Sum-T-7	1080	70	1080	70	9 7.8	–
7	96PC	RR0705_96PC_287.5_289.5_SUM-089+N(327)	1030	90	1080	70	–	102.1
7	104PC	RR0705_104PC_122_124_SUM-061+N(16,40)	1150	100	1080	70	–	98.0
8	Synthetic	Sum-T-8	–	–	1220	110	–	–
9	Synthetic	Sum-T-9	–	–	1370	100	–	–
10	Combine	Combine Sum-T-10	1500	60	1500	50	134.6	–
10	103TC	RR0705_103TC_036_038_SUM-178+N(24,177)	1400	200	1500	50	–	120.8
10	103PC	RR0705_103PC_049_051_SUM-054+N(18,46)	1460	100	1500	50	–	114.5
10	104PC	RR0705_104PC_158_160_SUM-082+N(5,47)	1590	110	1500	50	–	100.1
10	108TC	RR0705_108TC_020_022_SUM-172+N(44,132)	1420	160	1510	50	–	118.6
10	108PC	RR0705_108PC_039_041_SUM-080+N(4131)	1520	100	1500	50	–	125.5
11	Combine	Combine Sum-T-11	1650	80	1620	60	120.3	–
11	96PC	RR0705_96PC_374_376_SUM-090+N(7,18)	1670	100	1620	60	–	110.2
11	103TC	RR0705_103TC_039_041_SUM-179+N(0,104)	1620	140	1620	60	–	129.0
12	Synthetic	Sum-T-12	–	–	1730	100	–	–
13	Synthetic	Sum-T-13	–	–	1840	110	–	–
14	104PC	RR0705_104PC_207_209_SUM-115+N(17,28)	2040	290	1950	100	–	–
15	Synthetic	Sum-T-15	–	–	2030	90	–	–
16	96PC	RR0705_96PC_399_401_SUM-232+N(1320)	2020	110	2110	70	–	–
17	Synthetic	Sum-T-17	–	–	2210	100	–	–
18	Synthetic	Sum-T-18	–	–	2310	120	–	–
19	Synthetic	Sum-T-19	–	–	2410	120	–	–
20	103PC	RR0705_103PC_092_094_SUM-085+N(36,60)	2370	130	2520	100	–	–
21	Combine	Combine Sum-T-21	2760	50	2750	40	168.7	–
21	103TC	RR0705_103TC_079_081_SUM-180+N(0,92)	2740	140	2750	40	–	137.5
21	103PC	RR0705_103PC_111_113_SUM-055+N(28,46)	2720	110	2750	40	–	131.5
21	104PC	RR0705_104PC_326_328_SUM-235+N(6,25)	2760	110	2750	40	–	136.8
21	108PC	RR0705_108PC_132.5_134.5_SUM-081+N(0,39)	2800	100	2750	40	–	117.2
22	Synthetic	Sum-T-22	–	–	2920	150	–	–
23	Synthetic	Sum-T-23	–	–	3120	200	–	–
24	Synthetic	Sum-T-24	–	–	3320	210	–	–
25	Synthetic	Sum-T-25	–	–	3530	200	–	–
26	Synthetic	Sum-T-26	–	–	3720	170	–	–

(*continued*)

Geosphere, published online on 12 November 2015 as doi:10.1130/GES01066.1

TABLE 5B. RADIOCARBON AGE OXCAL MODELING RESULTS FOR TURBIDITE AGES IN THE 2004 SUMATRA-ANDAMAN SUBDUCTION ZONE EARTHQUAKE REGION (*continued*)

Regional turbidite number	Core number	Sample-combine name*	Unmodeled median age (yr B.P.)†	1σ error (yr)	Modeled median age (yr B.P.)§	1σ error (yr)	Acomb**	A††
27	Combine	Combine Sum-T-27	3870	90	3900	90	80.5	–
27	103PC	RR0705_103PC_174_176_SUM-087+N(12346)	3770	120	3900	90	–	–
27	108PC	RR0705_108PC_175_177_SUM-046+N(57,96)	4030	150	3900	90	–	–
28	Synthetic	Sum-T-28	–	–	4210	160	–	–
29	108PC	RR0705_108PC_194_196_SUM-194+N(24,35)	4430	130	4460	70	–	–
30	Synthetic	Sum-T-30	–	–	4510	80	–	–
31	Synthetic	Sum-T-31	–	–	4550	80	–	–
32	Synthetic	Sum-T-32	–	–	4590	80	–	–
33	103PC	RR0705_103PC_209_211_SUM-050+N(331)	4480	120	4630	80	–	–
34	Synthetic	Sum-T-34	–	–	4720	110	–	–
35	Synthetic	Sum-T-35	–	–	4810	120	–	–
36	Synthetic	Sum-T-36	–	–	4910	120	–	–
37	Synthetic	Sum-T-37	–	–	5010	120	–	–
38	Synthetic	Sum-T-38	–	–	5110	100	–	–
39	108PC	RR0705_108PC_257_259_SUM-042+N(44,23)	5070	120	5220	70	–	–
40	103PC	RR0705_103PC_300.5_302.5_SUM-053+N(0,23)	5710	90	5790	70	–	–
41	103PC	RR0705_103PC_324_326_SUM-224+N(17,29)	5940	110	6030	80	–	–
42	103PC	RR0705_103PC_383_385_SUM-253+N(1322)	6410	90	6470	60	–	–
43	108PC	RR0705_108PC_312.5_314.5_SUM-043+N(47,39)	6480	100	6600	70	–	–
Start	Boundary	Boundary Start	9950	–	9950	–	–	–

Note: dashes indicate no data.
*Sample names that are indented are the ages included in the combine function, named above them.
†Calibrated age and errors reported to 1 standard deviation and are reported in calendar years. Calibrated age ranges before A.D. 1950 according to Stuiver and Reimer (1998) calculated using marine reservoir correction and regional ΔR offset (ΔR = 16 ± 78). These ages are the result of simple calibrations, prior to any statistical manipulation during the Combine analysis (i.e., unmodeled). Synthetic age estimates are designated with sample names Sum-T-# and have no unmodeled ages.
§Results of calibration with the Combine function (see text). Years are reported as in the unmodeled results.
**Agreement Index Acomb.
††Agreement Index A.

older than ~5 yr at the time of collection, which was ~2.6 yr after the 2004 earthquake. Oxidation therefore may constrain the timing of emplacement more tightly than other methods, and suggests an age for the surface turbidite within a few years of collection.

Using the available constraints, our P_Sequence ^{14}C age model for the uppermost turbidite in core 96PC suggests a median age of 60 ± 150 cal yr B.P. (Table 3). The ^{210}Pb age data in cores 96 and 102 are compatible with an age within the past few decades at most, as are the radiocarbon ages (Figs. 7 and 8). We therefore interpret this young turbidite as likely the result of the 2004 earthquake, with the evidence spanning a distance of ~230 km along strike, a region of at least 10,500 km^2 (Fig. 3).

There was no detectable ^{137}Cs in cores 94PC and 105TC due to at least one of two possible reasons (Table 4): either there was insufficient ^{137}Cs in this region of the Indian Ocean to detect given the gamma counting methods (Wheatcroft and Sommerfield, 2005) because complete or nearly complete decay had occurred, or the sediment was deposited prior to 1952. Based on measurements from seawater (Alam et al., 1996), there may have been ^{137}Cs in the seawater. In this case, the ^{137}Cs may not have deposited in sufficient concentration at the seafloor. If sedimentation rates are sufficiently low, and or there was sufficient erosion, we would not expect to find ^{137}Cs activity in these cores.

Site conditions play an important role in proximal sites such as those in this study. Of all cores, core 96PC has the most expanded section of what we interpret to be the 2004 seismoturbidite. The expanded stratigraphic section is possibly due to the core site, found in the center of a 40-km-long by 7-km-wide slope basin that probably does not drain completely, possibly causing the sediment to pond (Fig. 6A). Underlying turbidites are also thicker than interpreted correlatives in other cores, suggesting that the reason for thicker deposits is site related. For example, T-6 and T-7 are 23 cm and 30 cm thick in core 96PC, but only 6 and 3 cm thick in 103PC. We use the entire sedimentary section above the oldest ^{14}C age in each core to calculate the overall sedimentation rate (Table 6). The overall sedimentation rate for the past 2 k.y. in core

Geosphere, published online on 12 November 2015 as doi:10.1130/GES01066.1

TABLE 5C. P_SEQUENCE OXCAL MODELING RESULTS FOR TURBIDITE AGES IN THE 2004 SUMATRA-ANDAMAN SUBDUCTION ZONE EARTHQUAKE REGION

Core number	Regional turbidite number	Sample name*	P_Sequence median age (yr B.P.)†	95.4% error (yr)
108PC	10	R_Date("RR0705_108PC_039_041_SUM-080", 2015, 15) + N(41,31) { z = 0.221; }	1550	270
108PC	21	R_Date("RR0705_108PC_132.5_134.5_SUM-081", 3035, 15) + N(0,39) { z = 0.523; }	2810	270
108PC	25	R_Date("RR0705_108PC_156_158_SUM-083", 3500, 15) + N(77,43) { z = 0.523; }	3320	300
108PC	26	R_Date("RR0705_108PC_175_177_SUM-046", 4070, 15) + N(57,96) { z = 0.605; }	4050	470
108PC	27	R_Date("RR0705_108PC_194_196_SUM-194", 4340, 20) + N(24,35) { z = 0.721; }	4470	320
108PC	28	R_Date("RR0705_108PC_212.5_214.5_SUM-045", 4625, 20) + N(37,27) { z = 0.812; }	4820	280
108PC	34	R_Date("RR0705_108PC_257_259_SUM-042", 4840, 20) + N(44,23) { z = 0.892; }	5130	300
108PC	36	R_Date("RR0705_108PC_290.5_292.5_SUM-044", 5950, 20) + N(15,26) { z = 1.043; }	6350	230
108PC	37	R_Date("RR0705_108PC_312.5_314.5_SUM-043", 6115, 20) + N(47,39) { z = 1.077; }	6520	270
108TC	10	R_Date("RR0705_108TC_020_022_SUM-172", 1930, 20) + N(44,132) { z = 0.054; }	1380	540
104PC	3	R_Date("RR0705_104PC_049.5_051.5_SUM-060", 1065, 20) + N(9,45) { z = 0.058; }	620	180
104PC	4	R_Date("RR0705_104PC_067.5_069.5_SUM-062", 1265, 15) + N(9,45) { z = 0.09; }	790	200
104PC	7	R_Date("RR0705_104PC_122_124_SUM-061", 1630, 45) + N(16,40) { z = 0.11; }	1160	220
104PC	10	R_Date("RR0705_104PC_158_160_SUM-082", 2040, 20) + N(5,47) { z = 0.17; };	1590	240
104PC	14	R_Date("RR0705_104PC_207_209_SUM-115", 2420, 220) + N(17,28) { z = 0.234; }	2070	530
104PC	21	R_Date("RR0705_104PC_326_328_SUM-235", 3000, 35) + N(6,25) { z = 0.416; }	2760	230
104TC	2	R_Date("RR0705_104TC_011_013_SUM-176", 705, 20) + N(32,170) { z = 0.007; }	320	340
104TC	4	R_Date("RR0705_104TC_047.5_049.5_SUM-175", 1220, 20) + N(11,170) { z = 0.022; }	770	360
103PC	4	R_Date("RR0705_103PC_020_022_SUM-084", 1225, 20) + N(5,46) { z = 0.122; }	810	240
103PC	10	R_Date("RR0705_103PC_049_051_SUM-054", 1940, 25) + N(18,46) { z = 0.186; }	1520	260
103PC	20	R_Date("RR0705_103PC_092_094_SUM-085", 2705, 15) + N(36,60) { z = 0.254; }	2430	310
103PC	21	R_Date("RR0705_103PC_111_113_SUM-055", 2985, 20) + N(28,46) { z = 0.282; }	2770	250
103PC	27	R_Date("RR0705_103PC_174_176_SUM-087", 3925, 20) + N(123,46) { z = 0.458; }	3840	280
103PC	29	R_Date("RR0705_103PC_209_211_SUM-050", 4360, 20) + N(3,31) { z = 0.523; }	4550	260
103PC	35	R_Date("RR0705_103PC_277_279_SUM-052", 5095, 20) + N(0,40) { z = 0.734; }	5500	240
103PC	36	R_Date("RR0705_103PC_324_326_SUM-224", 5575, 25) + N(17,29) { z = 0.827; }	6000	220
103PC	37	R_Date("RR0705_103PC_383_385_SUM-253", 6020, 25) + N(13,22) { z = 0.874; }	6470	200
103TC	4	R_Date("RR0705_103TC_012.5_014.5_SUM-177", 1310, 20) + N(0,206) { z = 0.018; }	850	180
103TC	11	R_Date("RR0705_103TC_036_038_SUM-178", 1890, 20) + N(24,177) { z = 0.038; }	1440	190
103TC	12	R_Date("RR0705_103TC_039_041_SUM-179", 2065, 20) + N(0,104) { z = 0.053; }	1650	290
103TC	21	R_Date("RR0705_103TC_079_081_SUM-180", 2985, 20) + N(0,92) { z = 0.098; }	2760	260
102MC	1	R_Date("RR0705_102MC_065_075_SUM-249", 455, 20) + N(5,46) { z = 0.596; }	50	60
96PC	1	R_Date("RR0705_96PC_206_208_SUM-227", 480, 15) + N(71,123) { z = 0.227; }	60	150
96PC	3	R_Date("RR0705_96PC_222_224_SUM-228", 1145, 15) + N(9,38) { z = 0.02; }	710	120
96PC	7	R_Date("RR0705_96PC_287.5_289.5_SUM-089", 1490, 15) + N(3,27) { z = 0.128; }	1070	130
96PC	11	R_Date("RR0705_96PC_374_376_SUM-090", 2115, 20) + N(7,18) { z = 0.267; }	1730	140
96PC	16	R_Date("RR0705_96PC_399_401_SUM-232", 2410, 20) + N(13,20) { z = 0.371; }	2070	150

*Sample names include the lab age and error, the gap in years and error (N), and the depth term (z).
†Calibrated age and errors reported to 95.4% error and are reported in calendar years. Calibrated age ranges before A. D. 1950 (B.P.) according to Stuiver and Reimer (1998) calculated using marine reservoir correction and regional ΔR offset (ΔR = 16 ± 78). These ages are the result of P_Sequence age modeling (see text).

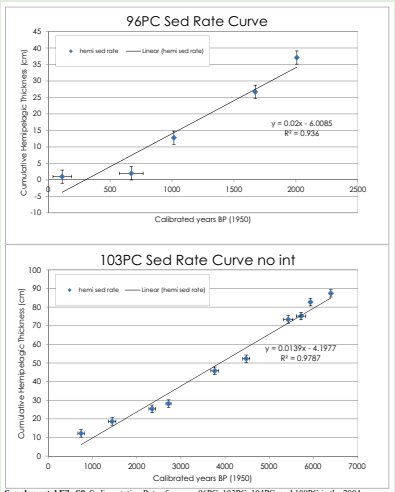

Supplemental File S8. Sedimentation Rates for cores 96PC, 103PC, 104PC, and 108PC in the 2004 Sumatra Andaman subduction zone (SASZ) earthquake region. Please visit http://dx.doi.org/10.1130/GES01066.S8 or the full-text article on www.gsapubs.org to view Supplemental File S8
Citation: Patton, J.R., Goldfinger, C., Morey, A.E., Ikehara, K., Romsos, C., Stoner, J., Djadjadihardja, Y., Udrekh, Ardhyastuti, S., Gaffar, E.Z., and Viscaino, A., 2015, A 6500 year earthquake history in the region of the 2004 Sumatra-Andaman subduction zone earthquake: Geosphere, v. 11, doi:10.1130/GES01066.1.

[8]Supplemental File S8. Sedimentation rates for cores 96PC, 103PC, 104PC, and 108PC in the 2004 Sumatra-Andaman subduction zone (SASZ) earthquake region. Please visit http://dx.doi.org/10.1130/GES01066.S8 or the full-text article on www.gsapubs.org to view Supplemental File S8.

96PC is 1.93 ± 0.09 mm/yr, 0.59 ± 0.03 mm/yr in core 103PC (minimum because the 2004 deposit is absent in this core), 1.04 ± 0.03 mm/yr in core 104PC, and 0.46 ± 0.07 mm/yr in core 108PC (minimum because while the base is present the uppermost portion of the possible 2004 deposit is absent). The stratigraphic section in 104PC has an overall sedimentation rate similar to that of 96PC, though the higher rate at the 104 core site (compared to cores 103PC and 108PC) is possibly due to the position at the base of an oversteepened slope (Fig. 3D), although persistently stronger ground motions at this site are also a possibility. Because over the past 2 k.y. the hemipelagic rate varies little along strike (Table 2; Supplemental File S8[8]), the primary source for variation in overall sedimentation rate is likely due to differences in turbidite deposit thicknesses.

Geosphere, published online on 12 November 2015 as doi:10.1130/GES01066.1

TABLE 6. OVERALL SEDIMENTATION RATES

Core	Depth* (cm)	Error	Age†	Error§	Sedimentation rate (mm/yr)	Error#
108	344	1	7520	490	0.46	0.07
104	445	1	4290	530	1.04	0.14
103	380	1	6470	200	0.59	0.03
96	400	1	2070	150	1.93	0.09

*Depth of the deepest age in the core.
†The deepest calibrated age in the core with uncertainty reported to 95.4% error and reported in calendar years. Calibrated age ranges before A.D. 1950 according to Stuiver and Reimer (1998) calculated using marine reservoir correction and regional ΔR offset (ΔR = 16 ± 78).
§95.4% error in calendar years.
#Root mean square error.

Lithostratigraphic Correlation in the SASZ 2004 Region

The correlated framework shown in Figure 8 represents a depositional history of turbidites spanning ~6.5 k.y., with a potential for a longer record based on the seismic reflection results. Our lithostratigraphic correlations are based on correlation criteria, some qualitative (including stratigraphic superposition, geophysical proxy fingerprinting, visual lithostratigraphic descriptions) and some quantitative (relative and absolute ages). When more correlation criteria are satisfied for a given turbidite bed, the confidence in bed correlation increases, and the corresponding tie line is thicker and solid. Radiocarbon age results are plotted for the sediment underlying the correlated turbidites. The map (Fig. 3A) shows the core locations and the isolated source areas for the basin cores.

A key tool to distinguish multipulse turbidites that were deposited as the result of a single earthquake from stacked turbidite beds (Nelson et al., 2012) that were deposited as the result of multiple earthquakes is the presence of hemipelagic sediment and perhaps an oxidized layer between turbidites. Because oxidized layers require more time to develop than the duration of ground shaking, these layers may provide evidence that the multiple turbidites represent multiple seismogenic events. An example of this is found between T-3 and T-4 in core 105. However, it may be possible that these oxidized layers may be absent between seismoturbidites. Here we refer to surface oxidation, not downward-propagating oxidation fronts (e.g., Wilson et al., 1985), which are also found in our cores. A second line of evidence that can distinguish between single single-pulse or single multipulse turbidites from multiple single-pulse or multiple multipulse turbidites is that the particle size and geophysical parameter values return to some background pelagic or hemipelagic value. An example of this is in core 96PC where density values in T-4 decrease upcore and reach a low value that corresponds to an oxidized hemipelagic layer beneath T-3. There is a correlation between oxidized layers and low geophysical parameter values for many of the hemipelagites in core 96PC. In core 103, T-3 and T-4 are muddier (lower sediment dynamic range) and lack oxidation laminae, so these deposits are less confidently correlated. In core 104, T-3 has underlying oxidized laminae, but T-4 does not. Considering these data as a whole, for turbidites T-1–T-4, core 96PC contains the balance of the correlated turbidites and other cores contain at least a subset of these turbidites. We note that some turbidites are absent across some intervals in the 2004 rupture region. For example, T-2, T-4, T-6–T-9, T-11–T-13, and T-15–T-20 may not present in core 108PC (Fig. 8; Supplemental File S3). Likewise, T-1 and T-2 appear to be absent in core 103 (missing top), but appear in core 102MC. These omissions may be due to site conditions, erosion, ability to core the entire stratigraphic section, or rupture characteristics (slip, directivity, duration and energy content of shaking; Kramer and Lindwall, 2004). If this were due to the result of site physiography and source proximity, cores that are more proximal than ideal in most cases would be expected to generate greater variability, as has been observed in Cascadia (Goldfinger et al., 2008, 2012a). The missing top in core 103 is probably the result of overpenetration or erosion of the seafloor while coring, because core 102MC includes an uppermost turbidites that are missing in core 103. The uppermost sediment can sometimes be eroded from the seafloor by the piston core during coring due to the high velocity of the corer compared to trigger cores, multicores, and Kasten cores. Missing section in the trigger (gravity core) can sometimes occur through over penetration and loss of material through the upper valve in the top of the corer. In this case, the uppermost sediment is missing from both the PC and the TC. The missing section in cores 108 and 103 may be the result of differences in turbiditic sedimentation rate (e.g., finer grained and/or thinner bedded turbidites), leading to increased bioturbation in the more finely grained and thin turbidites (Goldfinger et al., 2013b), making the turbidites more difficult to distinguish from background sedimentation. Tapered ground motions, as they diminish with distance from higher slip magnitudes, could also lead to finer grained turbidites. These missing sections may also be due to erosion of previous turbidites during the emplacement of any given overlying turbidite. Natural variability of this type is expected at proximal sites, and is observed in Cascadia (Adams, 1990; Goldfinger et al., 2012a) and elsewhere (Pouderoux et al., 2012). It is also possible, and even likely, that at any single core site we did not sample in the optimal location. Thus, the relatively limited time for survey for each site and the reconnaissance nature of our understanding of local slope processes may have resulted in potentially missing the best depositional area for a given basin or trench area.

T-1–T-11, 15, and T-17– T-21 are well correlated and are best explained by seismic triggering. T-12–T-14, T-16, and T-22–T-43 are less well correlated, but are attributed to a seismogenic trigger due to their spatial extent and the isolation of their respective sediment source areas. Other thinner and less coarse and/or less dense turbidites are even less well correlated. While some of these other turbidites may be explained by a seismogenic trigger, they are not included in our earthquake chronology because of the low confidence for these correlations. Nonetheless, some of these other turbidites may be from foreshocks or aftershocks, or from smaller earthquakes. In the following we discuss the site controls to deposition at our core sites.

Geosphere, published online on 12 November 2015 as doi:10.1130/GES01066.1

Site Effects

We have presented a few of the key correlations within which the post ~6600 yr Holocene turbidite sequences are interpreted as a coherent framework. Refer to Figures 8 and 9 for the following discussion of how correlated turbidites may differ between cores. There are many reasons that might contribute to these differences in structure between turbidites correlated between different cores. Highly bioturbated sediment may alter the geophysical property (changing the shape of the fingerprint) or structural interpretation of the turbidite. Highly deformed sediment and muddy turbidites may not be well correlated if the deposit has a low signal to noise ratio (low dynamic range in density or particle site) because their geophysical property fingerprints are not unique. In addition, there are muddy turbidites that may be the result of forcing factors other than earthquakes.

Autocyclic forcing factors may dominate at one site more than another, where local hydrodynamics may influence sedimentary structure or densostratigraphy. For example, sites that are within channels are more likely to have a larger dynamic range (resulting in larger geophysical peaks) than sites that are on terraces or in overbank settings. Allocyclic forcing factors may be more or less dominant at different sites, where the variations in ground motion and slope stability at the sediment source area control the initial input of sediment to the turbidity current. Subduction zone earthquake ruptures generally have nonuniform slip, leading to variations in seismic moment release through space and time (Barrientos and Ward, 1990; Konca et al., 2007; Moreno et al., 2009, 2011). Ground motions at the seafloor likely relate to these variations in slip (Arias, 1970). The ground motions also attenuate in response to a series of factors, including distance to the slip and crustal or site characteristics (e.g., rheology of underlying seascape; Bilek et al., 2004; Bilek, 2007; Mahani and Atkinson, 2013). One core may be closer to a larger slip region (higher energy release) for one earthquake, but at a greater distance for a different earthquake. The differences in coarsening or fining upward in the T-3–T-4 sequence may be due to either site effects, hydrodynamic pathway effects, or differences in earthquake ground motion (Fig. 9A).

We observe some sites at which the individual deposits and deposit sequences have persistent and similar sedimentary structures unique to that site. For example, cores 104PC and 104TC record what we interpret to be regional turbidites T-1–T-32 by correlation to other sites. In these cores individual turbidite beds are commonly expanded as a sequence of many thin coarse pulses as part of their single turbidite structure. The core location for 104 is at the base of a steep slope, with ~1.5 km of relief, and the canyon mouth outlet is <1 km to the east of the site (Fig. 3D; Supplemental File S3). We suggest that local retrogressive failure accompanying each seismic event, such as observed by Piper et al. (1999), may explain the repeated thinly laminated structures in core 104.

Another example is core 96PC, which has finer grained turbidites and higher overall sedimentation rate (turbidites are thicker; Table 6). Core 96 is located in a closed slope basin fed by very low relief terrain that does not form large channels (Fig. 6A). The low-relief terrain might explain the fine-grained texture, while the enclosed basin may be responsible for the relatively overthickened (ponded?) turbidites. Core 103 is in a location that has a low gradient, wide floodplain, and wide channel directly upslope, possibly explaining the low dynamic range of turbidite texture (Fig. 5D). Core 103 is located at the western edge of a small (~20 km^2) basin with eastward-sloping seafloor.

Our interpretation for proximity control on turbidite deposition is supported by looking at trench cores 98 and 94PC, along with some slope cores 104 and 103. Core 98 is located in the trench in a position protected from higher relief mass wasting processes sourced from the slope by a landward vergent anticline (Fig. 3F; Supplemental File S6). The turbidites are thin and less sandy than core 94PC, possibly as a result of this effect (Supplemental File S3). In contrast, core 94PC is located near the mouths of multiple canyon systems, and generally has thicker and sandier turbidites (Fig. 3G; Supplemental File S6). One amphitheater-shaped landslide source area directly feeds the seafloor surrounding core 94PC (arrow designates downslope direction in Fig. 3G). Proximal dominance is further supported by the stratigraphy in cores 103 and 104. While these cores are closely spaced (34 km apart; Fig. 3D) and correlate well with each other (Figs. 8–10), they have differences in turbidite style (thickness, structure) that probably reflect autocyclic forcing.

Stratigraphic Correlation Summary

The coherence of the turbidite fingerprints and radiocarbon ages between isolated basin and trench sites over 230 km along the strike of the subduction zone suggests that many or most of the correlated turbidites have a common trigger (Figs. 7–10). The good stratigraphic correlation between sites isolated from each other, from land sediment sources, and from other triggering mechanisms, coupled with consistent radiocarbon ages, suggests that the most likely triggering mechanism is regional subduction zone earthquakes. Uncorrelated turbidites present at some sites may be random sediment failures or smaller, local earthquakes. These uncorrelated turbidites commonly are thin and have low mass with nonunique fingerprints, making it more difficult to interpret their origin. We observe no examples of major turbidite beds that have no likely correlatives in other cores.

Age Relations

Radiocarbon ages provide a test of the temporal coherence of our correlations, but we also use them as a first-order control on the age of turbidites and recurrence of the earthquakes proposed as the origin for those turbidites (detailed radiocarbon methods are described in Supplemental File S2). Trench cores do not have radiometric age control, thus correlations between these and other cores do not have an independent test for our stratigraphic correlations. Therefore all of our correlations in the trench cores are tentative (Fig. 8; Supplemental File S3). One important source of aleatory uncertainty is basal erosion (Goldfinger et al., 2012a). Erosion preceding turbidite deposition would remove the youngest sediments underlying the turbidite, causing ^{14}C

Geosphere, published online on 12 November 2015 as doi:10.1130/GES01066.1

ages derived from those sediments to be older than the time of deposition. Erosion may be evaluated by collecting multiple cores at a given site (methods in Goldfinger et al., 2012a; Gutiérrez-Pastor et al., 2009). These erosion estimates are minimum estimates because there are no direct observations of the seafloor prior to the deposition of these turbidites, and erosion of all sites may be missed. Due to wire handling equipment failures, we were unable to collect multiple cores at each site, limiting our ability to evaluate erosion. Therefore our age models do not include assessment of basal erosion. The effect likely produces an overestimate of turbidite ages, as well as an increased scatter of ages among sites for turbidites even if they are synchronous.

There does not appear to be a systematic explanation for the small number of outlier ages. The excluded ages only slightly overlap with ages from underlying turbidites and there is no overlap with the overlying turbidite. We removed one age for T-33 in core 108PC (Table 5A) because it is ~310 yr older than the corresponding age in core 103PC. We removed one age for T-41 in core 108PC (Table 5A) because it is ~400 yr older than the corresponding age in core 103PC. We do not have an explanation for the older ages for T-33 or T-41 in core 108PC, but consider the correlation strong enough to reject the age on this basis. Because age biases due to erosion and the detrital material being dated almost always drive ages older, and rarely younger (Goldfinger et al., 2012a), it is common to have an age that is too old and virtually impossible to have one that is too young; thus we choose to remove the older ages in core 108PC from the combines for T-33 and T-41. This age sample also has the lower agreement index A_{comb}.

After outlier removal, the remaining ages satisfy the measures of agreement. The age model is therefore compatible with our stratigraphic correlations within the uncertainties inherent in radiocarbon, and the outlier removal seems reasonable. The external criteria on which the lithostratigraphic correlations are based support the inference that these horizons, in this context, most likely represent the same trigger event temporally. We therefore have combined them statistically in Table 7 and Figures 3 and 8. The OxCal code and log output of our radiocarbon age model with both modeled and unmodeled ages listed in Table 5 are found in Supplemental Files S2 and S5A.

Lithostratigraphy, radiocarbon ages, and geophysical log correlation suggest a good correlation of turbidites T-1–T-17 in core 96PC and T-1–T-21 between cores 108PC, 105, 104PC, and 103. These cores span the southernmost 2004 rupture zone and the earthquake records found in these cores likely represent earthquakes with associated spatial limits to earthquake ground motions (Figs. 8 and 11). The turbidites that are not correlated in core 108PC may represent earthquakes with more limited rupture length than the 2004 earthquake (i.e., smaller earthquake magnitude). It may also be that this core contains these turbidites, but the turbidites are too bioturbated or muddy to resolve (Goldfinger et al., 2013b). Less well correlated are turbidites T-22–T-39 in cores 108PC, 105PC, and 103PC, T-22–T-37 in core 104PC, and turbidites T-39–T-43 in cores 108PC and 103PC. Some ages (e.g., T-33 for core 108PC with core 103PC and T-41 for core 108PC and core 103PC) are incompatible with the preferred stratigraphic interpretations in Figure 8, but none of the ages overlap substantially with underlying turbidite ages (Figs. 8 and 11; Supplemental File S3). These small differences in age may be due to differences in basal erosion (more erosion means an older age), to minor differences in the marine reservoir (which are not yet resolvable), miscorrelations, or noncorrelation.

Origin of the Sumatra Turbidites

Sumatra Specific Factors

Of the potential triggering mechanisms proposed (Adams, 1990; Goldfinger et al., 2003, 2012a; Shanmugam, 2008), only a subset of these triggers applies to outer forearc sites offshore of Sumatra. In addition, several mechanisms do not directly trigger slope failure, but simply precondition slopes for failure (e.g., sediment loading, tectonics oversteepening, and regional gas hydrate destabilization). The remaining mechanisms are hyperpycnal flows, wave loading, bolide impact, self-failures, and earthquakes (intraplate and interplate). Frequent gas hydrate destabilization events linked to local as opposed to regional temperature changes would likely not occur synchronously and therefore could not be responsible for triggering frequent submarine landslides across large areas, as found in our cores. Crustal earthquakes and structural oversteepening and self-failures would leave behind highly localized deposits because their impact is localized. Bolide impacts may also leave a regional turbidite record, but their recurrence, on the order of thousands of years, is far too long to explain the chronostratigraphy in our cores (Rampino and Stothers, 1984; Rampino, 1984, 1999, 2002; Ward, 2002; Chesley and Ward, 2006). The remaining processes that can be both regional and synchronous include hyperpycnal flows, wave loads (storm and tsunami), and earthquakes (discussed in the following).

Hyperpycnal flow. Very large storms could potentially generate hyperpycnal flows, leaving behind hyperpycnites as the result of fluvial delivery of sediment to the coastal margin or through the resuspension of sediment along the continental shelf. In the region of the 2004 SASZ earthquake, core sites are located near landslide source areas that have no direct connection with continental shelf or fluvial sedimentary systems because the 50–70-km-wide unfilled Aceh Basin isolates the outer prism from this terrigenous input. The forearc plateau rises an average of 2.2 km above the forearc basin floor, effectively trapping all terrigenous input in the basin to the east. The Sumatra forearc plateau has a number of islands that could provide terrigenous input to sites downslope in the outer forearc. The nearest island, Simeulue, is 130 km to the southeast of our nearest slope core site, and there is no sedimentary pathway linking Simeulue to any of the core sites discussed here. We also note that hyperpycnites are reported to initially coarsen upward and then fine upward, representing the waxing and then waning of the hyperpycnal flow (Mulder et al., 2003; St-Onge et al., 2004). Turbidites in our cores do not show evidence of this depositional sequence, consistent with the observations of the spatial isolation of landslide source areas that feed our core sites.

Geosphere, published online on 12 November 2015 as doi:10.1130/GES01066.1

TABLE 7. RADIOCARBON AGES AND PRESENCE OR ABSENCE FOR REGIONAL TURBIDITES IN THE 2004 SUMATRA-ANDAMAN SUBDUCTION ZONE EARTHQUAKE REGION

Regional turbidite number	Analysis type*	Source core	Regional median age (yr B.P.)†	95% error (yr)	Core presence of regional turbidite§												
					108	107#	105#	104	103	102	99#	98#	96	95	94#	93#	88#
1	P_Sequence	96PC	60	150	xx	—	—	xx	—	xx	xx	—	xx	xx	xx	xx	xx
2	R_date	104TC	390	260	—	—	x	xx	—	xx	—	—	xx	—	—	—	—
3	Combine	96PC,104PC	630	110	xx	x	x	xx	xx		—	—	xx	—	—	—	—
4	Combine	104TC,104PC	740	110	—	x	x	xx	xx		—	—	xx	—	—	—	—
5	Combine		820	130	xx	x	x	xx	xx			—	xx	—	—	—	—
6	Synthetic		940	180	—	x	x	xx	xx			—	xx	—	—	—	—
7	Combine	96PC,104PC	1080	140	—	x	x	xx	xx			—	xx	—	—	—	—
8	Synthetic		1220	210	—	x	x	xx	xx			—	xx	—	—	—	—
9	Synthetic		1370	200	—	—	x	xx	xx			—	xx	—	—	—	—
10	Combine	103TC,103PC,104PC,108TC,108PC	1500	110	xx	x	x	xx	xx			—	xx	—	—	—	—
11	Combine	96PC,103TC	1620	140	—	x	x	xx	xx			—	xx	—	—	—	—
12	Synthetic		1730	200	—	x	x	x	xx			—	xx	—	—	—	—
13	Synthetic		1840	220	—	x	x	x	xx			—	xx	—	—	—	—
14	R_date	104PC	1950	210	xx	x	x	x	xx			—	xx	—	—	—	—
15	Synthetic		2030	190	—	x	x	xx	xx			—	xx	—	—	—	—
16	R_date	96PC	2110	150	—	—	—	x	xx			—	xx	—	—	—	—
17	Synthetic		2210	210	—	x	x	xx	xx			—	xx	—	—	—	—
18	Synthetic		2310	230	—	x	x	xx	xx			—	x	—	—	—	—
19	Synthetic		2410	230	—	—	x	xx	xx								
20	R_date	103PC	2520	190	—	x	x	xx	xx								
21	Combine	103TC,103PC,104PC,108PC	2750	100	xx	x	x	xx	xx								
22	Synthetic		2920	300	x		x	x	x								
23	Synthetic		3120	380	x		x	x	x								
24	Synthetic		3320	420	x		x	x	x								
25	Synthetic		3530	400	x		x	x	x								
26	Synthetic		3720	340	x		x	x	x								
27	Combine	103PC,108PC	3900	190	x		x	xx	xx								
28	Synthetic		4210	310	x		x	xx	xx								
29	R_date	108PC	4460	150	x		x	xx	xx								
30	Synthetic		4510	160	x		x	xx	xx								
31	Synthetic		4550	170	x		x	xx	xx								
32	Synthetic		4590	170	x		x	xx	xx								
33	R_date	103PC	4630	160	x		x	xx	xx								
34	Synthetic		4720	220	x		x	xx	xx								
35	Synthetic		4810	240	x		x	xx	xx								
36	Synthetic		4910	250	x		x	xx	xx								
37	Synthetic		5010	240	x		x	x	x								
38	Synthetic		5110	220	x		x		x								
39	R_date	108PC	5220	160	x		x		x								
40	R_date	103PC	5790	140	x				x								
41	R_date	103PC	6030	150	x				x								
42	R_date	103PC	6470	130	x				x								
43	R_date	108PC	6600	140	x				x								

*R_date ages are the result of using the Sequence command in OxCal (see text). Combine ages are based on the Combine function in OxCal. Synthetic ages are based on the Date command in our OxCal age model. Synthetic ages are not attributed to any source core. P_Sequence ages are based on a P_Sequence age model for a single core.

†Calibrated age and errors reported to 95.4% error and are reported in calendar years. Calibrated age ranges before A.D. 1950 (B.P.) according to Stuiver and Reimer (1998) calculated using marine reservoir correction and regional ΔR offset (ΔR = 16 ± 78).

§The more certain that a regional turbidite is present in a given core is designated xx. The less certain that a regional turbidite is present in a given core is designated x. The absence of a correlated turbidite is designated —.

#Trench cores with sediments of low dynamic range, or greater coring deformation, are correlated with lesser certainty.

Geosphere, published online on 12 November 2015 as doi:10.1130/GES01066.1

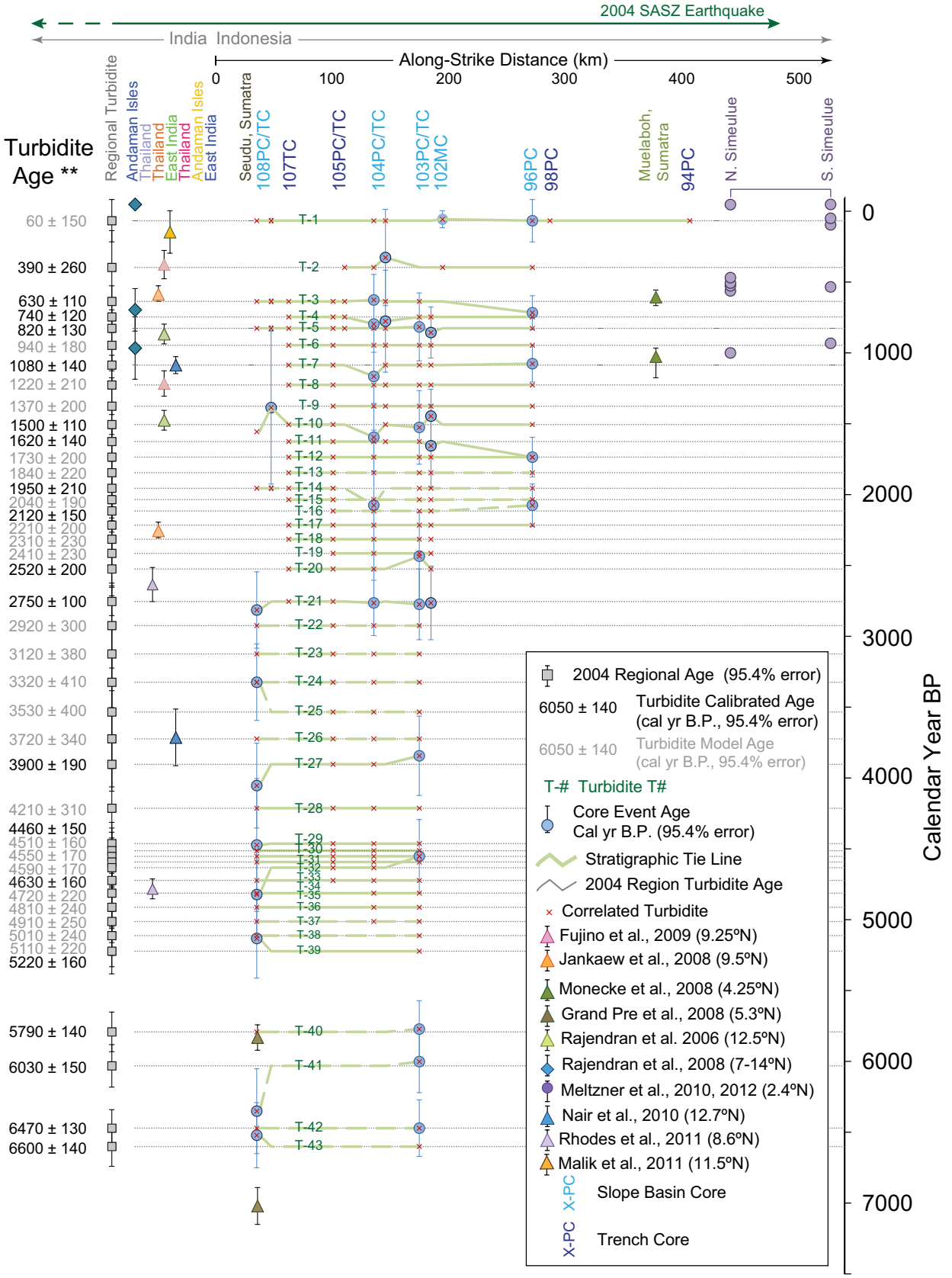

* Single ^{14}C age calibrated and reported according to Stuiver et al. (1998) calculated using marine reservior correction (ΔR = 16 ± 78). Error reported to 95.4%.
** Median age for each event, from Combine model (Table 5B). Grey ages are calculated with the "Date" OxCal command.
¥ OxCal v4.1.3 Bronk Ramsey (2009 a); Marine data from Reimer et al. (2009)

Figure 11. Earthquake chronology. Space-time relations for stratigraphy cored in the 2004 rupture region are plotted (versus forearc distance in km, from the India-Indonesia border) as blue circles with 95.4% error bars. Green tie lines show stratigraphic correlations (solid—correlation more certain, dashed—less certain). Region-wide events are designated by a horizontal dotted gray line and labeled with median ages on the left margin, along with the sequence age as gray squares with 95.4% error bars. Red x symbols designate correlated turbidites that lack ^{14}C age control. Terrestrial paleoseismic and paleotsunami data are plotted (see legend). Site locations are listed at the top of the plot. Data plotted to the left of core 108PC are not plotted versus forearc distance as they are farther north than the extent of the coring investigation. The 2004 earthquake extent, labeled with a green arrow, extends beyond the northern latitudinal extent shown in this figure (Chlieh et al., 2007). See Supplemental Files S2 and S5 for more detailed radiocarbon age discussions and presentations. Coral microatoll ages (Meltzner et al., 2010, 2012) are concatenated into two groups, N. and S. Simeulue; this evidence comprises multiple sites (Fig. 1; Supplemental File S1).

Geosphere, published online on 12 November 2015 as doi:10.1130/GES01066.1

Wave Loading. Wave loads can potentially trigger submarine landslides in two ways: (1) cyclic changes in pore pressure causing liquefaction induced slope failure and (2) shear failure of sediment on the slope, canyons, or shelf. These wave loads can be induced from storm waves or from tsunami waves.

Significant wave height, Hs, and spectral mean and peak wave period, Tm and Tp, have been modeled with buoy data and measured using satellite altimetry (Young, 1999; Alves and Young, 2003; Izaguirre et al., 2011) for the northeastern Indian Ocean in the region of our paleoseismic survey. Buoy data models estimate Hs with a 100 yr return period to be 3.5–9.5 m (Caires and Sterl, 2005). Alves and Young (2003) used satellite altimetry measurements to estimate Hs with a 100 yr return period to be 6–10 m. Izaguirre et al. (2011) used satellite altimetry measurements from 1992 to 2010 to estimate Hs with a 20 yr return period at 5–7 m. Young (1999) calculated Tm and Tp using the spectral wave model WAM (Komen et al., 1994) and find Tm to range from 10 to 13 s and Tp to range from 6 to 8 s in the region of our paleoseismic investigation. Measurements collected for these estimates are short lived and may not fully capture the variability, potentially missing extreme events possibly occurring in the past 6600 yr. Notwithstanding this possible limitation, we adopt these values as characteristic for the northeast Indian Ocean.

Cheng et al. (2001) suggested that passing waves, whether storm or tsunami, induce pore pressure loads that increase with each successive wave. If the sediment properties result in undrained conditions, the increased pore pressure may induce liquefaction and induce slope failure. Based on models of cyclic loading and drainage tests, where pore space decreases and shear strength increases, the sediment can result in being more resistant to slope failure (Miyamoto et al., 2004). This cyclic loading, whether from passage of storm or tsunami waves, is likely to retard slope failure. Chang et al. (2004) modeled this resistance to liquefaction in saturated sandy nearshore settings offshore Taiwan. The maximum depth that liquefaction was induced was 15 m, much shallower than the source areas in this study. Storm wave heights ranged from 1.5 to 7 m and wave periods ranged from 5 to 12 s, both consistent with Hs and Tm and Ts for offshore Sumatra. We therefore conclude that wave loading at depths of 1500–5000 m in the source areas for our turbidite cores is unlikely. We note that the lack of cyclones in equatorial waters (Peduzzi et al., 2012) all but rules out massive regional storms as a sediment source via either hyperpycnal flows or wave loading. Were such cyclones present in the past, they would still fail to trigger turbidity currents on the forearc slope with the majority of minimum depths relevant to this study of ~1500 m.

Tsunami-triggered turbidity currents have been examined in several locales. A tsunami-generated turbidite on the Tohoku shelf was reported (Ikehara et al., 2014), clearly identified by ^{234}Cs, sourced from the Fukushima nuclear accident, that fades with depth on the upper slope and is not present in deep water (Ikehara et al., 2012). In Goldfinger et al. (2012) the sediment transport potential for storm and tsunami waves in Cascadia was calculated, and it was concluded that neither wave type could shear or transport sand at depths >~450 m.

A turbidity current triggered by a tsunami has been proposed for as the origin of a homogenite in the Mediterranean Sea (Kastens and Cita, 1981) sourced in water depths of 100–2000 m. However, Kastens and Cita (1981) required a wave height of 1.9–17 m linked to a volcanic collapse. The maximum amplitude of the 2004 tsunami based on ground deformation on Simeulue Island and modeling the wave as imaged, in the deep sea, by the TOPEX/Poseidon joint satellite mission and Jason altimetry (Wang and Liu, 2006) is 1.5–2 m, considerably smaller. The water depths in the source areas for our basin sites are generally greater (1500–5000 m) than the proposed source areas of the Mediterranean homogenite (Mediterranean Ridge and African shelves). In addition, sediments offshore of Sumatra are cyclically strengthened, as discussed herein, unlike the Mediterranean Ridge hemipelagites, making them less susceptible to this type of induced failure.

Weiss (2008) calculated the capability of the 2004 SASZ subduction zone tsunami to move fine sand to a maximum depth of 985 m in the Bay of Bengal and 335 m in the region of our paleoseismic investigation, and concluded that tsunamis of similar size or smaller than the 2004 tsunami would be unlikely to initiate motion on seafloor sediments with low cohesion (fine sand). Potential source areas for slope cores in this study range from 1.5 to 5 km, all deeper than the Weiss (2008) maximum modeled depth. Core 108 has a small region of potential source area that reaches depths as shallow as ~750 m, but because the cores that have correlatable deposits have deeper potential source areas, the potential for tsunami wave loading as a trigger for the landslides that resulted in the turbidites in our cores is very limited.

Comparisons to Onshore Paleoseismology

We directly compare our results with records of earthquakes in the form of sandy deposits interpreted to be paleotsunami deposits, records of uplifted abrasion platforms, and records of coseismic paleodeformation recorded by coral microatolls. Our turbidite based evidence suggests that the ages of the 7 earthquakes prior to 2004 were ca. 390 ± 260, 630 ± 110, 740 ± 120, 820 ± 130, 940 ± 180, 1,080 ± 140, and 1,220 ± 220 (cal yr BP). Based on paleotsunami evidence in Thailand, the penultimate tsunamigenic earthquake recorded onshore in Phra Thong was younger than 370 ± 100 cal yr BP (Fujino et al., 2009; may correlate with T-2, aged 390 ± 260 cal yr BP) and the ante-penultimate tsunami was younger than 580 ± 50 cal yr BP (Jankaew et al., 2008; may correlate with T-3, aged 630 ± 110 cal yr BP; Fig. 11); also, paleotsunami younger than 1,210 ± 90 cal yr BP (Fujino et al., 2009) may correlate with T-8 (aged 1,220 ± 210 cal yr BP). Based on uplifted marine abrasion platforms, penultimate and ante-penultimate earthquakes occurred 690 ± 150 and 960 ± 220 cal yr BP, respectively, in the Andaman-Nicobar Islands (Rajendran et al., 2008; may correlate with T-4, aged 740 ± 120 cal yr BP, and T-6, aged 940 ± 180 cal yr BP). Similarly, paleotsunami evidence in Aceh, Sumatra, suggests the penultimate large tsunami timing was 600 ± 60 cal yr BP and the ante-penultimate tsunami timing was 1,020 ± 110 (Monecke et al., 2008; may correlate with T-3, aged 630 ±

Geosphere, published online on 12 November 2015 as doi:10.1130/GES01066.1

110 cal yr BP, and T-7, aged 1,080 ± 140 cal yr BP). These data shown in Fig. 11 suggest a strong possibility that the deep water turbidite record and regional tsunami records of the last ~1,500 years are a good match.

The terrestrial record of paleotsunami is sparse prior to 1,220 cal yr BP, but we make some preliminary comparisons. Paleotsunami records are less reliably linked to individual fault segments, though some sites are more likely to represent earthquakes in the region of the 2004 SASZ earthquake (e.g. Thailand, India). Our turbidite T-10 (aged 1,500 ± 110 cal yr BP) may be linked to a tsunami in East India at 1,470 ± 70 cal yr BP (Rajendran et al., 2008). Our T-26 (aged 3,720 ± 340 cal yr BP) may correlate with another East India tsunami with an age of 3,710 ± 200 cal yr BP (Nair et al., 2010). Similarly, T-20 and T-35 (aged 2,520 ± 200 and 4,720 ± 220 cal yr BP, respectively) may correlate with evidence from Thailand tsunami with ages of 2,630 ± 120 cal yr BP and 4,780 ± 70 cal yr BP (Rhodes et al., 2011).

Meltzner et al. (2010, 2012) have demonstrated that some local uplifts on Simeulue Island were the result of slip on the Sumatra megathrust in paleoearthquakes similar to those in 2004 and 2005. They also show that earthquakes on the northern and southern parts of the island are distinct and thus define a segment boundary that was observed in the 2004–2005 sequence, as well as for prior earthquakes. Meltzner et al. (2012) interpret that the magnitude of vertical paleodeformation relates to the magnitude for those paleoearthquakes, for the past ~1,100 years. Larger paleoearthquakes are reported in northern Simeulue for the following times: 500 ± 3, 556 ± 2, and 994 ± 16 cal yr BP (1450, 1394, and 956 AD). Smaller paleo-uplifts occurred in northern Simeulue at 520 ± 3 and 462 ± 3 cal yr BP (1430 and 1488 AD). The ages of the three larger paleoearthquakes are 500 ± 3, 556 ± 2, and 994 ± 16 cal yr BP (1450, 1394, and 956 AD) and may correlate with T-2, T-3, and T-6, with ages of 390 ± 260, 630 ± 110, and 940 ± 180 cal yr BP (1560, 1320, and 1010 AD; Table 7), respectively. The ages for T-2, T-3, and T-6 support the hypothesis that there were at least three earthquakes that were recorded by both microatoll corals and in deep sea sediments. Two uplift event ages (462 ± 3 and 520 ± 3 cal yr BP; 1488 ± 3 and 1430 ± 3 AD; Meltzner et al., 2012) do not overlap with any turbidite ages. These two smaller uplifts were each observed at only a single site and may be the result of smaller subduction zone earthquakes (e.g., the 2002 November and 2008 February earthquakes; Briggs et al., 2006; Meltzner et al., 2012), crustal earthquakes (local to Simeulue), or slow earthquakes that would not coincide with ground motion–triggered submarine slides. There is a temporal gap (462–20 cal yr BP, i.e., 1488–1930 AD) in the Meltzner et al. (2012) microatoll record during which we do not observe any correlated turbidites. Meltzner et al. (2010, 2012) speculated about possible missing earthquakes that may have occurred between their penultimate large earthquake (in 520 ± 3 cal yr BP; 1450 ± 3 AD) and the 2004 earthquake, although we suggest that large earthquakes in this period are unlikely due to the absence of turbidites during this time, and no evident alternative explanations. Thresholds for recording earthquakes with coral microatolls are likely different than those for recording earthquakes in sedimentary deposits, however, making event comparisons problematic at this stage of development for the Sumatra margin paleoseismic record.

We note that the timing of the paleoearthquake record of the Siberut and Enggano segments (Kopp et al., 2008; Sieh et al., 2008; Philibosian et al., 2012, 2014) and the Meltzner et al. (2012) record overlap in age range with the penultimate (T-2) and antepenultimate (T-3) turbidite ages from this study. However, these uplift event ages from the Siberut and Enggano segments do not overlap with uplift event ages from Simeulue (Sieh et al., 2008; Meltzner et al., 2010, 2012, 2015; Philibosian et al., 2012). The overlap with turbidite ages is therefore due to the larger uncertainties for the turbidite ages, since the coral ages do not overlap. While long earthquake sequences such as the 2004–2010 sequence along Sumatra may have occurred in the past (Sieh et al., 2008), they are not necessarily the rule over the 6600 yr span in the turbidite record.

Although these comparisons are somewhat coarse, the offshore evidence is broadly compatible with the onshore paleoseismic events. Paleotsunami, microatoll, and uplifted reefs may not record all earthquakes and thus may also represent maximum intervals for recurrence of Great earthquakes sensitive to the recording thresholds of the different methods.

Temporal Pattern

We calculate mean recurrence intervals (RI) based on turbidite ages within single cores and based on turbidite ages from all cores using three methods (Tables 8 and 9). First we calculate the RI by dividing the age of the oldest turbidite in each core by the regional number of correlated deposit intervals for that core (Table 9). We also determine the RI by determining the mean downcore interseismic interval in each core (Tables 8 and 9). We perform these calculations for each core and then find the mean for all cores for the purpose of intersite comparison (Table 9), then consider how the turbidite class, along strike length of correlation, and turbidite thickness standards might affect our RI estimates (Table 9). We also make comparisons between our RI estimates with those of the terrestrial record, for comparable time periods.

Based upon the oldest well-correlated seismoturbidite in cores 108PC, 104PC, 103PC, and 96PC, the mean RI for earthquakes large enough to generate a correlatable geologic record in the region of the 2004 earthquake is 160, 140, 160, and 140 yr for those cores, respectively (Table 9). The mean of these similar RI estimates is 150 yr.

We consider the along-strike extent of turbidites, how well they meet turbidite classification criteria, and turbidite thickness, as criteria for separating potential large-magnitude subduction zone earthquake deposits from other sources. Correlation using any of these criteria essentially requires an earthquake origin; however, turbidites that fail to meet all of these criteria cannot be distinguished by their source from the four possibilities, crustal earthquakes, slab earthquakes, small subduction zone earthquakes, or large subduction zone earthquakes. We use these criteria to rank our correlations to these three Turbidite Correlation Standards:

(1) turbidites that correlate along strike for >200 km, have the majority of turbidites from all cores that meet the majority of turbidite classification

Geosphere, published online on 12 November 2015 as doi:10.1130/GES01066.1

TABLE 8. DOWNCORE RECURRENCE INTERVAL

Core	Regional correlated turbidite number	Age* (cal yr B.P.)	Error	RI†	Error	RI§	Error
96PC							
	2	190	210	190	210	240	210
	3	710	120	360	240	520	240
	7	1070	130	180	180	90	180
	11	1730	140	170	190	170	190
	16	2070	150	140	210	70	210
103PC							
	4	810	240	270	240	290	240
	10	1520	260	170	350	120	350
	20	2430	310	130	400	90	400
	21	2770	250	140	400	340	400
	27	3840	280	150	380	180	380
	33	4550	260	140	380	120	380
	NA	5500	240				
	40	5770	200	150	310	40	310
	41	6000	220	150	300	230	300
	42	6470	200				
104PC							
	3	620	180	310	180	340	180
	4	790	200	260	260	170	260
	7	1160	220	190	290	120	290
	11	1590	240	160	330	110	330
	14	2070	530	160	580	160	580
	21	2760	230	140	580	100	580
108PC							
	10	1550	270	170	270	180	270
	21	2810	270	140	380	110	380
	25	3320	300	140	400	130	400
	27	4050	470	160	560	370	560
	29	4470	320	160	570	210	570
	33	4820	280	150	430	90	430
	39	5130	300	140	410	50	410
	41	6350	230	160	380	610	380
	43	6520	270	160	350	90	350
	NA	7160	310				
	NA	7520	490				

Note: NA indicates a turbidite that is not regionally correlated with sufficient certainty. PC—Piston Core.

*Age is reported in calendar years with uncertainty reported to 95.4% error. Calibrated age ranges before A.D. 1950 according to Stuiver and Reimer (1998) calculated using marine reservoir correction and regional ΔR offset (ΔR = 16 ± 78).

†RI (recurrence interval) is calculated by dividing the age of the turbidite by the regional turbidite number minus 1.

§RI is calculated by dividing the preceding interevent time by the number of preceding turbidites minus 1 (see text). These data are plotted in Figure 11.

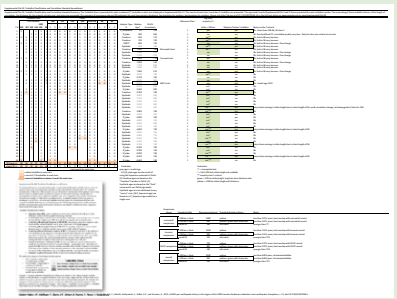

[9]Supplemental File S9. Turbidite classification and correlation standard summary. The turbidite class is presented for each numbered (T-) turbidite in each core displayed in Supplemental File S3. The counts of each class 1 and class 2 turbidites are presented. The age model results (Supplemental File S2 and S4A) are presented for each turbidite number. The accounting of these turbidite classes, strike length of correlation, thickness for the majority of each core, and notes are presented. The summary of recurrence interval (RI) estimates for each time period is displayed. See footnotes for notation. Please visit http://dx.doi.org/10.1130/GES01066.S9 or the full-text article on www.gsapubs.org to view Supplemental File S9.

criteria (class 1 turbidites), and have thicker turbidites in the majority of all cores (most confidence),

(2) turbidites that meet the turbidite class and thicker standards, but only correlate for >150 km (more confidence),

(3) turbidites that are correlated sufficiently to establish a seismogenic trigger based upon meeting our stratigraphic correlation criteria (less confidence; i.e., turbidites with T-numbers).

We choose 150 km as the minimum strike length over which beds should be correlatable to satisfy the length requirement, with >200 km used as a higher level of certainty. Strike length is limited in the 2004 rupture area, because no data are available north of the border with India. We also consider the number of beds along strike that are class 1 versus class 2 and class 3 beds (see Turbidite Classification Criteria in methods and Figure 5 E) as a measure of the robustness of the turbidite criteria, and also consider regionally consistent bed thickness as a measure of levels of ground shaking. While approximate, such relative measures have proved effective in Cascadia for both correlation and for linking the beds to the magnitudes of the source earthquakes (Goldfinger et al., 2012a, 2013b; Rong et al., 2014). Beds that meet all of these standards are stronger candidates for having been generated by regional subduction earthquakes (Supplemental File S8). Using these three standards of increasing confidence, we use the correlated turbidites to calculate three RIs (Table 9). Based on the range of standards met for discrimination between potential seismogenic sources, using the age to T-43 of ~6520 yr, we calculate an RI for the entire series of 2200 yr for turbidites that meet standard 1, RI of 550 yr for turbidites that meet standard 2 or higher, and RI of 160 yr for the entire series of 43 correlated deposits in the 2004 region. We discuss the RIs calculated for shorter time periods in the following (see overall comparison in Table 9).

If we then restrict the time ranges to make comparisons with other paleoseismic data, our RI estimates are compatible with other RI estimates. We first compare recurrences of earthquakes as recorded by regional paleotsunami deposits. RI estimates based on paleotsunami records are regional in nature, and likely to be generated by large earthquakes, although the knowledge of the spatial limits of ruptures that generated them is unknown (Dawson, 1999). We assume that the larger and regional subduction zone earthquakes are more likely to generate tsunamis that might be preserved in the geologic record than are tsunamis generated by smaller magnitude and more local earthquakes (Abe, 1979; Dawson and Stewart, 2007). These larger and regional earthquake-generated tsunamis are reasonable to compare with the seismoturbidite record because of a similar relation between trigger distance and earthquake magnitude for seismoturbidites (Black, 2014). Based on these limitations, we do not consider historic earthquakes in the Andaman Nicobar region that are <M 8.0 (A.D. 1679, 1847, 1881, 1941) for our RI estimate comparisons.

We combine these paleotsunami records in two ways: (1) using the records as completely unique (each paleotsunami represents a unique earthquake), and (2) using the records as reasonably correlatable (paleotsunami records with mostly overlapping age uncertainty are interpreted to be the result of the same earthquake; Supplemental File S9[9]). For the first tsunami RI estimate,

Geosphere, published online on 12 November 2015 as doi:10.1130/GES01066.1

TABLE 9. RECURRENCE INTERVAL ESTIMATES

Oldest age of turbidite*		Mean (interseismic time)†	
Core site	RI (yr)	Core	RI (yr)
108	160	108	200
104	140	104	170
103	160	103	210
96	140	96	220
All cores§	150	All cores§	200
Microatoll comparison#			
>200+ km strike distance	1080		
>150+ km strike distance	540		
Overall RI	180		
Tsunami comparison**			
>200+ km strike distance	1500		
>150+ km strike distance	500		
Overall RI	170		
96PC comparison††			
>200+ km strike distance	770		
>150+ km strike distance	460		
Overall RI	140		
Overall comparison§§			
>200+ km strike distance	2200		
>150+ km strike distance	550		
Overall RI	60		

*Recurrence interval, RI, is calculated by dividing the age of the oldest turbidite (T-; see text) in each core by the regional T- number for that core.

†RI is calculated by averaging the interseismic interval in each core, listed in the far right two columns in Table 8.

§The mean for all cores is the mean of the ages in that column (and a root mean square calculation of the standard deviation).

#The RI is calculated for a time period analogous to the microatoll record. Three RIs are calculated: (1) based upon turbidites that are correlated along strike for >200 km, (2) for turbidites that are correlated along strike for >150 km, and (3) for all turbidites that have T- numbers.

**The RI is calculated for a time period analogous to the tsunami record. Three RIs are calculated as for the microatoll comparison.

††The RI is calculated for the >200 km strike distance turbidite record. Three RIs are calculated as for the prior two methods.

§§The RI is calculated for the entire turbidite record. Three RIs are calculated as for the prior two methods.

considering records for the past ~1500 yr we find evidence for 10 earthquakes, including the 2004 SASZ earthquake (Fig. 11; yr before present): 1470 ± 70 (A.D. 480; Rajendran et al., 2006), 1210 ± 90 (A.D. 740; Fujino et al., 2009), 1080 ± 60 (A.D. 930; Nair et al., 2010), 1020 ± 110 (A.D. 930; Monecke et al., 2008), 860 ± 70 (A.D. 1090; Rajendran et al., 2006), 600 ± 60 (A.D. 1350; Monecke et al., 2008), 580 ± 50 (A.D. 1370; Jankaew et al., 2008), 370 ± 100 (A.D. 1580; Fujino et al., 2009), and 140 ± 150 (A.D. 1810; Malik et al., 2011). In the same time period, there are 10 seismoturbidites offshore of northern Sumatra, including the 2004 SASZ earthquake seismoturbidite, with the age of the oldest turbidite (T-10) for this span of 1500 ± 110 (Fig. 11; yr before present). The paleotsunami RI estimate is (1470)/(10 – 1) = 160 yr. We consider it possible and perhaps likely that the pair of paleotsunamis of age 1080 ± 60 and 1020 ± 110 (yr before present), and the pair dated 600 ± 60 and 580 ± 50 (yr before present) represent the same 2 earthquakes. If so, there would only be 8 earthquakes in this time range, yielding an RI estimate of (1470)/(8 – 1) = 210 yr. The lower paleotsunami RI of 160 yr is identical to the seismoturbidite value of ~170 yr (1500/10 – 1 = 167) for all correlated beds for the same period, and similar to the 210 yr RI for case where tsunamis that have closely overlapping radiocarbon ages are considered the same event. Of the 10 seismoturbidites in this time range, all but T-9 have potential tsunami correlatives with significant overlap of radiocarbon ages. When we consider the more restrictive turbidite correlation standards for the same time period, there are three seismoturbidites that meet standard 1 and five seismoturbidites that meet standard 2 or higher. It appears, however, that the more restrictive standard yields a poorer fit to the paleotsunami record (Table 9). Our attempt to discriminate between the four earthquake sources, three of which are much less likely to generate regional tsunami, appears more likely to show that all the correlated turbidites in this time range were sourced from significant subduction earthquakes capable of generating regional tsunami.

Microatoll records on Simeulue Island provide a unique record of paleodeformation that can also be compared to the seismoturbidite record. On northern Simeulue, for the past ~1100 yr (A.D. 2004 – 956 = 1048 yr), Meltzner et al. (2012) reported 4 earthquakes with larger inferred fault slip and as many as 6 earthquakes if we include records of paleodeformation with smaller inferred fault slip; we find that these two scenarios constrain RI estimates of ~350 and ~210 yr, respectively. The turbidite record, at 180 yr (6 events), compares reasonably well to the record for all events on northern Simeulue of 220 yr, and is identical to the tsunami interval of 180 yr for the same time period (6 events).

When we consider the turbidite correlation standards for the same time period, there is 1 seismoturbidite that meets standard 1, 3 seismoturbidites that meet standard 2 or higher, and 7 turbidites total, 3 of which only meet standard 3. The RIs for these three standards are 1080, 540, and 180 yr, respectively. The seismoturbidites of standard 2 or higher (3 earthquakes) match the Simeulue record in number and the total number of turbidites (7) is similar to the Simeulue record (6); however, the individual age overlaps are poor. Only T-1 and T-6 have good age matches. Four Simeulue events closely spaced in time between the mean ages of T-2 and T-3 overlap both those turbidite ages at the 95.4% uncertainty level (Fig. 11). Other turbidites appear not to have good matches with the microatoll record. Given that our RI estimates and those of Meltzner et al. (2012) describe earthquakes that generate observable records, these estimates are maximum recurrence intervals representing an unknown completeness of record in both cases. The reasons for a relatively poor fit to the microatoll data are unclear. The turbidite record for the 2004 rupture area covers ~270 km of strike length between the persistent (Meltzner et al., 2012)

Geosphere, published online on 12 November 2015 as doi:10.1130/GES01066.1

Simeulue segment boundary and the Indian border, while the tsunami record includes the entire Indian Ocean basin. We speculate that both the tsunami and turbidite records are more spatially extensive, and may be less subject to any spatial bias related to long-term slip heterogeneity (or lack thereof) or site location relative to past slip patches that might exist for what is essentially a single site at the north end of Simeulue Island.

To estimate a longer term RI, we extend our RI calculations to two longer time periods, the temporal limit of core 96PC and the temporal limit for all of the correlated turbidites. Correlations that satisfy the correlation standard 1 must extend between cores 108 and 96, so the correlations limited by core 96 provide the longest time span for the standard 1 RI. This RI has a more confident attribution to large subduction zone earthquakes. There are 4 seismoturbidites that satisfy standard 1, 6 seismoturbidites for standard 2, and 18 seismoturbidites in total for this time period; this results in calculated RIs of 770, 460, and 140 yr, respectively (Table 9). The correlations between cores 108 and 103 provide the longest time period with which to base a RI, though this is limited to a standard 2 correlation. For this RI, we cannot rule out seismogenic triggers from crustal, slab, or smaller subduction zone earthquakes. There are 4 seismoturbidites that satisfy standard 1, 13 seismoturbidites for standard 2, and 43 seismoturbidites in total for this time period; this results in calculated RIs of 2200, 550, and 160 yr, respectively (Table 9).

While we have more confidence in the more restrictive RI values, these restrictions are somewhat arbitrary, and belie the good fit of most turbidity current events to the onshore tsunami record for the ~1500 yr of record where multiple onshore sites are available (although we cannot rule out coincidence for this). The strike-length measurement is severely limited by the lack of data north of the Indian border, limiting the potential for along-strike correlation and therefore limiting the value of this measure. The beds emplaced during the ~1500 yr period of overlap with the tsunami record are not systematically higher or lower in quality of their characteristics or in their degree of preservation than those of earlier times; therefore we must consider the shorter recurrence interval of ~170 yr to be the preferred value from this study.

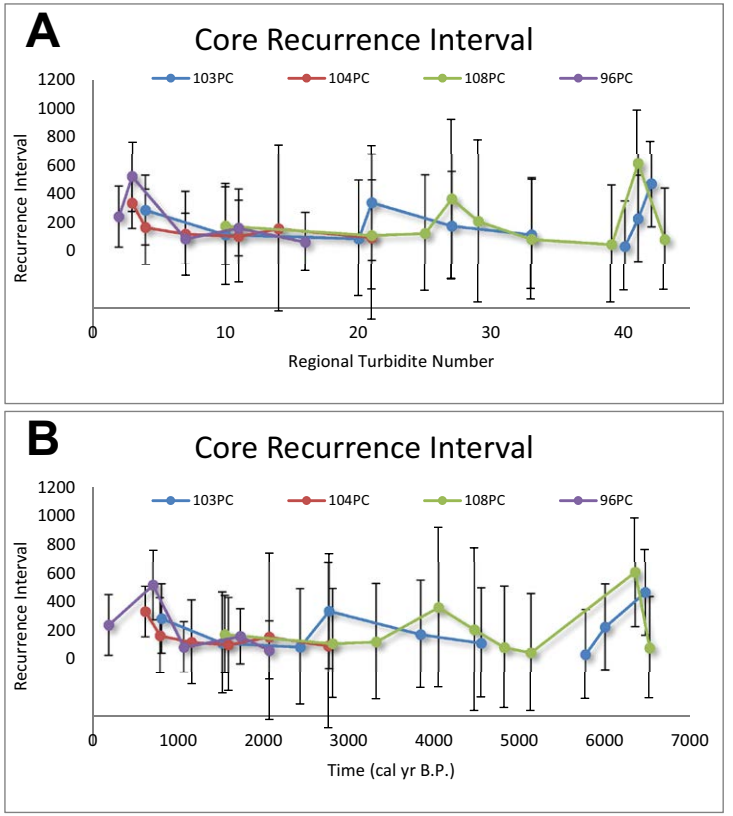

Figure 12. Downcore recurrence intervals (RI) are determined by dividing the time between turbidites by the span of turbidites that time represents (Table 8). The 95.4% error is plotted as vertical error bars. The RI is plotted in a different color for each core. (A) RI is plotted versus regional turbidite number. (B) RI is plotted versus age in cal yr B.P.

Intersite Comparison

We use the downcore series of recurrence intervals to make intersite comparisons. Downcore RI estimates are plotted as a function of age and correlated turbidite number in Figure 12. Time is in calendar years and error bars are plotted using one standard deviation RMS. These RI estimates are calculated by dividing the time between correlated turbidites by the number of correlated turbidites that are represented by that time span. We find that all cores share similar downcore recurrence trends, supporting a common trigger mechanism, because such similarity would not be expected for other random turbidite generating processes. Similar intersite matching trends were found in downcore RI estimates for Cascadia subduction zone earthquakes (Goldfinger et al., 2003, fig. 4 therein).

Longer RI times are represented by maxima in these plots centered approximately at 700 and 6500 yr. The shorter average RI between 1000–3000 yr ago and the longer RI span maxima centered at 0.7 and 6.5 ka are more robust examples of time length varying RIs because these estimates have more direct ages and thus a more continuous record of correlated turbidites in multiple cores. The RI maxima at 6.5 ka has fewer correlated turbidites in core 103PC than in core 104PC. The RI trends between cores 96PC, 103PC, and 104PC, for T-3–T-9 are similar. However, the maxima centered at 0.7 ka is much longer for core 96PC than for the other cores. Small variations in absolute RI length between cores may be due to age uncertainties or to earthquake strike length variations. These downcore variations in RI may also represent aperiodicity in subduction zone earthquakes, termed supercycles (Sieh et al., 2008; Goldfinger et al., 2013a).

Geosphere, published online on 12 November 2015 as doi:10.1130/GES01066.1

Extent of the 2004 and 2005 Turbidites and the Paleoseismic Record in Segment Boundaries

We note that the southernmost evidence for the 2004 turbidite is observed in core 95PC in a slope basin and core 88TC in the trench (Figs. 7 and 13). Slope cores provide a better constraint to the spatial limitations of ground shaking because their sedimentary sources and sinks are spatially restricted. Trench cores are less reliable for this purpose because turbidity currents can travel downtrench some unknown distance (trench mixing; Black, 2014). The slope cores nearest to the 2004 earthquake that likely lack a 2004 deposit are 92PC-92TC and 91MC. Core 91MC has a sedimentary section not sampled in core 92, an uppermost turbidite that is highly bioturbated and contains forams. This supports our interpretation that this core, at a range of ~100 km from the southern termination of 2004 slip, lacks a 2004 deposit. We do not have radiometric age estimates for this deposit in core 91MC. In the trench, turbidites in cores 93TC and 88TC have geophysical and structural similarities to the uppermost turbidite in core 96PC. Because of these similarities, we correlate, in cores 93TC and 88TC, the second turbidite from the top with T-1 in core 96PC. There is a younger turbidite in cores 93TC and 88TC that we suggest may have been deposited as a result of the March 2005 earthquake (Supplemental File S3).

There are few examples of rupture termination as observed in turbidite paleoseismic records with enough core data to constrain them. One such example was recently published for the Sumatra margin. Sumner et al. (2013) collected several cores ~50 km south of the rupture zone (based on slip model of Chlieh et al., 2007) of the 2004 Sumatra M_w 9.2 earthquake (cores labeled in

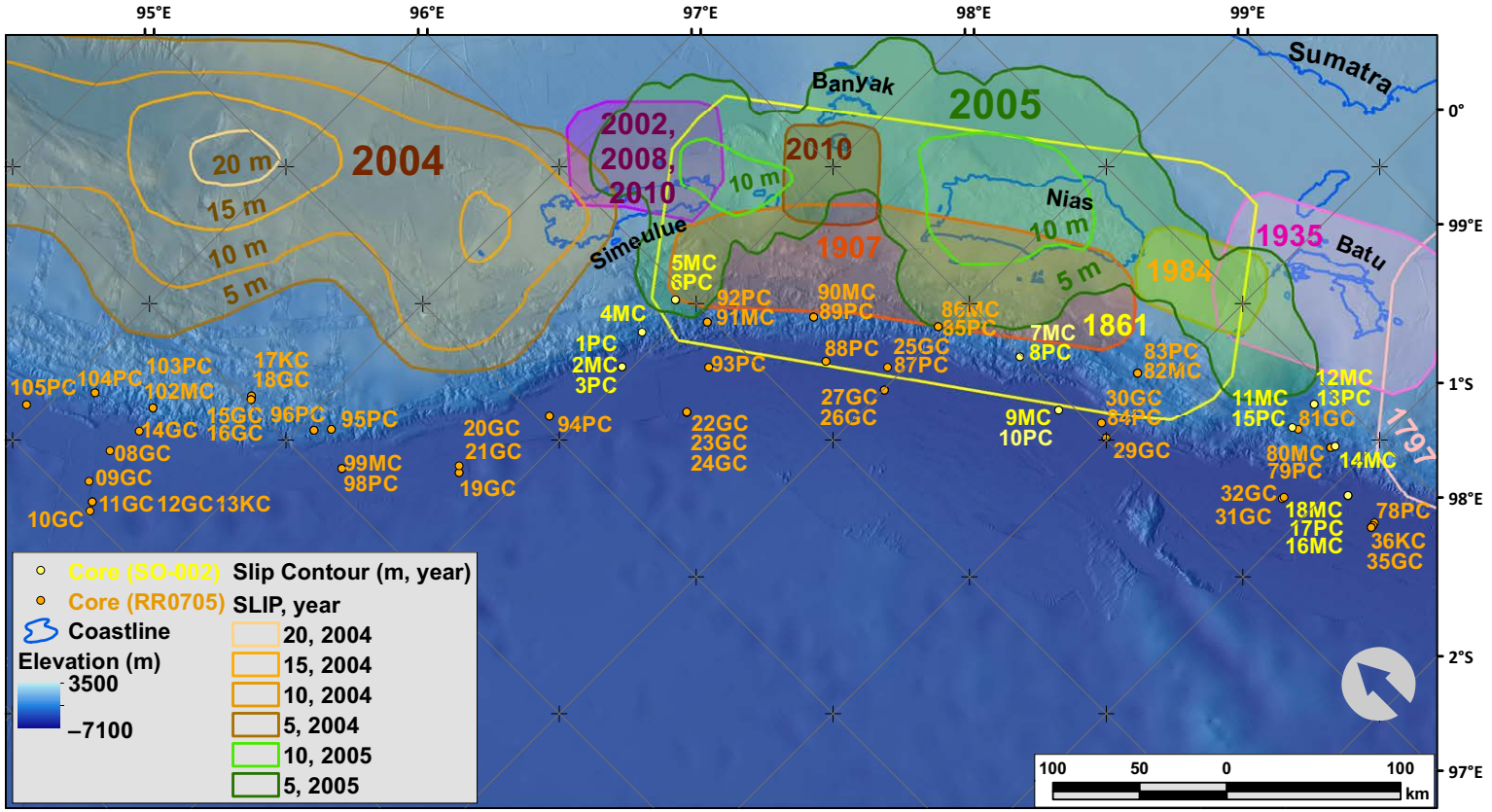

Figure 13. RR0705 and SO-002 core map; cores are plotted in orange and yellow in relation to slip regions for historic earthquakes (Bilham, 2005; Malik et al., 2011) plotted in Figure 1. The 2004 and 2005 slip contours are shown in orange and green, respectively (Chlieh et al., 2007, fig. 11 therein; Chlieh et al., 2008, fig. 20 therein). PC—piston core; MC—multicore; GC—gravity core; KC—Kasten core.

Geosphere, published online on 12 November 2015 as doi:10.1130/GES01066.1

yellow: 1PC, 2MC, 3PC, 4MC, 5MC, and 6PC; Fig. 13). Sumner et al. (2013) used SO-002 core data to state that not all large earthquakes generate turbidity currents, despite using nonideal sites and not having actually sampled the 2004 zone (Goldfinger et al., 2014a). The 2004 earthquake generated a widespread turbidity current and left widespread deposits in most of our sites (Figs. 3, 5, 7, 8, and 11). We use the SO-002 and RR0705 cores instead as part of a sensitivity test for triggering distance along strike. The value of this test is limited by the spatial extent of the two data sets, but suggests that in this case, distances of 50–100 km from the 1 m slip contour along strike could be too great for reliable recording of seismoturbidites on this part of the Sumatra margin. In addition to the limitations of spatially relevant SO-002 core sites, some were located in flat-floored, low-bathymetric-relief, wide basins that have proven to be of limited use for paleoseismology in slope settings (Goldfinger et al., 2014a, 2014b). We suggest that this is likely due to insufficient topography for local failures or due to the lack of channelized turbidity flow paths. Other SO-002 cores were located >30 km from their local canyon sources and >20 km from subdued local slopes. The slope failures leading to these SO-002 core sites are not channelized and thus the turbidity currents rapidly weaken as they spread across the basins (Nelson et al., 1986; Johnson et al., 2005; Patton et al., 2013a; Goldfinger et al., 2014a, 2014b). Core 2MC of Sumner et al. (2013) includes a surficial turbidite likely to be the 2004 turbidite based on its thickness and geophysical signature. Sumner et al. (2013, fig. 2B therein) agreed with our interpretation that SO-002–02MC includes a 2004 or 2005 deposit. This core is located in the trench (where there is possible sediment transport from the north) and is closer to the limit of slip for the 2004 earthquake than are any RR0705 slope cores, including core 96.

Given these limitations, a maximum triggering distance of ~50–100 km for the 2004 earthquake is supported by the data, subject to site sensitivities (Black, 2014). The 2004 earthquake had northward directivity, away from the core sites (Ammon et al., 2005; Ishii et al., 2005; Chlieh et al., 2007), possibly affecting this value locally. Because of the distance and rupture directivity, the SO-002 slope core sites were not ideal to record a turbidite from the 2004 earthquake, especially in slope basins. In addition, the main slip patch at the southern end of the rupture (i.e., Chlieh et al., 2007) was considerably north of the core sites (>200 km), thus likely strongly tapering ground motions southward toward the segment boundary. Ground motions in the 2011 Tohoku-Oki earthquake at both north and south ends of the rupture diminished along strike by an order of magnitude, from ~1 g (where g = Standard Gravity or 9.80665 m/s^2) to ~0.1 g, over a distance of ~100 km (Goto et al., 2012). Across-strike (along dip) energy radiation is broader because the energy is largely directed across strike in thrust earthquakes. This is a result of the orientation of the slip vector of the earthquake, which is typically normal to the trench. Ground shaking >0.5 g across strike extended across the forearc and well onshore, over a distance of 300 km, for the Tohoku-Oki earthquake (Goto et al., 2012). Records of ground shaking for the Tohoku-Oki earthquake exceeded 1 g, though these large values are thought to have been influenced by site conditions that may have amplified the ground shaking (Zhao and Xu, 2012). We therefore conclude that, while triggering distances are greater across strike, they are commonly more limited along strike (Black, 2014). As to the general question of how commonly do great earthquakes generate turbidity currents, we are not aware of any example of a submarine earthquake of M_w 8.3 or greater that did not generate turbidity currents where this has been tested (purposely or otherwise; see Black, 2014).

We also observe that the turbidite record becomes less robust in the region of the segment boundary of the 2004–2005 earthquakes, as well as the 2005 region. Segment boundaries typically are characterized by low or no slip during earthquakes and commonly have complex structural and slip transfer mechanisms from one segment to another (Barrientos and Ward, 1990; Bürgmann et al., 2005; Konca et al., 2008; Chlieh et al., 2007, 2008; Schurr et al., 2007; Hok et al., 2011; Kiser and Ishii, 2011; Hayes et al., 2013). They may also have many small earthquakes occurring between large earthquakes, leading to a confusing and likely incomplete record (e.g., historic earthquakes offshore Sumatra; Fig. 13). Briggs et al. (2006), Chlieh et al. (2008), and Meltzner et al. (2010, 2012) show the 2004 earthquake slip along the 2004–2005 boundary diminishing to near zero at the boundary, under central Simeulue Island. We find the turbidite record in the 2004–2005 segment boundary region (including our cores and those of Sumner et al., 2013), considered in the regional context presented here, consistent with the presence of a persistent segment boundary; this is also suggested by histories of land-level change deduced from coral microatolls across the boundary (Meltzner et al., 2012).

Compared to the 2004 earthquake (Ammon et al., 2005), the 2005 rupture was much smaller (M_w 8.7), and located much further downdip on the plate boundary. Slip in the outer forearc was not coseismic, but occurred over a span of several months (Hsu et al., 2006). For our core sites (and those of Sumner et al., 2013) focused in the outer wedge, the distance to the areas of greatest ground motion was much larger than in 2004, decreasing the likelihood of generating a viable turbidite record for that and other similar earthquakes. The turbidites we infer to have been emplaced as a result of the 2005 earthquake are much thinner (~2–3 cm thick in cores 88PC, 93PC, and 90MC; Supplemental File S3) than the turbidites emplaced following the 2004 earthquake (as much as ~3 m thick in core 96PC; Supplemental File S3).

Further analysis of the turbidites in the 2004–2005 rupture areas may address whether the 2004–2005 stress triggering relations are persistent features along the Sumatra margin (McCloskey et al., 2008; Meltzner et al., 2012; Kopp et al., 2008; Kopp, 2013). There are also significant differences in the incoming plate that may lead to variation in magnitude and recurrence of subduction zone earthquakes (Dean et al., 2010; Franke et al., 2008, Kopp, 2013). Offshore of Sumatra, the subductability of the oceanic lithosphere may be controlled by its thickness, buoyancy, and frictional variation generated by the ca. 36.5 Ma extinct slow spreading Wharton ridge (Jacob et al., 2014). These factors possibly explain the indentor (deviation of the curvilinear subduction zone fault) in the subduction zone fault from ~6°S to ~3°N (Jacob et al., 2014) as well as fault slip magnitude, recurrence, and the extent of updip and downdip and along-strike variations in seismic and aseismic slip (Bilek et al., 2011).

Geosphere, published online on 12 November 2015 as doi:10.1130/GES01066.1

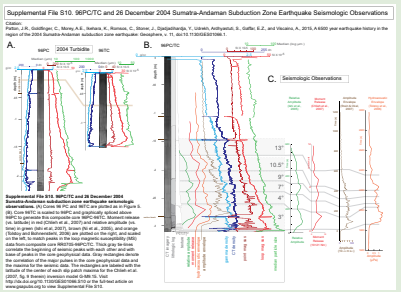

[10]Supplemental File S10. Core 96PC/TC and 26 December 2004 Sumatra-Andaman subduction zone earthquake seismologic observations. (A) Cores 96PC and 96TC are plotted as in Figure 5. (B) Core 96TC is scaled to 96PC and graphically spliced above 96PC to generate this composite core 96. Moment release (vs. latitude) in red (Chlieh et al., 2007) and relative amplitude (vs. time) in green (Ishii et al., 2007), brown (Ni et al., 2005), and orange (Tolstoy and Bohnenstiehl, 2006) are plotted on the right, and scaled on the left, to match peaks in the loop magnetic susceptibility (MS) data from composite core RR0705-96PC/TC. Thick gray tie lines correlate the beginning of seismic peaks with each other and with base of peaks in the core geophysical data. Gray rectangles denote the correlation of the major pulses in the core geophysical data and the maxima for the seismic data. The rectangles are labeled with the latitude of the center of each slip patch maxima for the Chlieh et al. (2007, fig. 9 therein) inversion model G-M9.15. Visit http://dx.doi.org/10.1130/GES01066.S10 or the full-text article on www.gsapubs.org to view Supplemental File S10.

Paleoseismograms

Submarine landslides can be triggered when seismic waves propagate through the landslide source area. If the source time function (Tanioka and Ruff, 1997; Bilek et al., 2004; Bilek, 2007) of the slope failures drives the sediment flux into the landslide system, and allocyclic forcing dominates (Underwood et al., 2005; Dennielou et al., 2006), the longitudinal structure of the resultant turbidity current will have maxima associated with the peaks in seismic energy. Therefore, the vertical structure of the turbidite is expected to have coarse pulses of sediment corresponding to each pulse (maxima) in seismic energy. The general structure would have a coarse-grained base and fine upward, with multiple coarse subunits for each peak in seismic energy; particle size might scale with seismic energy.

We note that the 2004 turbidite has three major fining-upward coarse pulses and several minor coarse pulses, for a total of six subunits in the turbidite base. The 2004 SASZ earthquake has three primary slip subevents (Lay et al., 2005). The relation between the earthquake source time function and the corresponding deposit originally led to the suggestion that the deposit structure can be used as a paleoseismogram (Seilacher, 1969; Goldfinger and Morey, 2004; Goldfinger et al., 2007, 2012b). Seilacher (1969) suggested that sedimentary structures could develop as the result of seismic loads to existing sedimentary deposits, while in Goldfinger and Morey (2004) and Goldfinger et al. (2007, 2012b) it was suggested that the sediments deposited following the earthquake record the earthquake source mechanism in the deposit. The source time functions produced by others (Ishii et al., 2005, Chlieh et al., 2007; Stein and Okal, 2007; Tolstoy and Bohnenstiehl, 2006) are plotted in comparison to the uppermost turbidite in core 96PC (Supplemental File S10[10]). There is good agreement between these plots of seismic energy release and the vertical sedimentary structure leading us to our comparison (Patton et al., 2013a, fig. 6 therein). This interpretation is supported by results from laboratory experiments that related sediment flux with changes in sequential deposition of sediments with varying density (Garrett et al., 2011; Goldfinger et al., 2012a). We speculate that this uppermost turbidite offshore Sumatra probably satisfies the definition of paleoseismogram (Goldfinger and Morey, 2004; Goldfinger et al., 2007, 2012b). Our model predicts that these subevents may be recorded as discernible coarse pulses within the turbidite that can be correlated over large distances (Figs. 9 and 10). A similar conclusion was drawn for Cascadia earthquake turbidites (Goldfinger et al., 2012a); the mechanism has been tested in flume studies, and is predicted by theory and analog models (Goldfinger et al., 2012b, and references therein; Garrett et al., 2011).

CONCLUSIONS

We used multibeam bathymetry and seismic reflection data to develop an understanding of catchment basins, turbidity current pathways, and depositional styles, as well as to precisely locate our gravity cores, piston cores, Kasten cores, and multicores along the outer Sumatra forearc. The physiography of the forearc high and basin isolates these sites from terrestrial sediment input from Himalayan-derived sediment, and from large storms, providing good localities to investigate the potential for turbidite paleoseismology. We collected 144 sediment cores in the trench and in lower slope piggyback basins of the Sumatra accretionary prism. Our analysis of these cores used detailed physical property data, including computed tomographic X-ray (CT), gamma density, magnetic susceptibility, grain-size analysis, faunal analysis, and smear slides to evaluate the turbidite stratigraphy and sedimentology at each site. We use radiocarbon age control for piggyback basin sites above the CCD, and use ^{210}Pb and ^{137}Cs to evaluate the timing for the most recent sedimentary deposits. Using well-log correlation methods and the radiometric age control, we tested for potential correlations between isolated sites in piggyback basins and the trench. Turbidite stratigraphy is ubiquitous in isolated outer slope basin and trench sites along the northern Sumatra margin.

The youngest turbidite (21 examples) in the region of the 2004 rupture has no overlying hemipelagic sediment, no oxidation at the seafloor, and has ^{210}Pb and radiocarbon ages that overlap a zero age of emplacement. This bed was most likely emplaced within a few years of 2007. We interpret this turbidite as linked to the 26 December 2004 Great SASZ M_w ~9.2 earthquake. This earthquake triggered turbidity currents in multiple submarine drainage systems that left stratigraphic evidence in the form of multipulse turbidites in isolated slope basin and trench depocenters.

Lithostratigraphic correlation and radiocarbon ages support serial deposition of turbidites over the past ~6600 yr in outer slope basin and trench sites. While local depositional variability in slope basins is relatively high, the aggregate of core data in and near the 2004 rupture zone form a consistent stratigraphic sequence among basin and trench core sites. Local variability is observed (and expected) for various reasons, including basal erosion, heterogeneous source areas within the region, coring deformation, nonseismic events, and varying site geomorphology. Intersite correlation is strong enough that we consider most of these beds to be to have been deposited synchronously. This conclusion is supported, but cannot be proven, with consistent radiocarbon age control.

The fact that these Sumatra cores, in sedimentologically isolated and hydrodynamically unique systems, share similar turbidite sequences, suggests that they also share a common trigger mechanism. Random occurrences such as local self-failure, gas hydrate destabilization, and tectonic oversteepening would not be expected to correlate among sites, develop self-similar sequences in numerous isolated basins, or have any resemblance in their temporal history. Because triggering by large storm effects (hyperpycnal flow, wave loading) and triggering by passage of tsunami waves are excluded by both water depth and physiography, earthquakes are the best explanation for regional and synchronously triggered turbidity currents. While individual deposits cannot be unequivocally linked to earthquakes, alternative mechanisms would need to affect the different regions with similar frequency and result in

Geosphere, published online on 12 November 2015 as doi:10.1130/GES01066.1

landslides with similar turbidite structures, in the same stratigraphic order, to explain the sediment stratigraphy found in these cores.

Among slab, crustal, and subduction zone earthquakes, discrimination of these types is not straightforward. Regional correlation within the 2004 rupture zone is limited to ~270 km by the lack of data along the India margin. Nevertheless, for the best period of overlap comprising the last ~1500 yr, the turbidite sequence comprises 10 events, and regional evidence for significant tsunami most likely includes 8 discrete events, all of which have significant overlap in radiocarbon ages with the offshore turbidites. Comparison of the turbidite stratigraphy with earthquake records in the form of uplifted coral microatolls reveals only two to three likely temporal matches over ~1100 yr. The reasons for this difference are not clear, but may be the result of spatial aliasing of the spatially limited coral records versus the more spatially extensive tsunami and turbidite records.

Previous Great earthquakes in the 2004 rupture region have shaken sufficiently to trigger at least 43 turbidity currents and to deposit corresponding turbidites during the past ~6.6 k.y., yielding an average repeat time of 160 yr. For the period of overlap with the tsunami record, the recurrence average for 8 discrete events is similar to the turbidite record at ~210 yr and 170 yr, and given the individual event overlaps in time, we prefer this recurrence interval as the best representation of significant subduction zone earthquakes in the region. Crustal, slab, and small plate boundary earthquakes may be present in the record as well, but are considered less likely sources due to the strong correspondence with the regional tsunami record.

The structure of the 2004 turbidite, with numerous replicates, comprises three main fining-upward subevents. The 2004 earthquake also comprises three main subevents both temporally and along strike (Supplemental File S10). This correspondence may support a recent hypothesis that the temporal pattern of seismic energy during the mainshock may impart a longitudinal structure to the resulting turbidity currents and thus be reflected in the deposits (Goldfinger et al., 2008, 2012a). The success of turbidite correlation in Cascadia, the northern San Andreas, and Sumatra suggests that some primary structure of the turbidity current maintains integrity, at least in the case of long-source Great earthquakes, despite the fluid dynamic complexity of turbidity currents. We speculate that the longitudinal heterogeneity of the turbidity current, allocyclic forcing imparted by the heterogeneous earthquake rupture (the source time function of the earthquake), may be recorded in the deposits (Goldfinger and Morey, 2004; Goldfinger et al., 2008, 2012a; Garrett et al., 2011). There may be potential to correlate the seismogenic forcing of these landslides with future work.

We find that selecting core sites is essential when attempting to evaluate the sedimentary record of past earthquakes. Based on the presence of a turbidite we interpret to be the result of the 2004 SASZ earthquake in the RR0705 and SO-002 cores, and a global sensitivity analysis, we find a maximum along-strike triggering distance for the southern limit of the 2004 earthquake to be ~50–100 km. The best coring sites will conjoin as many positive factors as possible: these are factors that promote seismogenic triggering of turbidity currents and promote the deposition and preservation of their turbidites. Ideal paleoseismic locales would (1) comprise core sites nearest maximum shaking intensity; (2) have high-relief sources upslope; (3) be associated with turbidity current channels and canyons; and (4) comprise sites that may promote expanded stratigraphic section (such as those within enclosed basins). Poor localities include broad flat basins without channel systems, low-relief and distant topographic source areas, and persistent segment boundaries or other areas of reduced ground motion.

ACKNOWLEDGMENTS

This research was funded by the Ocean Sciences and Earth Sciences Divisions of the National Science Foundation (awards OCE 0526655, OCE 1030381). We are grateful for the comprehensive and constructive comments from Aron Meltzner and an anonymous reviewer. We thank the Indonesian Agencies BPPT (Badan Pengkajian dan Penerapan Teknologi) and LIPI (Lembaga Ilmu Pengetahuan Indonesia), collaborator Haryadi Permana, and the staff of the U.S. Embassy in Jakarta, without whom this work would not have been possible. We thank the Indonesian science party members Sapta Chahyadi, Eddy Hartantyo, Gatot Fajar Suryono, Yudo Haryadi, Riza Rahardiawan, Nanang, and Prabowo, and international science party members Alexis Vizcaino, Elena Pinero, Oriol Pique, Zoraida Rosello, Ximena Moreno, Russel Wynn, Eugene Morgan, and Stefan Ladage, for their hard work at sea. We thank M. Erhardt, Amy M. Garrett, and Robert H. Porter for conducting laboratory analyses; NOC (National Oceanography Centre, Southampton), IFREMER (Institut Français de Recherche pour l'Exploitation de la Mer), and BGR for providing key bathymetry and subbottom data; collaborator Eulalia Gracia and UTM-CSIC (Unitat de Tecnologia Marina–Consejo Superior de Investigaciones Científicas) Barcelona, for supporting participation of the large Spanish contingent; NOC for supporting participation of Russ Wynn; BGR for supporting participation of Stefan Ladage; and AIST-GSJ (National Institute of Advanced Industrial Science and Technology–Geological Survey of Japan) for supporting participation of Ken Ikehara. We also thank coring technicians from Oregon State University (OSU) including Chris Moser, Bob Wilson, Kurt Schultz, and Paul Walczak, and UTM coring technicians Ramon Amettler and Roberto Gonzalez. We thank Scripps resident technicians; R/V *Roger Revelle* Captain Tom Djardins and crew; student volunteers and faculty from OSU, including Bart DeBaere, Javier Moncada, and Maureen Davies. We also thank Rob Wheatcroft (OSU) and Guillaume St-Onge (Institut des Sciences de la Mer de Rimouski) for assistance with ^{210}Pb and ^{137}Cs analyses; Jerry Thompson of Rainstory Productions for supporting videographer Chris Aikenhead; and Morgan Erhardt, Amy M. Garrett, Jeff Beeson, Handoko Wendobo, and Bran Black for identifying and collecting foraminifera tests. Further details regarding the cruise and the core locations are provided in this cruise report: http://www.activetectonics.coas.oregonstate.edu/sumatra/report/index.html.

REFERENCES CITED

Abdeldayem, A.L., Ikehara, K., and Yamazaki, T., 2004, Flow path of the 1993 Hokkaido-Nansei-Oki earthquake seismoturbidite, southern margin of the Japan Sea north basin, inferred from anisotropy of magnetic susceptibility: Geophysical Journal International, v. 157, p. 15–24, doi:10.1111/j.1365-246X.2004.02210.x.

Abe, K., 1979, Size of great earthquakes of 1837–1974 inferred from tsunami data: Journal of Geophysical Research, v. 84, p. 1561–1568, doi:10.1029/JB084iB04p01561.

Abercrombie, R.E., Antolik, M., and Ekstrom, G., 2003, The June 2000 Mw 7.9 earthquakes south of Sumatra: Deformation in the India-Australia plate: Journal of Geophysical Research, v. 108, no. B1, 2018, doi:10.1029/2001JB000674.

Adams, J., 1984, Active deformation of the Pacific Northwest continental margin: Tectonics, v. 3, p. 449–472, doi:10.1029/TC003i004p00449.

Adams, J., 1990, Paleoseismicity of the Cascadia subduction zone: Evidence from turbidites off the Oregon-Washington Margin: Tectonics, v. 9, p. 569–583, doi:10.1029/TC009i004p00569.

Alam, M.N., Chowdhury, M.I., Kamal, M., Ghose, S., Nahmood, N., Matim, N.A.K.A., and Saikat, S.Q., 1996, Radioactivity of ^{134}Cs, ^{137}Cs and ^{40}K in sea-water of the Bay of Bengal: Applied Radiation and Isotopes, v. 47, p. 33–35, doi:10.1016/0969-8043(95)00245-6.

Geosphere, published online on 12 November 2015 as doi:10.1130/GES01066.1

Almagor, G., and Wiseman, G., 1991, Analysis of submarine slumping in the continental slope off the southern coast of Israel: Marine Geotechnology, v. 10, p. 303–342, doi:10.1080/10641199109379898.

Alves, J.H.G.M., and Young, I.R., 2003, On estimating extreme wave heights using combined GeoSat, Topex/Poseidon and ERS-1 altimeter data: Applied Ocean Research, v. 25, p. 167–186, doi:10.1016/j.apor.2004.01.002.

Ammon, C.J., et al., 2005, Rupture process of the 2004 Sumatra-Andaman earthquake: Science, v. 308, p. 1133–1139, doi:10.1126/science.1112260.

Amy, L.A., and Talling, P.J., 2006, Anatomy of turbidites and linked debrites based on long distance (120 × 30 km) bed correlation, Marnoso Arenacea Formation, Northern Apennines, Italy: Sedimentology, v. 53, p. 161–212, doi:10.1111/j.1365-3091.2005.00756.x.

Amy, L.A., Talling, P.J., Peakall, J., Wynn, R.B., and Thynne, R.G.A., 2005, Bed geometry used to test recognition criteria of turbidites and (sandy) debrites: Sedimentary Geology, v. 179, p. 163–174, doi:10.1016/j.sedgeo.2005.04.007.

Arias, A., 1970, A measure of earthquake intensity, *in* Hansen, F.J., ed., Seismic design for nuclear power plants: Cambridge, Massachusetts Institute of Technology Press, p. 438–483.

Atkinson, G.M., and Boore, D.M., 2003, Empirical ground-motion relations for subduction-zone earthquakes and their application to Cascadia and other regions: Seismological Society of America Bulletin, v. 93, p. 1703–1729.

Atkinson, G.M., and Boore, D.M., 2011, Modifications to existing ground-motion prediction equations in light of new data: Seismological Society of America Bulletin, v. 101, p. 1121–1135.

Atwater, B.F., 1987, Evidence for great Holocene earthquakes along the outer coast of Washington State: Science, v. 236, p. 942–944, doi:10.1126/science.236.4804.942.

Atwater, B.F., and Hemphill-Haley, E., 1997, Recurrence intervals for great earthquakes of the past 3500 years at northeastern Willapa Bay, Washington: U.S. Geological Survey Professional Paper 1576, 108 p.

Atwater, B.F., and Griggs, G.B., 2012, Deep-sea turbidites as guides to Holocene earthquake history at the Cascadia Subduction Zone—Alternative views for a seismic-hazard workshop: U.S. Geological Survey Open-File Report 2012-1043, 58 p., http://pubs.usgs.gov/of/2012/1043/.

Atwater, B.F., Carson, B., Griggs, G.B., Johnson, H.P., and Salmi, M.S., 2014, Rethinking turbidite paleoseismology along the Cascadia subduction zone: Geology, v. 42, p. 827–830, doi:10.1130/G35902.1.

Baas, J.H., Van Kesteren, W., and Postma, G., 2004, Deposits of depletive high-density turbidity currents: A flume analogue of bed geometry, structure and texture: Sedimentology, v. 51, p. 1053–1088, doi:10.1111/j.1365-3091.2004.00660.x.

Baas, J.H., McCaffrey, W.D., Haughton, P.D.W., and Choux, C., 2005, Coupling between suspended sediment distribution and turbulence structure in a laboratory turbidity current: Journal of Geophysical Research, v. 110, C11015, doi:10.1029/2004JC002668.

Bacon, C.R., 1983, Eruptive history of Mount Mazama and Crater Lake caldera, Cascade Range, U.S.A.: Journal of Volcanology and Geothermal Research, v. 18, p. 57–115, doi:10.1016/0377-0273(83)90004-5.

Bacon, C.R., and Lanphere, M.A., 2006, Eruptive history and geochronology of Mount Mazama and the Crater Lake region, Oregon: Geological Society of America Bulletin, v. 118, p. 1331–1359, doi:10.1130/B25906.1.

Bandopadhyay, A., and Bandyopadhyay, R.R., 1999, Thermogenic hydrocarbons in the mid-proximal Bengal Fan, west of the Andaman-Nicobar Islands: Marine Georesources and Geotechnology, v. 17, p. 1–16, doi:10.1080/106411999273963.

Barnard, W.D., 1973. Late Cenozoic sedimentation on the Washington continental slope [Ph.D. thesis]: Seattle, University of Washington, 255 p.

Barnes, P.M., Bostock, H.C., Neil, H.L., Strachan, L.J., and Gosling, M., 2013, A 2300-year paleoearthquake record of the Southern Alpine fault and Fiordland subduction zone, New Zealand, based on stacked turbidites: Seismological Society of America Bulletin, v. 103, p. 2424–2446, doi:10.1785/0120120314.

Barrientos, D.E., and Ward, S.N., 1990, The 1960 Chile earthquake; inversion for slip distribution from surface deformation: Geophysical Journal International, v. 103, p. 589–598, doi:10.1111/j.1365-246X.1990.tb05673.x.

Bayes, M., and Price, M., 1763, An essay towards solving a problem in the doctrine of chances, by the Late Rev. Mr. Bayes, F. R. S. communicated by Mr. Price, in a letter to John Canton, A. M. F. R. S: Royal Society of London Philosophical Transactions, v. 53, p. 370–418, doi:10.1098/rstl.1763.0053.

Beeson, J.W., and Goldfinger, C., 2013, Large erosional features on the Cascadia accretionary wedge imaged with new high-resolution multibeam bathymetry and seismic datasets: American Geophysical Union, fall meeting, abs. S21C–2419.

Béjar-Pizarro, M., Socquet, A., Armijo, R., Carrizo, D., Genrich, J., and Simons, M., 2013, Andean structural control on interseismic coupling in the North Chile subduction zone: Nature Geoscience, v. 6, p. 462–467, doi:10.1038/ngeo1802.

Bilek, S.L., 2007, Using earthquake source durations along the Sumatra–Andaman subduction system to examine fault-zone variations: Seismological Society of America Bulletin, v. 97, p. S62–S70, doi:10.1785/0120050622.

Bilek, S.L., Lay, T., and Ruff, L.J., 2004, Radiated seismic energy and earthquake source duration variations from teleseismic source time functions for shallow subduction zone thrust earthquakes: Journal of Geophysical Research, v. 109, B09308, doi:10.1029/2004JB003039.

Bilek, S.L., Engdahl, E.R., DeShon, H.R., and El Hariri, M., 2011, The 25 October 2010 Sumatra tsunami earthquake: Slip in a slow patch: Geophysical Research Letters, v. 38, L14306, doi:10.1029/2011GL047864.

Bilham, R., 2005, Partial and complete rupture of the Indo-Andaman plate boundary 1847–2004: Seismological Research Letters, v. 76, p. 299–311, doi:10.1785/gssrl.76.3.299.

Bilham, R., Engdahl, R., Feldl, N., and Satybala, S.P., 2005, Partial and complete rupture of the Indo-Andaman Plate Boundary 1847–2004: Seismological Research Letters, v. 76, p. 299–311.

Blais-Stevens, A., and Clague, J.J., 2001, Paleoseismic signature in late Holocene sediment cores from Saanich Inlet, British Columbia: Marine Geology, v. 175, p. 131–148, doi:10.1016/S0025-3227(01)00132-3.

Blais-Stevens, A., Clague, J.J., Bobrowsky, P.T., and Patterson, R.T., 1997, Late Holocene sedimentation in Saanich Inlet, British Columbia, and its paleoseismic implications: Canadian Journal of Earth Sciences, v. 34, p. 1345–1357, doi:10.1139/e17-107.

Blais-Stevens, A., Rogers, G.C., and Clague, J.J., 2011, A revised earthquake chronology for the last 4,000 years inferred from varve-bounded debris-flow deposits beneath an inlet near Victoria, British Columbia: Seismological Society of America Bulletin, v. 101, p. 1–12, doi:10.1785/0120090360.

Black, B., 2014, Stratigraphic correlation of seismoturbidites and the integration of sediment cores with 3.5 kHz Chirp subbottom data in southern Cascadia [M.S. thesis]: Corvallis, Oregon State University, 211 p.

Blott, S.J., and Pye, K., 2006, Particle size distribution analysis of sand-sized particles by laser diffraction: An experimental investigation of instrument sensitivity and the effects of particle shape: Sedimentology, v. 53, p. 671–685, doi:10.1111/j.1365-3091.2006.00786.x.

Bock, Y., Prawirodirdjo, L., Genrich, J.F., Stevens, C.W., McCaffrey, R., Subarya, C., Puntodewo, S.S.O., and Calais, E., 2003, Crustal motion in Indonesia from global positioning system measurements: Journal of Geophysical Research, v. 108, no. B8, 2367, doi:10.1029/2001JB000324.

Boore, D.M., and Atkinson, G.M., 2008, Ground-motion prediction equations for the average horizontal component of PGA, PGV, and 5%-damped PSA at spectral periods between 0.01 s and 10.0 s: Earthquake Spectra, v. 24, p. 99–138, doi:10.1193/1.2830434.

Bothara, J., Beetham, R.D., Brunston, D., Stannard, M., Brown, R., Hyland, C., Lewis, W., Miller, S., Sanders, R., and Sulistio, Y., 2010, General observations of effects of the 30th September 2009 Padang earthquake, Indonesia: New Zealand Society for Earthquake Engineering Bulletin, v. 43, p. 143–173.

Bouma, A.H., 1962, Sedimentology of some flysch deposits: A graphic approach to facies interpretation: New York, Elsevier Publishing, 168 p.

Bouma, A.H., 2004, Key controls on the characteristics of turbidite systems, *in* Lomas, S.A., and Joseph, P., eds., Confined turbidite systems: Geological Society, London, Special Publication 222, p. 9–22, doi:10.1144/GSL.SP.2004.222.01.02

Bowman, G.M., 1985, Oceanic reservoir correction for marine radiocarbon dates from northwestern Australia: Australian Archaeology, v. 20, p. 58–67.

Bowman, G., and Harvey, N., 1983, Radiocarbon dating marine shells in South Australia: Australian Archaeology, v. 17, p. 113–123.

Briggs, R.W., et al., 2006, Deformation and slip along the Sunda megathrust in the great 2005 Nias-Simeulue earthquake: Science, v. 311, p. 1897–1901, doi:10.1126/science.1122602.

Bronk Ramsey, C., 1995, Radiocarbon calibration and analysis of stratigraphy: The OxCal program: Radiocarbon, v. 37, p. 425–430.

Bronk Ramsey, C., 2001, Development of the radiocarbon program OxCal: Radiocarbon, v. 43, p. 355–363.

Bronk Ramsey, C., 2008, Deposition models for chronological records: Quaternary Science Reviews, v. 27, p. 42–60, doi:10.1016/j.quascirev.2007.01.019.

Geosphere, published online on 12 November 2015 as doi:10.1130/GES01066.1

Bronk Ramsey, C., 2009a, Bayesian analysis of radiocarbon dates: Radiocarbon, v. 51, p. 337–360.
Bronk Ramsey, C., 2009b, Dealing with outliers and offsets in radiocarbon dating: Radiocarbon, v. 51, no. 3, p. 28.
Bürgmann, R., Kogan, M.G., Steblov, G.S., Hilley, G., Levin, V.E., and Apel, E., 2005, Interseismic coupling and asperity distribution along the Kamchatka subduction zone: Journal of Geophysical Research, v. 110, B07405, doi:10.1029/2005JB003648.
Çağatay, M.M., et al., 2012, Sedimentary earthquake records in the İzmit Gulf, Sea of Marmara, Turkey: Sedimentary Geology, v. 282, p. 347–359, doi:10.1016/j.sedgeo.2012.10.001.
Caires, S., and Sterl, A., 2005, 100-year return value estimates for ocean wind speed and significant wave height from the ERA-40 data: Journal of Climate, v. 18, p. 1032–1048, doi:10.1175/JCLI-3312.1.
Campbell, C.V., 1967, Lamina, laminaset, bed and bedset: Sedimentology, v. 8, p. 7–26, doi:10.1111/j.1365-3091.1967.tb01301.x.
Campbell, K.W., 1997, Empirical near-source attenuation relationships for horizontal and vertical components of peak ground acceleration, peak ground velocity, and pseudo-absolute acceleration response spectra: Seismological Research Letters, v. 68, p. 154–179, doi:10.1785/gssrl.68.1.154.
Carlson, P.R., 1967, Marine geology of Astoria submarine canyon [Ph.D. thesis]: Corvallis, Oregon State University, 259 p.
Chang, C.-H., Chien, L.-K., and Chang, Y.-H., 2004, 3-D liquefaction potential analysis of seabed at nearshore area: Journal of Marine Science and Technology, v. 12, p. 141–151.
Cheng, L.B., Sumer, M., and Freds, J., 2001, Solutions of pore pressure build up due to progressive waves: International Journal for Numerical and Analytical Methods in Geomechanics, v. 25, p. 885–907, doi:10.1002/nag.159.
Chesley, S.R., and Ward, S.N., 2006, A quantitative assessment of the human and economic hazard from impact-generated tsunami: Natural Hazards, v. 38, p. 355–374, doi:10.1007/s11069-005-1921-y.
Chhibber, H., 1934, Geology of Burma: London, McMillan, 538 p.
Chlieh, M., et al., 2007, Coseismic slip and afterslip of the great (Mw 9.15) Sumatra-Andaman earthquake of 2004: Seismological Society of America Bulletin, v. 97, p. S152–S173, doi:10.1785/0120050631.
Chlieh, M., Avouac, J.P., Sieh, K., Natawidjaja, D.H., and Galetzka, J., 2008, Heterogeneous coupling of the Sumatran megathrust constrained by geodetic and paleogeodetic measurements: Journal of Geophysical Research, v. 113, B05305, doi:10.1029/2007JB004981.
Colella, H., Dieterich, J.H., Richards-Dinger, K., and Rubin, A., 2012, Complex characteristics of slow slip events in subduction zones reproduced in multi-cycle simulations: Geophysical Research Letters, v. 39, L20312, doi:10.1029/2012GL053276.
Cowie, G., Calvert, S., De Lange, G., and Keil, R.H., 1998, Extents and implications of organic matter alteration at oxidation fronts in turbidites from the Madeira abyssal plain, *in* Weaver, P.P.E., et al., eds., Proceedings of the Ocean Drilling Program, Scientific results, Volume 157: College Station, Texas, Ocean Drilling Program, p. 581–590, doi:10.2973/odp.proc.sr.157.150.1998.
Dallimore, A., Thomson, R.E., and Bertram, M.A., 2005, Modern to late Holocene deposition in an anoxic fjord on the west coast of Canada: Implications for regional oceanography, climate and paleoseismic history: Marine Geology, v. 219, p. 47–69, doi:10.1016/j.margeo.2005.05.003.
Davis, E., Kinoshita, M., Becker, K., Wang, K., Asano, A., and Ito, Y., 2013, Episodic deformation and inferred slow slip at the Nankai subduction zone during the first decade of CORK borehole pressure and VLFE monitoring: Earth and Planetary Science Letters, v. 368, p. 110–118, doi:10.1016/j.epsl.2013.03.009.
Dawson, A.G., 1999, Linking tsunami deposits, submarine slides and offshore earthquakes: Quaternary International, v. 60, p. 119–126, doi:10.1016/S1040-6182(99)00011-7.
Dawson, A.G., and Stewart, I., 2007, Tsunami deposits in the geological record: Sedimentary Geology, v. 200, p. 166–183, doi:10.1016/j.sedgeo.2007.01.002.
Dean, S., McNeil, L.C., Henstock, T., Bull, J.M., Gulick, S.P.S., Austin, J.A., Jr., Bangs, N.L.B., Djadjadihardja, Y., and Permana, H., 2010, Contrasting décollement and prism properties over the Sumatra 2004–2005 earthquake rupture boundary: Science, v. 329, p. 207–210, doi:10.1126/science.1189373.
Dennielou, B., Huchon, A., Beaudouin, C., and Berné, S., 2006, Vertical grain-size variability within a turbidite levee: Autocyclicity or allocyclicity? A case study from the Rhône neofan, Gulf of Lions, Western Mediterranean: Marine Geology, v. 234, p. 191–213, doi:10.1016/j.margeo.2006.09.019.
Duncan, J.R., 1968. Late Pleistocene and postglacial sedimentation and stratigraphy of deep-sea environments off Oregon [Ph.D. thesis]: Corvallis, Oregon State University, 222 p.
Dura, T., Rubin, C.M., Kelsey, H.M., Horton, B.P., Hawkes, A., Vane, C.H., Daryono, M., Grand Pre, C., Ladinsky, T., and Bradley, S., 2011, Stratigraphic record of Holocene coseismic subsidence, Padang, West Sumatra: Journal of Geophysical Research, v. 116, B11306, doi:10.1029/2011JB008205.
Dutta, K., Bhushan, R., and Somayajulu, B.L.K., 2001, ΔR correction values for the northern Indian Ocean: Radiocarbon, v. 43, p. 483–488.
Enkin, R.J., Dallimore, A., Baker, J., Southon, J., Ivaniochko, T., and Lian, O., 2013, A new high-resolution radiocarbon Bayesian age model of the Holocene and late Pleistocene from core MD02–2494 and others, Effingham Inlet, British Columbia, Canada; with an application to the paleoseismic event chronology of the Cascadia Subduction Zone: Canadian Journal of Earth Sciences, v. 50, p. 746–760, doi:10.1139/cjes-2012-0150.
Ericson, D.B., Ewing, M., and Heezen, B.C., 1952, Turbidity currents and sediments in the North Atlantic: American Association of Petroleum Geologists Bulletin, v. 36, p. 489–511.
Fairbanks, R.G., Mortlock, R.A., Chiu, T.-C., Cao, L., Kaplan, A., Guilderson, T.P., Fairbanks, T.W., Bloom, A.L., Gootes, P.M., Nadeau, M.-J., 2005, Radiocarbon calibration curve spanning 0 to 50,000 years BP based on paired $^{230}Th/^{234}U/^{238}U$ and ^{14}C dates on pristine corals: Quaternary Science Reviews, v. 24, p. 1781–1796.
Faure, G., and Mensing, T.M., 2005, Isotopes principles and applications (third edition): New York, John Wiley and Sons, 928 p.
Felix, M., and Peakall, J., 2006, Transformation of debris flows into turbidity currents: Mechanisms inferred from laboratory experiments: Sedimentology, v. 53, p. 107–123, doi:10.1111/j.1365-3091.2005.00757.x.
Fisher, D., Mosher, D., Austin, J.A., Gulick, S.P., Masterlark, T., and Moran, K., 2007, Active deformation across the Sumatran forearc over the December 2004 Mw 9.2 rupture: Geology, v. 35, p. 99–102, doi:10.1130/G22993A.1.
Flynn, W.W., 1968, The determination of low levels of polonium-210 in environmental materials: Analytica Chimica Acta, v. 43, p. 221–227, doi:10.1016/S0003-2670(00)89210-7.
Fornes, W.L., DeMaster, D.J., and Smith, C.R., 2001, A particle introduction experiment in Santa Catalina Basin: Testing the age-dependent mixing hypothesis: Journal of Marine Research, v. 59, p. 97–112, doi:10.1357/002224001321237380.
Franke, D., Schnabel, M., Ladage, S., Tappin, D. R., Neben, S., Djadjadihardja, Y., Müller, R. D., Kopp, H., and Gaedicke, C., 2008, The great Sumatra–Andaman earthquakes—Imaging the boundary between the ruptures of the great 2004 and 2005 earthquakes: Earth and Planetary Science Letters, v. 269, p. 118–130.
Fujino, S., Naruse, H., Matsumoto, D., Jarupongsakul, T., Sphawajruksakul, A., and Sakakura, N., 2009, Stratigraphic evidence for pre-2004 tsunamis in southwestern Thailand: Marine Geology, v. 262, p. 25–28, doi:10.1016/j.margeo.2009.02.011.
Fukuma, K., 1998, Origin and applications of whole-core magnetic susceptibility of sediments and volcanic rocks from Leg 152, *in* Saunders, A.D., et al., eds., Proceedings of the Ocean Drilling Program, Scientific results, Volume 152: College Station, Texas, Ocean Drilling Program, p. 271–280, doi:10.2973/odp.proc.sr.152.225.1998.
Garrett, A.M., Goldfinger, C., Patton, J.R., and Morey, A.M., 2011, "Paleoseismograms": Testing a hypothesis of source-time function recording of paleoearthquakes: American Geophysical Union, fall meeting, abs. T51F-2421.
Ghaleb, B., 2009, Overview of the methods for the measurement and interpretation of short-lived radioisotopes and their limits: IOP Conference Series: Earth and Environmental Science, v. 5, no. 1, 14 p.
Gillespie, R., 1977, Sydney University natural radiocarbon measurements IV: Radiocarbon, v. 19, p. 101–110.
Gillespie, R., and Polach, H., 1979, The suitability of marine shells for radiocarbon dating of Australian prehistory, *in* Berger, R., and Suess, H., eds., Proceedings of the 9th International Conference on Radiocarbon Dating: Los Angeles: University of California Press. p. 404–421.
Gilmore, G., and Hemingway, J.D., 1995, Practical gamma-ray spectrometry: New York, Wiley, 314 p.
Goldfinger, C., 2009, Sub-aqueous paleoseismology, *in* McCalpin, J.P., ed., Paleoseismology (second edition): International Geophysics Series Volume 95: New York, Academic Press-Elsevier, p. 119–170.
Goldfinger, C., 2010, Submarine paleoseismology based on turbidite records: Annual Review of Marine Science, v. 3, p. 35–66, doi:10.1146/annurev-marine-120709-142852.

Geosphere, published online on 12 November 2015 as doi:10.1130/GES01066.1

Goldfinger, C., 2011, Possible turbidite record of earthquake source characteristics: A small scale test: U.S. Geological Survey National Earthquake Hazards Reduction Program Report 07HQGR0064, 18 p.

Goldfinger, C., and Morey, A., 2004, Physical property correlations from Cascadia great earthquakes: What are they telling us about the triggering events?: Eos (Transactions, American Geophysical Union), v. 85, abs. OS21E–01.

Goldfinger, C., Nelson, C.H., and Johnson, J.E., 2003, Holocene earthquake records from the Cascadia Subduction Zone and northern San Andreas fault based on precise dating of offshore turbidites: Annual Review of Earth and Planetary Sciences, v. 31, p. 555–577, doi:10.1146/annurev.earth.31.100901.141246.

Goldfinger, C., Morey, A.E., Nelson, C.H., Gutierrez-Pastor, J., Johnson, J.E., Karabanov, E., Chaytor, J., and Ericsson, A., 2007, Rupture lengths and temporal history of significant earthquakes on the offshore and north coast segments of the northern San Andreas fault based on turbidite stratigraphy: Earth and Planetary Science Letters, v. 254, p. 9–27, doi:10.1016/j.epsl.2006.11.017.

Goldfinger, C., et al., 2008, Late Holocene rupture of the northern San Andreas fault and possible stress linkage to the Cascadia Subduction Zone: Seismological Society of America Bulletin, v. 98, p. 861–889, doi:10.1785/0120060411.

Goldfinger, C., et al., 2012a, Turbidite event history: Methods and implications for Holocene paleoseismicity of the Cascadia Subduction Zone: U.S. Geological Survey Professional 1661–F, 170 p., http://pubs.usgs.gov/pp/pp1661f/.

Goldfinger, C., Garrett, A.M., Patton, J.R., and Morey, A.E., 2012b, Paleoseismograms: Can turbidite deposits record flow unsteadiness imparted by earthquakes?: American Geophysical Union, fall meeting, abs. T22D–06.

Goldfinger, C., Ikeda, Y., Yeats, R.S., and Ren, J., 2013a, Superquakes and supercycles: Seismological Research Letters, v. 84, p. 24–32, doi:10.1785/0220110135.

Goldfinger, C., Morey, A., Black, B., and Patton, J.R., 2013b, Spatially limited mud turbidites on the Cascadia Margin: Segmented earthquake ruptures: Natural Hazards and Earth System Sciences, v. 13, p. 2109–2146, doi:10.5194/nhess-13-2109-2013.

Goldfinger, C., Patton, J.R., Van Daele, M., Moernaut, J., Nelson, C.H., de Batist, M., and Morey, A.E., 2014a, Can turbidites be used to reconstruct a paleoearthquake record for the central Sumatran margin?: Comment: Geology, v. 42, p. e344, doi:10.1130/G35558C.1.

Goldfinger, C., Hamilton, T.S., Beeson, J., Galer, S., Nelson, C.H., Morey, A., and Udrekh, 2014b, Turbidite paleoseismology: Site selection, physiography, sediment supply, current dynamics and temporal considerations as applied in Cascadia and elsewhere: American Geophysical Union, fall meeting, abs. T52A-08.

Gonzalez-Yajimovich, O.E., Gorsline, D.S., and Douglas, R.G., 2007, Frequency and sources of basin floor turbidites in Alfonso Basin, Gulf of California, Mexico: Products of slope failures: Sedimentary Geology, v. 199, p. 91–105, doi:10.1016/j.sedgeo.2005.09.025.

Gorsline, D.S., De Diego, T., and Nava-Sanchez, E.H., 2000, Seismically triggered turbidites in small margin basins: Alfonso Basin, western Gulf of California and Santa Monica Basin, California borderland: Sedimentary Geology, v. 135, p. 21–35, doi:10.1016/S0037-0738(00)00060-9.

Goto, H., Morikawa, H., Inatani, M., Ogura, Y., Tokue, S., Zhang, X.-X., Iwasaki, M., Araki, M., Sawada, S., and Zerva, A., 2012, Very dense seismic array observations in Furukawa District, Japan: Seismological Research Letters, v. 83, p. 765–774, doi:10.1785/0220120044.

Gràcia, E., Vizcaino, A., Escutia, C., Asioli, A., Rodés, Á., Pallàs, R., Garcia-Orellana, J., Lebreiro, S., and Goldfinger, C., 2010, Holocene earthquake record offshore Portugal (SW Iberia): Testing turbidite paleoseismology in a slow-convergence margin: Quaternary Science Reviews, v. 29, p. 1156–1172, doi:10.1016/j.quascirev.2010.01.010.

Gràcia, E., et al., 2012, Acoustic and seismic imaging of the Adra fault (NE Alboran Sea): In search of the source of the 1910 Adra earthquake: Natural Hazards Earth System Sciences, v. 12, p. 3255–3267, doi:10.5194/nhess-12-3255-2012.

Graehl, N.A., Kelsey, H.M., Witter, R.C., Hemphill-Haley, E., and Englehart, S.E., 2014, Stratigraphic and microfossil evidence for a 4500-year history of Cascadia subduction zone earthquakes and tsunamis at Yaquina River estuary, Oregon, USA: Geological Society of America Bulletin, v. 127, p. 211–226, doi:10.1130/B31074.1.

Graindorge, D., et al., 2008, Impact of lower plate structure on upper plate deformation at the NW Sumatran convergent margin from seafloor morphology: Earth and Planetary Science Letters, v. 275, p. 201–210, doi:10.1016/j.epsl.2008.04.053.

Grand Pre, C., Horton, B., Kelsey, H., Rubin, C., Hawkes, A., Natawidjaja, D.H., Daryono, M., Yulianto, E., 2008, Application of microfossils to reconstruct a paleoseismic record of the Sunda subduction megathrust, northern Sumatra: Eos (Transactions, American Geophysical Union), v. 89, abs. U51A–0010.

Grantz, A., Phillips, R.L., Mullen, M.W., Starratt, S.W., Jones, G.A., and Naidu, A.S., 1996, Character, paleoenvironment, rate of accumulation, and evidence for seismic triggering of Holocene turbidites, Canada Abyssal Plain, Arctic Ocean: Marine Geology, v. 133, p. 51–73, doi:10.1016/0025-3227(96)00015-1.

Griggs, G.B., 1969, Cascadia Channel—The anatomy of a deep sea channel [Ph.D. thesis]: Corvallis, Oregon State University, 183 p.

Griggs, G.B., and Kulm, L.D., 1970, Sedimentation in Cascadia deep-sea channel: Geological Society of America Bulletin, v. 81, p. 1361–1384, doi:10.1130/0016-7606(1970)81[1361:SICDC]2.0.CO;2.

Gulick, S.P.S., Austin, J.A., Jr., McNeill, L.C., Bangs, N.L.B., Martin, K.M., Henstock, T.J., Bull, J.M., Dean, S., Djadjadihardja, Y.S., and Permana, H., 2011, Updip rupture of the 2004 Sumatra earthquake extended by thick indurated sediments: Nature Geoscience, v. 4, p. 453–456, doi:10.1038/ngeo1176.

Gutiérrez-Pastor, J., Nelson, C. H., Goldfinger, C., and Johnson, J. E., 2005a, Holocene turbidite and onshore paleoseismic record of great earthquakes on the Cascadia Subduction Zone: Relevance for the Sumatra 2004 great earthquake: Eos (Transactions, American Geophysical Union), v. 86, abs. U51A–03.

Gutiérrez-Pastor, J., Nelson, C.H., Goldfinger, C., and Johnson, J.E., 2005b, Holocene turbidite history in the Cascadia Subduction Zone shows the potential to develop paleoseismic methods for the Sumatra and other subduction zones: Geophysical Research Abstracts, v. 7, no. 07269, p. 3.

Gutiérrez-Pastor, J., Nelson, C.H., Goldfinger, C., Johnson, J.E., Escutia, C., Eriksson, A.T., and Morey, A.E., 2009, Earthquake control of Holocene turbidite frequency confirmed by hemipelagic sedimentation chronology on the Cascadia and northern California active continental margins, *in* Kneller, B.C., et al., eds., External controls of deep-water depositional systems: Society for Sedimentary Geology (SEPM) Special Publication 92, p. 179–197, doi:10.2110/sepmsp.092.179.

Gutiérrez-Pastor, J., Nelson, C.H., Goldfinger, C., and Escutia, C., 2013, Sedimentology of seismo-turbidites off the Cascadia and northern California active tectonic continental margins, northwest Pacific Ocean: Marine Geology, v. 336, p. 99–119, doi:10.1016/j.margeo.2012.11.010.

Hagstrum, J.T., Atwater, B.F., and Sherrod, B.L., 2004, Paleomagnetic correlation of late Holocene earthquakes among estuaries in Washington and Oregon: Geochemistry, Geophysics, Geosystems, v. 5, Q10001, doi:10.1029/2004GC000736.

Hammond, D.E., McManus, J., Berelson, W.M., Kilgore, T.E., and Pope, R.H., 1996, Early diagenesis of organic material in equatorial Pacific sediments: stoichiometry and kinetics: Deep-Sea Research II, v. 43, p. 1365–1412, doi:10.1016/0967-0645(96)00027-6.

Hampton, M.A., Bouma, A.H., Carlson, P.R., Molnia, B.F., Clukey, E.C., and Sangrey, D.A., 1978, Quantitative study of slope instability in the Gulf of Alaska: Houston, Texas, Offshore Technology Conference, OTC-3314-MS, p. 2307–2318, doi:10.4043/3314-MS.

Hampton, M.A., Lee, H.J., and Locat, J., 1996, Submarine landslides: Reviews of Geophysics, v. 34, p. 33–59, doi:10.1029/95RG03287.

Hayes, G.P., Bergman, E., Johnson, K.L., Benz, H.M., Brown, L., and Meltzer, A.S., 2013, Seismotectonic framework of the 2010 February 27 M_w 8.8 Maule, Chile earthquake sequence: Geophysical Journal International, v. 195, p. 1034–1051, doi:10.1093/gji/ggt238.

Heki, K., and Mitsui, Y., 2013, Accelerated pacific plate subduction following interplate thrust earthquakes at the Japan trench: Earth and Planetary Science Letters, v. 363, p. 44–49, doi:10.1016/j.epsl.2012.12.031.

Hemphill-Haley, E., 1995, Diatom evidence for earthquake-induced subsidence and tsunami 300 yr ago in southern coastal Washington: Geological Society of America Bulletin, v. 107, p. 367–378, doi:10.1130/0016-7606(1995)107<0367:DEFEIS>2.3.CO;2.

Henkart, P., 2011, SIOSEIS—The introduction: Software package sponsored by the National Science Foundation and the Scripps Industrial Associates: http://sioseis.ucsd.edu/sioseis.html.

Henstock, T.J., McNeill, L.C., and Tappin, J.R., 2006, Seafloor morphology of the Sumatran subduction zone: Surface rupture during megathrust earthquakes?: Geology, v. 34, p. 485–488, doi:10.1130/22426.1.

Hindle, D., and Mackey, K., 2011, Earthquake recurrence and magnitude and seismic deformation of the northwestern Okhotsk plate, northeast Russia: Journal of Geophysical Research, v. 116, B02301, doi:10.1029/2010JB007409.

Geosphere, published online on 12 November 2015 as doi:10.1130/GES01066.1

Hok, S., Fukuyama, E., and Hashimoto, C., 2011, Dynamic rupture scenarios of anticipated Nankai-Tonankai earthquakes, southwest Japan: Journal of Geophysical Research, v. 116, B12319, doi:10.1029/2011JB008492.

Howard, A.D., 1994, A detachment-limited model of drainage basin evolution: Water Resources Research, v. 30, p. 2261–2285, doi:10.1029/94WR00757.

Howard, A.D., 1997, Badland morphology and evolution: Interpretation using a simulation model: Earth Surface Processes and Landforms, v. 22, p. 211–227, doi:10.1002/(SICI)1096-9837(199703)22:3<211::AID-ESP749>3.0.CO;2-E.

Hsu, Y.-j., Simons, M., Avouac, J., Galetzka, J., Sieh, K., Chlieh, M., Natawidjaja, D.H., Prawirodirdjo, L., and Bock, Y., 2006, Frictional afterslip following the 2005 Nias-Simeulue earthquake, Sumatra: Science, v. 312, p. 1921–1926, doi:10.1126/science.1126960.

Hua, Q., Woodroffe, C., Barbetti, M., Smithers, S., Zoppi, U., and Fink, D., 2004, Marine reservoir correction for the Cocos (Keeling) Islands, Indian Ocean: Radiocarbon, v. 46, p. 603–610.

Hughen, K., Lehman, S., Southon, J., Overpeck, J., Marchal, O., Herring, C., and Turnbull, J., 2004, ^{14}C activity and global carbon cycle changes over the past 50,000 years: Science, v. 303, p. 202–207, doi:10.1126/science.1090300.

Huh, C.A., Su, C.C., Liang, W.T., and Ling, C.Y., 2004, Linkages between turbidites in the southern Okinawa Trough and submarine earthquakes: Geophysical Research Letters, v. 31, L12304, doi:10.1029/2004GL019731.

Huh, C.-A., Su, C.-C., Wang, C.-H., Lee, S.-Y., and Lin, I.-T., 2006, Sedimentation in the Southern Okinawa Trough—Rates, turbidites and a sediment budget: Marine Geology, v. 231, p. 129–139, doi:10.1016/j.margeo.2006.05.009.

Ide, S., 2013, The proportionality between relative plate velocity and seismicity in subduction zones: Nature Geoscience, v. 6, p. 780–784, doi:10.1038/NGEO1901.

Ikehara, K., Kanamatsu, T., Strasser, M., Fink, H., Nagahashi, Y., Usami, K., and Wefer, G., 2012, Past "earthquaketsunami" event deposits found in the Japan Trench: Results from the Sonne SO219A and Mirai MR12–E01 cruises: American Geophysical Union, fall meeting, abs. NH41C–02.

Ikehara, K., Irino, T., Usami, K., Jenkins, R., Omura, A., and Ashi, J., 2014, Possible submarine tsunami deposits on the outer shelf of Sendai Bay, Japan resulting from the 2011 earthquake and tsunami off the Pacific coast of Tohoku: Marine Geology, v. 349, p. 91–98, doi:10.1016/j.margeo.2014.01.001.

Inouchi, Y., Kinugasa, Y., Kumon, F., Nakano, S., Yasumatsu, S., and Shiki, T., 1996, Turbidites as records of intense palaeoearthquakes in Lake Biwa: Japan: Sedimentary Geology, v. 104, p. 117–125, doi:10.1016/0037-0738(95)00124-7.

Ishii, M., Shearer, P.M., Houston, H., and Vidale, J.E., 2005, Extent, duration and speed of the 2004 Sumatra-Andaman earthquake imaged by the Hi-Net array: Nature, v. 435, p. 933–936, doi:10.1038/nature03675.

Ishii, M., Shearer, P.M., Houston, H., and Vidale, J.E., 2007, Teleseismic P wave imaging of the 26 December 2004 Sumatra-Andaman and 28 March 2005 Sumatra earthquake ruptures using the Hi-net array: Journal of Geophysical Research, v. 112, B11307, doi:10.1029/2006JB004700.

Izaguirre, C., Mendez, F.J., Mendez, M., and Losada, I.J., 2011, Global extreme wave height variability based on satellite data: Geophysical Research Letters, v. 38, L10607, doi:10.1029/2011GL047302.

Jacob, J., Dyment, J., and Yatheesh, V., 2014, Revisiting the structure, age, and evolution of the Wharton Basin to better understand subduction under Indonesia: Journal of Geophysical Research, v. 119, p. 1–22, doi:10.1002/2013JB010285.

Jankaew, K., Atwater, B.F., Sawai, Y., Charoentitirat, T., Martin, M.E., and Prendergast, A., 2008, Medieval forewarning of the 2004 Indian Ocean tsunami in Thailand: Nature, v. 455, p. 1228–1231, doi:10.1038/nature07373.

Johnson, J.E., Goldfinger, C., Trehu, A.M., Bangs, N.L.B., Torres, M.E., and Chevallier, J., 2005, North-south variability in the history of deformation and fluid venting across Hydrate Ridge, Cascadia Margin, *in* Tréhu, A.M., et al., eds., Proceedings of the Ocean Drilling Program, Scientific results, Volume 204: College Station, Texas, Ocean Drilling Program, p. 1–16, doi:10.2973/odp.proc.sr.204.125.2006

Kagan, Y.Y., Jackson, D.D., and Geller, R.J., 2012, Characteristic earthquake model, 1884–2011, R.I.P.: Seismological Research Letters, v. 83, p. 951–953, doi:10.1785/0220120107.

Kanamori, H., Rivera, L., and Lee, W.H.K., 2010, Historical seismograms for unravelling a mysterious earthquake: The 1907 Sumatra earthquake: Geophysical Journal International, v. 183, p. 358–374, doi:10.1111/j.1365-246X.2010.04731.x.

Karig, D.E., Lawrence, M.B., Moore, G.F., and Curray, J.R., 1980, Structural framework of the forearc basin, NW Sumatra: Journal of the Geological Society, London, v. 137, p. 77–91, doi:10.1144/gsjgs.137.1.0077.

Karlin, R.E., and Abella, S.E.B., 1992, Paleoearthquakes in the Puget Sound region recorded in sediments from Lake Washington, U.S.A.: Science, v. 258, p. 1617–1620, doi:10.1126/science.258.5088.1617.

Karlin, R.E., and Abella, S.E.B., 1996, A history of Pacific Northwest earthquakes recorded in Holocene sediments from Lake Washington: Journal of Geophysical Research, v. 101, no. B3, p. 6137–6150.

Karlin, R., and Seitz, G., 2007, Final Technical Report for 07HQGR0014 and 07HQGR0008: A basin wide record of earthquakes at Lake Tahoe: Validation of the earthquake induced turbidite model with sediment core analysis: Collaborative Research with UNR and SDSU: U.S. Geological Survey National Earthquake Hazards Reduction Program, 18 p.

Karlin, R.E., Holmes, M., Abella, S.E.B., and Sylwester, R., 2004, Holocene landslides and a 3500-year record of Pacific Northwest earthquakes from sediments in Lake Washington: Geological Society of America Bulletin, v. 116, p. 94–108, doi:10.1130/B25158.1.

Kastens, K.A., and Cita, M.B., 1981, Tsunami-induced sediment transport in the abyssal Mediterranean Sea: Geological Society of America Bulletin, v. 92, p. 845–857, doi:10.1130/0016-7606(1981)92<845:TSTITA>2.0.CO;2.

Kayen, R.E., and Mitchell, J.K., 1997, Assessment of liquefaction potential during earthquakes by Arias intensity: Journal of Geotechnical and Geoenvironmental Engineering, v. 123, p. 1162–1174, doi:10.1061/(ASCE)1090-0241(1997)123:12(1162).

Keefer, D.K., 1984, Landslides caused by earthquakes: Geological Society of America Bulletin, v. 95, p. 406–421, doi:10.1130/0016-7606(1984)95<406:LCBE>2.0.CO;2.

Kelsey, H.M., Witter, R.C., and Hemphill-Haley, E., 2002, Plate-boundary earthquakes and tsunamis of the past 5500 yr, Sixes River estuary, southern Oregon: Geological Society of America Bulletin, v. 114, p. 298–314, doi:10.1130/0016-7606(2002)114<0298:PBEATO>2.0.CO;2.

Kelsey, H.M., Nelson, A.R., Hemphill-Haley, E., and Witter, R.C., 2005, Tsunami history of an Oregon coastal lake reveals a 4600 yr record of great earthquakes on the Cascadia subduction zone: Geological Society of America Bulletin, v. 117, p. 1009–1032, doi:10.1130/B25452.1.

Kiser, E., and Ishii, M., 2011, The 2010 Mw 8.8 Chile earthquake: Triggering on multiple segments and frequency dependent rupture behavior: Geophysical Research Letters, v. 38, L07301, doi:10.1029/2011GL047140.

Klug, C., Cashman, K.V., and Bacon, C.R., 2002, Structure and physical characteristics of pumice from the climactic eruption of Mount Mazama (Crater Lake), Oregon: Bulletin of Volcanology, v. 34, p. 486–501, doi:10.1007/s00445-002-0230-5.

Kneller, B., and Buckee, C., 2000, The structure and fluid mechanics of turbidity currents: A review of some recent studies and their geological implications: Sedimentology, v. 47, p. 62–94, doi:10.1046/j.1365-3091.2000.047s1062.x.

Kneller, B., and McCaffrey, B., 1995, Modeling the effects of salt-induced topography on deposition from turbidity currents, *in* Travis, C., et al., eds., Gulf Coast Section Society of Economic Paleontologists and Mineralogists Foundation Sixteenth annual research conference: Houston, Texas, Gulf Coast Section Society of Economic Paleontologists Foundation, p. 137–145.

Kneller, B.C., and McCaffrey, W.D., 2003, The interpretation of vertical sequences in turbidite beds: The influence of longitudinal flow structure: Journal of Sedimentary Research, v. 73, p. 706–713, doi:10.1306/031103730706.

Komen, G.J., Cavaleri, L., Donelan, M., Hasselmann, K., Hasselmann, S., and Janssen, P.A.E.M., 1994, Dynamics and modeling of ocean waves: Cambridge, Cambridge University Press, 556 p.

Konca, A.O., Hjorleifsdottir, V., Song, T.A., Avouac, J., Helmberger, D., Ji, C., Briggs, R.W., and Meltzner, A.J., 2007, Rupture kinematics of the 2005 Mw 8.6 Nias–Simeulue earthquake from the joint inversion of seismic and geodetic data: Seismological Society of America Bulletin, v. 97, p. S307–S322, doi:10.1785/0120050632.

Konca, A.O., et al., 2008, Partial rupture of a locked patch of the Sumatra Megathrust during the 2007 earthquake sequence: Nature, v. 456, p. 631–635, doi:10.1038/nature07572.

Kopp, H., 2013The control of subduction zone structural complexity and geometry on margin segmentation and seismicity: Tectonophysics, v. 589, p. 1–16, doi:10.1016/j.tecto.2012.12.037.

Kopp, H., et al., 2008, Lower slope morphology of the Sumatra trench system: Basin Research, v. 20, p. 519–529, doi:10.1111/j.1365-2117.2008.00381.x.

Geosphere, published online on 12 November 2015 as doi:10.1130/GES01066.1

Kramer, S.L., and Lindwall, N.W., 2004, Dimensionality and directionality effects in Newmark sliding block analyses: Journal of Geotechnical and Geoenvironmental Engineering, v. 130, p. 303–315, doi:10.1061/(ASCE)1090-0241(2004)130:3(303).

Ladage, S., Weinrebe, W., Gaedicke, C., Barckhausen, U., Flueh, E.R., Heyde, I., Krabbenhoeft, A., Kopp, H., Fahar, S., and Djadjadihardja, Y., 2006, Bathymetric survey images structure off Sumatra: Eos (Transactions, American Geophysical Union), v. 87, p. 165–172.

Lamb, M.P., Tonolio, H., and Parker, G., 2006, Trapping of sustained turbidity currents by intra-slope minibasins: Sedimentology, v. 53, p. 147–160, doi:10.1111/j.1365-3091.2005.00754.x.

Lay, T., et al., 2005, The great Sumatra-Andaman earthquake of 26 December 2004: Science, v. 308, p. 1127–1133, doi:10.1126/science.1112250.

Lees, J.A., Flower, R.J., Ryves, D., Vologina, E., and Sturm, M., 1998a, Identifying sedimentation patterns in Lake Baikal using whole core and surface scanning magnetic susceptibility: Journal of Paleolimnology, v. 20, p. 187–202, doi:10.1023/A:1008043230549.

Lees, J.A., Fowler, R.J., and Appleby, P.G., 1998b, Mineral magnetic and physical properties of surficial sediments and onshore samples from the southern basin of Lake Baikal, Siberia: Journal of Paleolimnology, v. 20, p. 175–186, doi:10.1023/A:1008040824614.

Leonard, L.J., Hyndman, R.D., and Mazzotti, S., 2004, Coseismic subsidence in the 1700 great Cascadia earthquake: Coastal estimates versus elastic dislocation models: Geological Society of America Bulletin, v. 116, p. 655–670, doi:10.1130/B25369.1.

Leonard, L.J., Currie, C.A., Mazzotti, S., and Hyndman, R.D., 2010, Rupture area and displacement of past Cascadia great earthquakes from coastal coseismic subsidence: Geological Society of America Bulletin, v. 122, p. 1951–1968, doi:10.1130/B30108.1.

Levesque, C.L., Locat, J., and Leroueil, S., 2006, Dating submarine mass movements triggered by earthquakes in the Upper Saguenay Fjord, Quebec, Canada: Norwegian Journal of Geology, v. 86, p. 231–242.

Lorenzoni, L., Thunell, R.C., Benitez-Nelson, C.R., Hollander, D., Martinez, N., Tappa, E., Varela, R.N., Astor, Y., Muller-Karger, F.E., 2012, The importance of subsurface nepheloid layers in transport and delivery of sediments to the eastern Cariaco Basin, Venezuela: Deep-Sea Research I, v. 56, p. 2249–2262, doi:10.1016/j.dsr.2009.08.001.

Lovlie, R., and Van Veen, P., 1995, Magnetic susceptibility of a 180 m sediment core: Reliability of incremental sampling and evidence for a relationship between susceptibility and gamma activity, *in* Turner, P., and Turner, A., eds., Palaeomagnetic applications in hydrocarbon exploration and production: Geological Society, London, Special Publication 98, p. 259–266, doi:10.1144/GSL.SP.1995.098.01.16.

Lowe, D.R., 1982, Sediment gravity flows: II. Depositional models with special reference to the deposits of high-density turbidity currents: Journal of Sedimentary Petrology, v. 52, p. 279–297, doi:10.1306/212F7F31-2B24-11D7-8648000102C1865D.

Mahani, A.B., and Atkinson, G.M., 2013, Regional differences in ground-motion amplitudes of small-to-moderate earthquakes across North America: Seismological Society of America Bulletin, v. 103, p. 2604–2620, doi:10.1785/0120120350.

Major, C.O., Pirmez, C., Goldberg, D., and Party, L.S., 1998, High-resolution core-log integration techniques: Examples from the Ocean Drilling Program, *in* Harvey, P.K., and Lovell, M.A., eds., Core-log integration: Geological Society, London, Special Publication 136, p. 285–295, doi:10.1144/GSL.SP.1998.136.01.24.

Malik, J.N., Shishikura, M., Echigo, T., Ikeda, Y., Satake, K., Kayanne, H., Sawai, Y., Murty, C.V.R., and Dikshit, D., 2011, Geologic evidence for two pre-2004 earthquakes during recent centuries near Port Blair, South Andaman Island, India: Geology, v. 39, p. 559–562, doi:10.1130/G31707.1.

Martin, W.R., and Sayles, F.L., 2003, The recycling of biogenic material at the seafloor, *in* Mackenzie, F.T., ed., Treatise on Geochemistry Volume 7: Amsterdam, Elsevier, p. 37–65, doi:10.1016/B0-08-043751-6/07089-4.

Masson, D.G., Harbitz, C.B., Wynn, R.B., Pedersen, G., Løvholt, F., 2006, Submarine landslides: Processes, triggers and hazard prediction: Royal Society of London Philosophical Transactions, v. 364, p. 2009–2039, doi:10.1098/rsta.2006.1810.

Matson, R.G., and Moore, G., 1992, Structural influence on Neogene subsidence in the central Sumatra fore-arc basin: Southwest Pacific and eastern Indian Ocean margins, *in* Watkins, J.S., et al., eds., Geology and geophysics of continental margins: American Association of Petroleum Geologists Memoir 53, p. 157–181.

McCalpin, J.P., 2009, Field techniques in paleoseismology—Terrestrial environments, *in* McCalpin, J.P., ed., Paleoseismology: San Diego, California, Academic Press, p. 29–118.

McCalpin, J.P., and Nelson, A.R., 1996, Introduction to paleoseismology, *in* McCalpin, J.P., ed., Paleoseismology: San Diego, California, Academic Press, p. 1–32.

McGregor, H., Gagan, M., McCulloch, M., Hodge, E., and Mortimer, G., 2008, Mid-Holocene variability in the marine ^{14}C reservoir age for northern coastal Papua New Guinea: Quaternary Geochronology, v. 3, p. 213–225, doi:10.1016/j.quageo.2007.11.002.

McHugh, C.M.G., Seeber, L., Cormier, M.-H., Dutton, J., Çağatay, N., Polonia, A., Ryan, W.B.F., and Gorur, N., 2006, Submarine earthquake geology along the North Anatolia fault in the Marmara Sea, Turkey: A model for transform basin sedimentation: Earth and Planetary Science Letters, v. 248, p. 661–684, doi:10.1016/j.epsl.2006.05.038.

McHugh, C.M.G., Braudy, N., Çağatay, M.M., Sorlien, C., Cormier, M., Seeber, L., and Henry, P., 2014, Seafloor fault ruptures along the North Anatolia fault in the Marmara Sea, Turkey: Link with the adjacent basin turbidite record: Marine Geology, v. 353, p. 65–83, doi:10.1016/j.margeo.2014.03.005.

Meltzner, A.J., Sieh, K., Abrams, M., Agnew, D.C., Hudnut, K.W., Avouac, J.-P., and Natawidjaja, D.H., 2006, Uplift and subsidence associated with the great Aceh-Andaman earthquake of 2004: Journal of Geophysical Research, v. 111, B02407, doi:10.1029/2005JB003891.

Meltzner, A.J., Sieh, K., Chiang, H., Shen, C., Suwargadi, B.W., Natawidjaja, D.H., Philibosian, B., Briggs, R.W., and Galetzka, J., 2010, Coral evidence for earthquake recurrence and an A.D. 1390–1455 cluster at the south end of the 2004 Aceh-Andaman rupture: Journal of Geophysical Research, v. 115, B10402, doi:10.1029/2010JB007499.

Meltzner, A.J., Sieh, K., Chiang, H.-W., Shen, C.-C., Suwargadi, B.W., Natawidjaja, D.H., Philibosian, B., and Briggs, R.W., 2012, Persistent termini of 2004- and 2005-like ruptures of the Sunda megathrust: Journal of Geophysical Research, v. 117, B04405, doi:10.1029/2011JB008888.

Meltzner, A.J., Sieh, K., Chiang, H.-W., Wu, C.-C., Tsang, L.L.H., Shen, C.-C., Hill, E.M., Suwargadi, B.W., Natawidjaja, D.H., Philibosian, B., and Briggs, R.W., 2015, Time-varying interseismic strain rates and similar seismic ruptures on the Nias-Simeulue patch of the Sunda megathrust: Quaternary Science Reviews, v. 122, p. 258–281, doi:10.1016/j.quascirev.2015.06.003.

Meunier, P., Hovius, N., and Haines, A.J., 2007, Regional patterns of earthquake-triggered landslides and their relation to ground motion: Geophysical Research Letters, v. 34, L20408, doi:10.1029/2007GL031337.

Michels, K.H., Suckow, A., Breitzke, M., Kudrass, H.R., and Kottke, B., 2003, Sediment transport in the shelf canyon "Swatch of No Ground" (Bay of Bengal): Deep-Sea Research II, v. 50, p. 1003–1022, doi:10.1016/S0967-0645(02)00617-3.

Middleton, G.V., 1967, Experiments on density and turbidity currents 111: Deposition of sediment: Canadian Journal of Earth Sciences, v. 4, p. 475–505, doi:0.1139/e67-025.

Miyamoto, J., Sassa, S., and Sekiguchi, H., 2004, Progressive solidification of a liquefied sand layer during continued wave loading: Geotechnique, v. 54, p. 617–629, doi:10.1680/geot.2004.54.10.617.

Moernaut, J., Batist, M.D., Charlet, F., Heirman, K., Chapron, E., Pino, M., Brümmer, R., and Urrutia, R., 2007, Giant earthquakes in south-central Chile revealed by Holocene mass-wasting events in Lake Puyehue: Sedimentary Geology, v. 195, p. 239–256, doi:10.1016/j.sedgeo.2006.08.005.

Monecke, K., Anselmetti, F.S., Becker, A., Schnellmann, M., Sturm, M., and Giardini, D., 2006, Earthquake-induced deformation structures in lake deposits: A late Pleistocene to Holocene paleoseismic record for central Switzerland: Eclogae Geologicae Helvetiae, v. 99, p. 343–362, doi:10.1007/s00015-006-1193-x.

Monecke, K., Finger, W., Klarer, D., Kongo, W., McAdoo, B., Moore, A., Sudrajat, S., 2008, A 1,000-year sediment record of tsunami recurrence in northern Sumatra: Nature, v. 455, p. 1232–1234, doi:10.1038/nature07374.

Moore, D.G., Curray, J.R., and Emmell, F.J., 1976, Large submarine slide (olistostrome) associated with Sunda arc subduction zone, northeast Indian Ocean: Marine Geology, v. 21, p. 211–226, doi:10.1016/0025-3227(76)90060-8.

Moore, G.F., and Karig, D.E., 1980, Structural geology of Nias Island, Indonesia: Implications for subduction zone tectonics: Science, v. 280, p. 193–223, doi:10.2475/ajs.280.3.193.

Moreno, M.S., Bolte, J., Klotz, J., and Melnick, D., 2009, Impact of megathrust geometry on inversion of coseismic slip from geodetic data: Application to the 1960 Chile earthquake: Geophysical Research Letters, v. 36, L16310, doi:10.1029/2009GL039276.

Moreno, M.S., et al., 2011, Heterogeneous plate locking in the south-central Chile subduction zone: Building up the next great earthquake: Earth and Planetary Science Letters, v. 305, p. 413–424, doi:10.1016/j.epsl.2011.03.025.

Morgenstern, N.R., 1967, Submarine slumping and the initiation of turbidity currents, *in* Richards, A., ed., Marine géotechnique: Urbana, University of Illinois Press, p. 189–220.

Geosphere, published online on 12 November 2015 as doi:10.1130/GES01066.1

Mosher, D. C., Austin, J.A., Jr., Fisher, D., and Gulick, S.P.S., 2008, Deformation of the northern Sumatra accretionary prism from high-resolution seismic reflection profiles and ROV observations: Marine Geology, v. 252, p. 89–99.

Mosher, D.C., Moscardelli, L., Shipp, R.C., Chaytor, J.D., Baxter, C.D.P., Lee, H.J., and Urgeles, R., 2010, Submarine mass movements and their consequences, *in* Mosher, D.C., et al., eds., Submarine mass movements and their consequences: New York, Springer, p. 1–8.

Muck, M.T., and Underwood, M.B., 1990, Upslope flow of turbidity currents: A comparison among field observations, theory, and laboratory models: Geology, v. 18, p. 54–57, doi:10.1130/0091-7613(1990)018<0054:UFOTCA>2.3.CO;2.

Mulder, T., Syvitski, J.P.M., Migeon, S., Faugeres, J.-C., and Savoye, B., 2003, Marine hyperpycnal flows: initiation, behavior and related deposits. A review: Marine and Petroleum Geology, v. 20, p. 861–882, doi:10.1016/j.marpetgeo.2003.01.003.

Murray, J., and Segall, P., 2002, Testing time-predictable earthquake recurrence by direct measurement of strain accumulation and release: Nature, v. 419, p. 287–291, doi:10.1038/nature00984.

Nair, R.R., Buynevich, I., Goble, R.J., Srinivasan, P., Murthy, S.G.N., Kandipal, S.C., Lakshmi, C.S.V., and Trivedi, I.D., 2010, Subsurface images shed light on past tsunamis in India: Eos (Transactions, American Geophysical Union), v. 91, p. 489–490, doi:10.1029/2010EO500002.

Nakajima, T., 2000, Initiation processes of turbidity currents; implications for assessments of recurrence intervals of offshore earthquakes using turbidites: Geological Survey of Japan Bulletin, v. 51, p. 79–87.

Nakajima, T., and Kanai, Y., 2000, Sedimentary features of seismoturbidites triggered by the 1983 and older historical earthquakes in the eastern margin of the Japan Sea: Sedimentary Geology, v. 135, p. 1–19, doi:10.1016/S0037-0738(00)00059-2.

Natawidjaja, D.H., Sieh, K., Ward, S.N., Cheng, H., Edwards, R.L., Galetzka, J., and Suwargadi, B.W., 2004, Paleogeodetic records of seismic and aseismic subduction from central Sumatran microatolls, Indonesia: Journal of Geophysical Research, v. 109, B04306, doi:10.1029/2003JB002398.

Natawidjaja, D.H., Sieh, K., Chlieh, M., Galetzka, J., Suwargadi, B., Cheng, H., Edwards, R.L., Avouac, J., and Ward, S.N., 2006, Source parameters of the great Sumatran megathrust earthquakes of 1797 and 1833 inferred from coral microatolls: Journal of Geophysical Research, v. 111, B06403, doi:10.1029/2005JB004025.

Nelson, A.R., Kelsey, H.M., and Witter, R.C., 2006, Great earthquakes of variable magnitude at the Cascadia subduction zone: Quaternary Research, v. 65, p. 354–365, doi:10.1016/j.yqres.2006.02.009.

Nelson, C.H., 1968, Marine geology of Astoria deep-sea fan [Ph.D. thesis]: Corvallis, Oregon State University, 289 p.

Nelson, C.H., Kulm, L.D., Carlson, P.R., and Duncan, J.R., 1968, Mazama ash in the northeastern Pacific: Science, v. 161, p. 47–49, doi:10.1126/science.161.3836.47.

Nelson, C.H., Meyer, A.W., Thor, D., and Larsen, M., 1986, Crate Lake, Oregon: A restricted basin with base-of-slope aprons of nonchanellized turbidites: Geology, v. 14, p. 238–241, doi:10.1130/0091-7613(1986)14<238:CLOARB>2.0.CO;2.

Nelson, C.H., Pastor, J.G., Goldfinger, C., and Escutia, C., 2012, Great earthquakes along the western United States continental margin: Implications for hazards, stratigraphy and turbidite lithology: Natural Hazards and Earth System Sciences, v. 12, p. 3191–3208, doi:10.5194/nhess-12-3191-2012.

Newcomb, K.R., and McCann, W.R., 1987, Seismic history and seismotectonics of the Sunda Arc: Journal of Geophysical Research, v. 92, p. 421–439, doi:10.1029/JB092iB01p00421.

Newman, A.V., Hayes, G.P., Wei, Y., and Convers, J., 2011, The 25 October 2010 Mentawai tsunami earthquake, from real-time discriminants, finite-fault rupture, and tsunami excitation: Geophysical Research Letters, v. 38, L05302, doi:10.1029/2010GL046498.

Ni, S., Kanamori, H., and Helmberger, D., 2005,. Energy radiation from the Sumatra earthquake: Nature, v. 434, p. 582.

Ninis, D., Little, T.A., Van Dissen, R.J., Litchfield, N.J., Smith, E.G.C., Wang, N., Reiser, U., and Henderson, C.M., 2013, Slip rate on the Wellington fault, New Zealand, during the late Quaternary: Evidence for variable slip during the Holocene: Seismological Society of America Bulletin, v. 103, p. 559–579, doi:10.1785/0120120162.

Nittrouer, C.A., 1978, Detrital sediment accumulation in a continental shelf environment of the Washington shelf [Ph.D. thesis]: Seattle, University of Washington, 243 p.

Noda, A., 2004, Turbidites along Kushiro Canyon, *in* Satake, K., and Goldfinger, C., eds., Workshop on turbidites as earthquake recorders: Tsukuba, Geological Survey of Japan.

Noda, A., Tuzino, T., Kanai, Y., Furukawa, R., and Uchida, J.-I., 2008, Paleoseismicity along the southern Kuril Trench deduced from submarine-fan turbidites: Marine Geology, v. 254, p. 73–90, doi:10.1016/j.margeo.2008.05.015.

Noller, J.S., 2000, Lead-210 geochronology, *in* Noller, J.S., et al., eds., Quaternary geochronology: American Geophysical Union Reference Shelf 4, p. 115–120.

Obermeier, S.F., and Dickenson, S.E., 2000, Liquefaction evidence for the strength of ground motions resulting from late Holocene Cascadia subduction earthquakes, with emphasis on the event of 1700 A.D: Seismological Society of America Bulletin, v. 90, p. 876–896, doi:10.1785/0119980179.

O'Connor, S., Ulm, S., Fallon, S., Barham, A., and Loch, I., 2010, Pre-bomb marine reservoir variability in the Kimberley region, Western Australia: Radiocarbon, v. 52, p. 1158–1165.

Park, J., et al., 2005, Earth's free oscillations excited by the 26 December 2004 Sumatra-Andaman earthquake: Science, v. 308, p. 1139–1144, doi:10.1126/science.1112305.

Parsons, T., 2012, Paleoseismic interevent times interpreted for an unsegmented earthquake rupture forecast: Geophysical Research Letters, v. 39, L13302, doi:10.1029/2012GL052275.

Parsons, T., Console, R., Falcone, G., Murru, M., and Yamashima, K., 2012, Comparison of characteristic and Gutenberg-Richter models for time-dependent M ≥ 7.9 earthquake probability in the Nankai-Tokai subduction zone, Japan: Geophysical Journal International, v. 190, p. 1673–1688, doi:10.1111/j.1365-246X.2012.05595.x.

Patton, J.R., Goldfinger, C., Djadjadihardja, Y., Udrekh, and Shipboard Scientific Party, 2007, Roger Revelle Cruise RR0705 Superquakes07 Cruise Report: Oregon State University, Active Tectonics Laboratory; Agency for the Assessment and Application of Technology, Indonesia (BPPT), 66 p.

Patton, J.R., Goldfinger, C., Morey, A., Romsos, C., Black, B., Djadjadihardja, Y., and Udrekh, 2013a, Seismoturbidite record as preserved at core sites at the Cascadia and Sumatra-Andaman subduction zones: Natural Hazards and Earth System Sciences, v. 13, p. 833–867, doi:10.5194/nhess-13-833-2013.

Patton, J.R., Goldfinger, C., Djadjadihardja, Y., and Udrekh, 2013b, Slope stability: Factor of safety along the seismically active continental slope offshore Sumatra: American Geophysical Union, fall meeting, abs. T23I–03.

Peduzzi, P., Chatenoux, B., Dao, H., De Bono, A., Herold, C., Kossin, J., Mouton, F., and Nordbeck, O., 2012, Global trends in tropical cyclone risk: Nature Climate Change, v. 2, p. 289–294, doi:10.1038/nclimate1410.

Peterson, C.D., and Madin, I.P., 1997, Coseismic paleoliquefaction evidence in the central Cascadia margin, USA: Oregon Geology, v. 59, p. 51–74.

Philibosian, B., Sieh, K., Natawidjaja, D.H., Chiang, H., Shen, C., Suwargadi, B., Hill, E.M., and Edwards, R.L., 2012, An ancient shallow slip event on the Mentawai segment of the Sunda megathrust, Sumatra: Journal of Geophysical Research, v. 117, B05401, doi:10.1029/2011JB009075.

Philibosian, B., Sieh, K., Avouac, J., Natawidjaja, D.H., Chiang, H., Wu, C., Perfettini, H., Shen, C., Daryono, M., and Suwargadi, B., 2014, Rupture and variable coupling behavior of the Mentawai segment of the Sunda megathrust during the supercycle culmination of 1797 to 1833: Journal of Geophysical Research, v. 119, p. 7258–7287, doi:10.1002/2014JB011200.

Piper, D.J.W., 1978, Turbidite muds and silts on deep-sea fans and abyssal plains, *in* Stanley, D.J., and Kelling, G., eds., Sedimentation in submarine canyons, fans and trenches: Stroudsburg, Pennsylvania, Dowden, Hutchinson & Ross, p. 163–176.

Piper, D.J.W., Cochonat, P., and Morrison, M.L., 1999, The sequence of events around the epicentre of the 1929 Grand Banks earthquake: Initiation of debris flows and turbidity current inferred from sidescan sonar: Sedimentology, v. 46, p. 79–97, doi:10.1046/j.1365-3091.1999.00204.x.

Polonia, A., Romano, S., Çağatay, M.N., Capotondi, L., Gasparotto, G., Gasperini, L., Panieri, G., and Torelli, L., 2015, Are repetitive slumpings during sapropel S1 related to paleo-earthquakes?: Marine Geology, v. 361, p. 41–52, doi:10.1016/j.margeo.2015.01.001.

Polonia, A., Bonatti, E., Camerlenghi, A., Lucchi, R.G., Panieri, G., and Gasperini, L., 2013a, Mediterranean megaturbidite triggered by the AD 365 Crete earthquake and tsunami: Scientific Reports, v. 3, 1285, doi:10.1038/srep01285.

Polonia, A., Panieri, G., and Gasperini, L., 2013b, Turbidite paleoseismology in the Calabrian Arc subduction complex (Ionian Sea): Geochemistry, Geophysics, Geosystems, v. 14, p. 112–140, doi:10.1029/2012GC004402.

Pouderoux, H., Proust, J.-N., Lamarche, G., Orpin, A., and Neil, H., 2012, Postglacial (after 18 ka) deep-sea sedimentation along the Hikurangi subduction margin (New Zealand): Character-

Geosphere, published online on 12 November 2015 as doi:10.1130/GES01066.1

isation, timing and origin of turbidites: Marine Geology, v. 295–298, p. 51–76, doi:10.1016/j.margeo.2011.11.002.

Prell, W.L., Imbrie, J., Martinson, D.G., Morley, J.J., Pisias, N.G., Shackleton, N.J., and Streeter, H.F., 1986, Graphic correlation of oxygen isotope stratigraphy application to the late Quaternary: Paleoceanography, v. 1, p. 137–162, doi:10.1029/PA001i002p00137.

Rajendran, C. P., Rajendran, K., Machado, T., Satyamurthy, T., Aravazhi, P., and Jaiswal, M., 2006, Evidence of ancient sea surges at the Mamallapuram coast of India and implications for previous Indian Ocean tsunami events: Current Science, v. 91, no. 9, p. 1242–1247.

Rajendran, C.P., Rajendran, K., Anu, R., Earnest, A., Machado, T., Mohan, P.M., and Freymueller, J., 2007, Crustal deformation and seismic history associated with the 2004 Indian Ocean earthquake: A perspective from the Andaman–Nicobar Islands: Seismological Society of America Bulletin, v. 97, p. S174–S191, doi:10.1785/0120050630.

Rajendran, K., Rajendran, C.P., Earnest, A., Ravi Prasad, G.V., Dutta, K., Ray, D.K., and Anu, R., 2008, Age estimates of coastal terraces in the Andaman and Nicobar Islands and their tectonic implications: Tectonophysics, v. 455, p. 53–60, doi:10.1016/j.tecto.2008.05.004.

Rajendran, C.P., Rajendran, K., Andrade, V., and Srinivasalu, S., 2013, Ages and relative sizes of pre-2004 tsunamis in the Bay of Bengal inferred from geologic evidence in the Andaman and Nicobar Islands: Journal of Geophysical Research, v. 118, p. 1–18, doi:10.1029/2012JB009541.

Rampino, M.R., 1984, Terrestrial mass extinctions, cometary impacts and the sun's motion perpendicular to the galactic plane: Nature, v. 308, p. 709–712, doi:10.1038/308709a0.

Rampino, M.R., 1999, Impact crises, mass extinctions, and galactic dynamics: The case for a unified theory, *in* Dressler, B.O., and Sharpton, V.L., eds., Large meteorite impacts and planetary evolution; II: Geological Society of America Special Paper 339, p. 241–248, doi:10.1130/0-8137-2339-6.241.

Rampino, M.R., 2002, Role of the galaxy in periodic impacts and mass extinctions on the Earth, *in* Koeberl, C., and MacLeod, K., eds., Catastrophic events and mass extinctions: Impacts and beyond: Geological Society of America Special Paper 356, p. 667–678, doi:10.1130/0-8137-2356-6.667.

Rampino, M.R., and Stothers, R.B., 1984, Geological rhythms and cometary impacts: Science, v. 226, p. 1427–1431, doi:10.1126/science.226.4681.1427.

Ratzov, G., Collot, J.-Y., Sosson, M., and Migeon, S., 2010, Mass-transport deposits in the northern Ecuador subduction trench: Result of frontal erosion over multiple seismic cycles: Earth and Planetary Science Letters, v. 296, p. 89–102, doi:10.1016/j.epsl.2010.04.048.

Reimer, P.J., et al., 2009, INTCAL09 and MARINE09 radiocarbon age calibration curves, 0–50,000 years cal BP: Radiocarbon, v. 51, p. 1111–1150,.

Reimer, P.J., et al., 2013, IntCal13 and Marine13 radiocarbon age calibration curves 0–50,000 years cal BP: Radiocarbon, v. 55, p. 1869–1887, doi:10.2458/azu_js_rc.55.16947.

Rhodes, B.P., Kirby, M.E., Jankaew, K., and Choowong, M., 2011, Evidence for a mid-Holocene tsunami deposit along the Andaman coast of Thailand preserved in a mangrove environment: Marine Geology, v. 282, p. 255–267, doi:10.1016/j.margeo.2011.03.003.

Rivera, L., Sieh, K., Helmberger, D., and Natawidjaja, D.H., 2002, A comparative study of the Sumatran subduction-zone earthquakes of 1935 and 1984: Seismological Society of America Bulletin, v. 92, p. 1721–1736, doi:10.1785/0120010106.

Robbins, J.A., Edgington, D.N., and Kemp, A.L.W., 1978, Comparative ^{210}Pb, ^{137}Cs, and pollen geochronologies of sediments from Lakes Ontario and Erie: Quaternary Research, v. 10, p. 256–278, doi:10.1016/0033-5894(78)90105-9.

Robison, W.L., Conrado, C.L., Bogen, K.T., and Stoker, A.C., 2003, The effective and environmental half-life of ^{137}Cs at Coral Islands at the former US nuclear test site: Journal of Environmental Radioactivity, v. 69, p. 207–223, doi:10.1016/S0265-931X(03)00080-8.

Rong, Y., Jackson, D.D., Magistrale, H., and Goldfinger, C., 2014, Magnitude limits of subduction zone earthquakes: Seismological Society of America Bulletin, v. 104, p. 2359–2377, doi:10.1785/0120130287.

Ross, D.A., 1971, Mass physical properties and slope stability of sediments of the northern Middle America Trench: Journal of Geophysical Research, v. 76, p. 704–712, doi:10.1029/JC076i003p00704.

Ruff, L., and Kanamori, H., 1980, Seismicity and the subduction process: Physics of the Earth and Planetary Interiors, v. 23, p. 240–252, doi:10.1016/0031-9201(80)90117-X.

Salisbury, M., Kent, A., Patton, J., Goldfinger, C., Djadjadihardja, Y., and Udrekh, U., 2010, Deep-sea ash layers reveal evidence of large Pleistocene and Holocene volcanic eruptions from Sumatra, Indonesia: American Geophysical Union, fall meeting, abs. V11D–2330.

Salisbury, M., Patton, J., Kent, A., Goldfinger, C., Djadjadihardja, Y., and Udrekh, U., 2012, Newly discovered deep-sea ash layers reveal evidence of large Holocene volcanic eruptions from Sumatra, Indonesia: Journal of Volcanology and Geothermal Research, v. 231–232, p. 61–71, doi:10.1016/j.jvolgeores.2012.03.007.

Sarı, E., and Çağatay, M., 2006, Turbidites and their association with past earthquakes in the deep Çınarcık Basin of the Marmara Sea: Geo-Marine Letters, v. 26, p. 69–76, doi:10.1007/s00367-006-0017-3.

Satake, K., and Atwater, B., 2007, Long-term perspectives on giant earthquakes and tsunamis at subduction zones: Annual Review of Earth and Planetary Sciences, v. 35, p. 349–374, doi:10.1146/annurev.earth.35.031306.140302.

Sayles, F.L., Martin, W.R., and Deuser, W.G., 1994, Response of benthic oxygen demand to particulate organic carbon supply in the deep sea near Bermuda: Nature, v. 371, p. 686–689, doi:10.1038/371686a0.

Sayles, F.L., Martin, W.R., Chase, Z., and Anderson, R.F., 2001, Benthic remineralization and burial of biogenic SiO_2, $CaCO_3$, organic carbon, and detrital material in the Southern Ocean along a transect at 170° west: Deep-Sea Research, Part II, Topical Studies in Oceanography, v. 48, p. 4323–4383, doi:10.1016/S0967-0645(01)00091-1.

Schlagenhauf, A., Manighetti, I., Benedetti, L., Gaudemer, Y., Finkel, R., Malavieille, J., and Pou, K., 2011, Earthquake supercycles in central Italy, inferred from ^{36}Cl exposure dating: Earth and Planetary Science Letters, v. 307, p. 487–500, doi:10.1016/j.epsl.2011.05.022.

Schulz, W.H., Galloway, S.L., and Higgins, J.D., 2012, Evidence for earthquake triggering of large landslides in coastal Oregon, USA: Geomorphology, v. 141–142, p. 88–98, doi:10.1016/j.geomorph.2011.12.026.

Schurr, B., Asch, G., Rosenau, M., Wang, R., Oncken, O., Barrientos, D.E., Salazar, P., and Vilotte, J.P., 2007, The 2007 M7.7 Tocopilla northern Chile earthquake sequence: Implications for along-strike and downdip rupture segmentation and megathrust frictional behavior: Journal of Geophysical Research, v. 117, B05305, doi:10.1029/2011JB009030.

Scott, E.M., 2003, The Fourth International Radiocarbon Intercomparison (FIRI): Radiocarbon, v. 45, p. 135–285.

Seilacher, A., 1969, Fault-graded beds interpreted as seismites: Sedimentology, v. 13, p. 155–159, doi:10.1111/j.1365-3091.1969.tb01125.x.

Shanmugam, G., 2008, The constructive functions of tropical cyclones and tsunamis on deep-water sand deposition during sea level highstand: Implications for petroleum exploration: American Association of Petroleum Geologists Bulletin, v. 92, p. 443–471, doi:10.1306/12270707101.

Shiki, T., 1996, Reading of the trigger records of sedimentary events—A problem for future studies: Sedimentary Geology, v. 104, p. 249–255, doi:10.1016/0037-0738(95)00132-8.

Shiki, T., Kumon, F., Inouchi, Y., Kontani, Y., Sakamoto, T., Tateishi, M., Matsubara, H., and Fukuyama, K., 2000, Sedimentary features of the seismo-turbidites, Lake Biwa, Japan: Sedimentary Geology, v. 135, p. 37–50, doi:10.1016/S0037-0738(00)00061-0.

Shimazaki, K., and Nakata, T., 1980, Time-predictable recurrence model for large earthquakes: Geophysical Research Letters, v. 7, p. 279–282, doi:10.1029/GL007i004p00279.

Shirai, M., Omura, A., Wakabayashi, T., Uchida, J.-i., and Ogami, T., 2010, Depositional age and triggering event of turbidites in the western Kumano Trough, central Japan during the last ca. 100 years: Marine Geology, v. 271, p. 225–235, doi:10.1016/j.margeo.2010.02.015.

Sieh, K., and Natawidjaja, D., 2000, Neotectonics of the Sumatran fault: Journal of Geophysical Research, v. 105, no. B12, p. 28,295–28,326, doi:10.1029/2000JB900120.

Sieh, K., Natawidjaja, D.H., Meltzner, A.J., Shen, C., Cheng, H., Li, K., Suwargadi, B.W., Galetzka, J., Philibosian, B., and Edwards, R.L., 2008, Earthquake supercycles inferred from sea-level changes recorded in the corals of West Sumatra: Science, v. 322, p. 1674–1678, doi:10.1126/science.1163589.

Smith, K.L., 1987, Food energy supply and demand: A discrepancy between particulate organic carbon flux and sediment community oxygen consumption in the deep ocean: Limnology and Oceanography, v. 32, p. 201–220, doi:10.4319/lo.1987.32.1.0201.

Smith, S., Karlin, R.E., Kent, G.M., Seitz, G.G., and Driscoll, N.W., 2013, Holocene subaqueous paleoseismology of Lake Tahoe: Geological Society of America Bulletin, v. 125, p. 691–708, doi:10.1130/B30629.1.

Smith, W.H.F., and Sandwell, D.T., 1997, Global seafloor topography from satellite altimetry and ship depth soundings: Science, v. 277, p. 1956–1962, doi:10.1126/science.277.5334.1956.

Song, T.-R.A., and Simons, M., 2003, Large trench-parallel gravity variations predict seismogenic behavior in subduction zones: Science, v. 301, p. 630–633, doi:10.1126/science.1085557.

Sorensen, M.B., Atakan, K., and Pulido, N., 2007, Simulated strong ground motions for the great M 9.3 Sumatra–Andaman earthquake of 26 December 2004: Seismological Society of America Bulletin, v. 97, p. S139–S151, doi:10.1785/0120050608.

Geosphere, published online on 12 November 2015 as doi:10.1130/GES01066.1

Southon, J., Kashgarian, M., Fontugne, M., Metivier, B., and Yim, W.W.-S., 2002, Marine reservoir corrections for the Indian Ocean and Southeast Asia: Radiocarbon, v. 44, p. 167–180.

Squire, P., Joannes-Boyau, R., Scheffers, A.M., Nothdurft, L.D., Hua, Q., Collins, L.B., Scheffers, S.R., and Zhao, J., 2013, A marine reservoir correction for the Houtman-Abrolhos Archipelago, East Indian Ocean, Western Australia: Radiocarbon, v. 55, p. 103–114, doi:10.2458/azu_js_rc.v55i1.16197.

Stein, S., and Okal, E., 2007, Ultralong period seismic study of the December 2004 Indian Ocean earthquake and implications for regional tectonics and the subduction process: Seismological Society of America Bulletin, v. 97, p. S279–S295, doi:10.1785/0120050617.

St-Onge, G., Mulder, T., Piper, D.J.W., Hillaire-Marcel, C., and Stoner, J.S., 2004, Earthquake and flood-induced turbidites in the Saguenay Fjord (Québec): A Holocene paleoseismicity record: Quaternary Science Reviews, v. 23, p. 283–294, doi:10.1016/j.quascirev.2003.03.001.

St-Onge, G., et al., 2012, Comparison of earthquake-triggered turbidites from the Saguenay (eastern Canada) and Reloncavi (Chilean margin) fjords: Implications for paleoseismicity and sedimentology: Sedimentary Geology, v. 243–244, p. 89–107, doi:10.1016/j.sedgeo.2011.11.003.

Stow, D.A.V., 1977, Late Quaternary stratigraphy and sedimentation on the Nova Scotian outer continental margin [Ph.D. thesis]: Halifax, Nova Scotia, Dalhousie University, 360 p.

Stow, D.A.V., 1985, Deep-sea clastics: Where are we and where are we going?, *in* Brenchley, P.J., and Williams, B.P.J., eds., Sedimentology recent developments and applied aspects: Geological Society, London, Special Publication 18, p. 67–93, doi:10.1144/GSL.SP.1985.018.01.05.

Stow, D.A.V., and Bowen, A.J., 1980, A physical model for the transport and sorting of fine-grained sediment by turbidity currents: Sedimentology, v. 27, p. 31–46, doi:10.1111/j.1365-3091.1980.tb01156.x.

Stow, D.A.V., and Piper, D.J.W., 1984, Deep-water fine-grained sediments: Facies models, *in* Stow, D.A.V., and Piper, D.J.W., eds., Fine-grained sediments: Deep-water processes and facies: Geological Society, London, Special Publication 15, p. 611–646, doi:10.1144/GSL.SP.1984.015.01.38.

Stow, D.A.V., Amano, K., Balson, P.S., Brass, G.W., Corrigan, J., Raman, C.V., Tiercelin, J.-J., Townsend, M., and Wijayananda, N.P., 1990, Sediment facies and processes on the distal Bengal Fan, Leg 116, *in* Cochran, J.R., et al., Proceedings of the Ocean Drilling Program, Scientific results, Volume 116: College Station, Texas, Ocean Drilling Program, p. 377–396, doi:10.2973/odp.proc.sr.116.110.1990.

Stuiver, M., and Braziunas, T.F., 1993, Modeling atmospheric ^{14}C influences and ^{14}C ages of marine samples to 10,000 BC: Radiocarbon, v. 35, p. 137–189.

Stuiver, M., and Polach, H.A., 1977, Discussion: Reporting of 14C data: Radiocarbon, v. 19, p. 355–363.

Stuiver, M., Reimer, P.J., and Braziunas, T.F., 1998, High precision radiocarbon age calibration for terrestrial and marine samples: Radiocarbon, v. 40, p. 1127–1151.

Subarya, C., Chlieh, M., Prawirodirdjo, L., Avouac, J., Bock, Y., Sieh, K., Meltzner, A.J., Natawidjaja, D.H., and McCaffrey, R., 2006, Plate-boundary deformation associated with the great Sumatra–Andaman earthquake: Nature, v. 440, p. 46–51, doi:10.1038/nature04522.

Sultan, N., et al., 2004, Triggering mechanisms of slope instability processes and sediment failures on continental margins: A geotechnical approach: Marine Geology, v. 213, p. 291–321, doi:10.1016/j.margeo.2004.10.011.

Sultan, N., Cattaneo, A., Sibuet, J.-C., and Schneider, J.-L., 2009, Deep sea in situ excess pore pressure and sediment deformation off NW Sumatra and its relation with the December 26, 2004 Great Sumatra–Andaman earthquake: International Journal of Earth Sciences, v. 98, p. 823–837, doi:10.1007/s00531-008-0334-z.

Sumner, E., Siti, M., McNeil, L.C., Talling, P.J., Henstock, T., Wynn, R., Djadjadihardja, Y., and Permana, H., 2013, Can turbidites be used to reconstruct a paleoearthquake record for the central Sumatran margin?: Geology, v. 41, p. 763–766, doi:10.1130/G34298.1.

Susilohadi, S., Gaedickea, C., and Ehrhardt, A., 2005, Neogene structures and sedimentation history along the Sunda forearc basins off southwest Sumatra and southwest Java: Marine Geology, v. 219, p. 133–154, doi:10.1016/j.margeo.2005.05.001.

Syvitski, J.P.M., and Schafer, C.T., 1996, Evidence for an earthquake-triggered basin collapse in Saguenay Fjord, Canada: Sedimentary Geology, v. 104, p. 127–153, doi:10.1016/0037-0738(95)00125-5.

Talling, P.J., 2014, On the triggers, resulting flow types and frequencies of subaqueous sediment density flows in different settings: Marine Geology, v. 352, p. 155–182, doi:10.1016/j.margeo.2014.02.006.

Tanioka, Y., and Ruff, L.J., 1997, Source time functions: Seismological Research Letters, v. 68, p. 386–400, doi:10.1785/gssrl.68.3.386.

Tappin, D. R., McNeil, L. C., Henstock, T., and Mosher, D. C., 2007, Mass Wasting Processes—Offshore Sumatra, p. 327-336 in: Springer, Submarine Mass Movements and Their Consequences: 3rd International Symposium, 10 p.

Tearpock, D.J., and Bischke, R.E., 2002, Applied subsurface geological mapping: Englewood Cliffs, New Jersey, Prentice-Hall, Inc., 864 p.

Thompson, R., and Morton, D.J., 1979, Magnetic susceptibility and particle-size distribution in recent sediments of the Loch Lomond drainage basin, Scotland: Journal of Sedimentary Petrology, v. 49, p. 801–812, doi:10.1306/212F7851-2B24-11D7-8648000102C1865D.

Thomson, R.E., Davis, E.E., Heesemann, M., and Villinger, H., 2010, Observations of long-duration episodic bottom currents in the Middle America Trench: Evidence for tidally initiated turbidity flows: Journal of Geophysical Research, v. 115, C10020, doi:10.1029/2010JC006166.

Tolstoy, M., and Bohnenstiehl, D.R., 2006, Hydroacoustic contributions to understanding the December 26th 2004 great Sumatra–Andaman earthquake: Surveys in Geophysics, v. 27, p. 633–646, doi:10.1007/s10712-006-9003-6.

Travasarou, T., Bray, J.D., and Abrahamson, N.A., 2003, Empirical attenuation relationship for Arias intensity: Earthquake Engineering and Structural Dynamics, v. 32, p. 1133–1155, doi:10.1002/eqe.270.

Underwood, M.B., Hoke, K.D., Fisher, A.T., Davis, E.E., Giambalvo, E., Hlsdorff, L.Z., and Spinelli, G.A., 2005, Provenance, stratigraphic architecture, and hydrogeologic influence of turbidites on the mid-ocean ridge flank of northwestern Cascadia Basin, Pacific Ocean: Journal of Sedimentary Research, v. 75, p. 149–164, doi:10.2110/jsr.2005.012.

Van Daele, M., Gnudde, V., Duyck, P., Pino, M., Urrutia, R., and De Batist, M., 2014, Multidirectional, synchronously-triggered seismo-turbidites and debrites revealed by X-ray computed tomography (CT): Sedimentology, v. 61, p. 861–880, doi:10.1111/sed.12070.

Van Daele, M., Moernaut, J., Doom, L., Boes, R., Hebbeln, D., Pino, M., Urrutia, R., Brümmer, R., and De Batist, M., 2015, A comparison of the sedimentary records of the 1960 and 2010 great Chilean earthquakes in 17 lakes: Implications for quantitative lacustrine palaeoseismology: Sedimentology, doi:10.1111/sed.12193.

van der Lingen, G.J., 1969, The turbidite problem: New Zealand Journal of Geology and Geophysics, v. 12, p. 7–50, doi:10.1080/00288306.1969.10420225.

Völker, D., Reichel, T., Wiedicke, M., and Heubeck, C., 2008, Turbidites deposited on Southern Central Chilean seamounts: Evidence for energetic turbidity currents: Marine Geology, v. 251, p. 15–31, doi:10.1016/j.margeo.2008.01.008.

Waldmann, N., Anselmetti, F.S., Ariztegui, D., Austin, J.A., Jr., Pirouz, M., Moy, C.M., and Dunbar, R.B., 2011, Holocene mass-wasting events in Lago Fagnano, Tierra del Fuego (54°S): Implications for paleoseismicity of the Magallanes-Fagnano transform fault: Basin Research, v. 23, p. 171–190, doi:10.1111/j.1365-2117.2010.00489.x.

Wang, X., and Liu, P.L., 2006, An analysis of 2004 Sumatra earthquake fault plane mechanisms and Indian Ocean tsunami: Journal of Hydraulic Research, v. 44, p. 147–154, doi:10.1080/00221686.2006.9521671.

Ward, S.N., 2002, Planetary cratering: A probabilistic approach: Journal of Geophysical Research, v. 107, p. 7-1–7-11, doi:10.1029/2000JE001343.

Weiss, R., 2008, Sediment grains moved by passing tsunami waves: Tsunami deposits in deep water: Marine Geology, v. 250, p. 251–257, doi:10.1016/j.margeo.2008.01.018.

Wells, R.E., Blakely, R.J., Sugiyama, Y., Scholl, D.W., and Dinterman, P.A., 2003, Basin-centered asperities in great subduction zone earthquakes: A link between slip, subsidence, and subduction erosion: Journal of Geophysical Research, v. 108, 2507, doi:10.1029/2002JB002072.

Wesnousky, S.G., 1994, The Gutenberg-Richter or characteristic earthquake distribution, which is it?: Seismological Society of America Bulletin, v. 84, p. 1940–1959.

Wesnousky, S.G., 2008, Displacement and geometrical characteristics of earthquake surface ruptures: Issues and implications for seismic-hazard analysis and the process of earthquake rupture: Seismological Society of America Bulletin, v. 98, p. 1609–1632.

Wheatcroft, R.A., and Sommerfield, C.K., 2005, River sediment flux and shelf accumulation rates on the Pacific Northwest margin: Continental Shelf Research, v. 25, p. 311–332, doi:10.1016/j.csr.2004.10.001.

Wilson, C., and Keefer, D.K., 1985, Predicting areal limits of earthquake-induced landsliding, *in* Ziony, J.I., ed., Evaluating earthquake hazards in the Los Angeles region; an earth-science perspective: U.S. Geological Survey Professional Paper 1360, p. 317–345.

Wilson, R.C., 1993, Relation of Arias intensity to magnitude and distance in California: U.S. Geological Survey Open-File Report 93-556, 45 p.

Geosphere, published online on 12 November 2015 as doi:10.1130/GES01066.1

Wilson, T.R.S., Thomson, J., Colley, S., Hydes, D.J., Higgs, N.C., and Sørensen, J., 1985, Early organic diagenesis: The significance of progressive subsurface oxidation fronts in pelagic sediments: Geochimica et Cosmochimica Acta, v. 49, p. 811–822, doi:10.1016/0016-7037(85)90174-7.

Wiseman, K., and Bürgmann, R., 2011, Stress and seismicity changes on the Sunda megathrust preceding the 2007 Mw 8.4 earthquake: Seismological Society of America Bulletin, v. 101, p. 313–326, doi:10.1785/0120100063.

Witter, R.C., Zhang, Y., Wang, K., Priest, G.R., Goldfinger, C., Stimely, L.L., English, J.T., and Ferro, P.A., 2011, Simulating tsunami inundation at Bandon, Coos County, Oregon, using hypothetical Cascadia and Alaska earthquake scenarios: Oregon Department of Geology and Mineral Industries Special Paper 43, 63 p.

Witter, R.C., Zhang, Y.J., Wang, K., Priest, G., Goldfinger, C., Stimely, L., English, J., and Ferro, P., 2013, Simulated tsunami inundation for a range of Cascadia megathrust earthquake scenarios at Bandon, Oregon, USA: Geosphere, v. 9, p. 1783–1803, doi:10.1130/GES00899.1.

Young, I.R., 1999, Seasonal variability of the global ocean wind and wave climate: International Journal of Climatology, v. 19, p. 931–950, doi:10.1002/(SICI)1097-0088(199907)19:9<931::AID-JOC412>3.0.CO;2-O.

Youngs, R.R., Chiou, S.J., Silva, W.J., and Humphrey, J.R., 1997, Strong ground motion attenuation relationships for subduction zone earthquakes: Seismological Research Letters, v. 68, p. 58–73, doi:10.1785/gssrl.68.1.58.

Yu, K., Hua, Q., Zhao, J.-X., Hodge, E., Fink, D., and Barbetti, M., 2010, Holocene marine ^{14}C reservoir age variability: Evidence from ^{230}Th-dated corals from South China Sea: Paleoceanography, v. 25, PA3205, doi:10.1029/2009PA001831.

Zdanowicz, C.M., Zielinski, G.A., and Germani, M.S., 1999, Mount Mazama eruption: Calendrical age verified and atmospheric impact assessed: Geology, v. 27, p. 621–624, doi:10.1130/0091-7613(1999)027<0621:MMECAV>2.3.CO;2.

Zhao, J.X., and Xu, H., 2012, Magnitude-scaling rate in ground-motion prediction equations for response spectra from large subduction interface earthquakes in Japan: Seismological Society of America Bulletin, v. 102, p. 222–235, doi:10.1785/0120110154.

Geosphere

A 6600 year earthquake history in the region of the 2004 Sumatra-Andaman subduction zone earthquake

Jason R. Patton, Chris Goldfinger, Ann E. Morey, Ken Ikehara, Chris Romsos, Joseph Stoner, Yusuf Djadjadihardja, Udrekh, Sri Ardhyastuti, Eddy Zulkarnaen Gaffar and Alexis Vizcaino

Geosphere published online 12 November 2015;
doi: 10.1130/GES01066.1

Geosphere, published online on 12 November 2015 as doi:10.1130/GES01066.1

Notes